An Extraction System for Radiocarbon Microanalysis of Dissolved Organic Carbon in Glacier Ice

Inauguraldissertation
der Philosophisch-naturwissenschaftlichen Fakultät
der Universität Bern

vorgelegt von

Johannes Schindler

aus Josefstal, Deutschland

Leiterin der Arbeit:
Prof. Dr. Margit Schwikowski
Departement für Chemie und Biochemie der Universität Bern

Original document saved on the web server of the University Library of Bern

This work is licensed under a Creative Commons Attribution-Non-Commercial-No derivative works 2.5 Switzerland licence. To see the licence go to http://creativecommons.org/licenses/by-nc-nd/2.5/ch/ or write to Creative Commons, 171 Second Street, Suite 300, San Francisco, California 94105, USA.

source: https://doi.org/10.24442/boristheses.854 | downloaded: 19.4.2024

Copyright Notice

This document is licensed under the Creative Commons Attribution-Non-Commercial-No derivative works 2.5 Switzerland. http://creativecommons.org/licenses/by-nc-nd/2.5/ch/

You are free:

to copy, distribute, display, and perform the work

Under the following conditions:

Attribution. You must give the original author credit.

Non-Commercial. You may not use this work for commercial purposes.

No derivative works. You may not alter, transform, or build upon this work..

For any reuse or distribution, you must take clear to others the license terms of this work.

Any of these conditions can be waived if you get permission from the copyright holder.

Nothing in this license impairs or restricts the author's moral rights according to Swiss law.

The detailed license agreement can be found at:
http://creativecommons.org/licenses/by-nc-nd/2.5/ch/legalcode.de

An Extraction System for Radiocarbon Microanalysis of Dissolved Organic Carbon in Glacier Ice

Inauguraldissertation
der Philosophisch-naturwissenschaftlichen Fakultät
der Universität Bern

vorgelegt von

Johannes Schindler

aus Josefstal, Deutschland

Leiterin der Arbeit:
Prof. Dr. Margit Schwikowski
Departement für Chemie und Biochemie der Universität Bern

Von der philosophisch-naturwissenschaftlichen Fakultät angenommen:

Bern, 02. Juni 2017 Der Dekan:

Prof. Dr. Gilberto Colangelo

Zum Besten aller Wesen.

Summary

Alpine glaciers situated in mid- and low latitudes are valuable archives for paleoclimatology. They offer a continuous record of recent local climatic conditions in regions where the majority of humankind lived and still lives. For meaningful interpretation of an ice core from such an archive, accurate dating is essential. Usually, several complementary approaches are used to establish a depth–age relationship. The oldest part of the ice at the bottom of the ice core suffers annual layer thinning and is influenced by small-scale bedrock geometry, which limits the use of annual layer counting or the assignment of reference horizons for dating. Nuclear dating techniques overcome this restriction since they do not rely on the preservation of a resolvable stratigraphy by using the continuous record of the respective radioisotope.

Radiocarbon is especially powerful for dating alpine glaciers because its half-life of 5730 years suitably allows it to cover the typical age range of these archives. Most important, glacier ice does contain minute amounts of carbon. While macrofossils can only be found by coincidence, organic aerosols deposited on the glacier offer the best source of contemporary carbon in glacier ice. Despite a large part of its chemical composition being unknown, organic carbon found in an ice sample can be operationally classified into a particulate fraction (POC) and a dissolved fraction (DOC). Radiocarbon dating of POC has proven to be very successful and is a routine application by now. The major limitation of this technique is the low POC concentration found especially in pre-industrial and polar ice samples.

Therefore, the DOC fraction promises even better suitability for dating thanks to its by a factor of 5 to 10 higher concentrations. Nevertheless, a straightforward analysis of DOC is hampered by its vulnerability to contamination. DOC consists in large part of mono- and dicarboxylic acids – compounds that can easily be taken up from the surrounding gas phase during sample preparation or which are dissolved from surfaces in contact with

the liquid sample. Hence it is vital to ensure ultra-clean sample preparation with a low and stable procedural blank for reliable radiocarbon analysis of DOC from glacier ice.

In this work, we developed an extraction system for DOC from glacier ice samples. To meet the requirements of ultra-clean and efficient carbon extraction, the complete sample treatment is performed in inert gas conditions and only dedicated materials are chosen for the individual components of the setup.

Ice samples are pre-cleaned and melted in a melting vessel. POC is separated from the liquid sample by filtration during the transfer to the photo-reactor. The sample is acidified and inorganic carbon is degassed from the solution. A minimal invasive photo-oxidation method is applied by means of external UV irradiation of the sample. This converts the DOC to CO_2, which is degassed, cleaned and captured in cryogenic traps. The CO_2 is quantified to determine the initial DOC concentration and is sampled to glass vials. With state-of-the-art accelerator mass spectrometry, the gaseous CO_2 sample is directly analysed for its radiocarbon content to yield the age of the ice sample.

Following a detailed description of the extraction system hardware and its operation protocol, we show the results of its extensive characterisation. The setup can process ice samples of up to 400 g mass. Within 45 min of irradiation time, oxalic acid was oxidised and recovered as CO_2 with an efficiency of $(85 \pm 7)\%$. Most important, thanks to the stringent working conditions we achieved a low overall procedural blank of $m_{\mathrm{blank}} = (3.5 \pm 0.6)\,\mu\mathrm{g\,C}$ with $F^{14}\mathrm{C}_{\mathrm{blank}} = 0.65 \pm 0.04$. This allows for the reliable measurement of ice samples with carbon concentrations as low as $33\,\mu$g C/kg ice, if we require the minimal sample mass to be larger than three times the blank mass. Thus by now, the method provides the anticipated efficiency and accuracy to analyse $\mathrm{DO}^{14}\mathrm{C}$ of ice samples from alpine glaciers.

As a side product of the method, also POC is extracted. We found that the procedural blank for this method is similar to the standard method for $\mathrm{PO}^{14}\mathrm{C}$ analysis. Therefore, this setup can be used to analyse both organic carbon fractions from only one ice sample.

We validated this new method with well-dated ice samples from Juvfonne ice patch in Norway. Six samples from three different ice blocks were analysed for $\mathrm{DO}^{14}\mathrm{C}$ and $\mathrm{PO}^{14}\mathrm{C}$. Within the uncertainties and the sample-to-sample variability most $F^{14}\mathrm{C}$ results from both organic carbon fractions agree with each other and with the reference samples from the same ice blocks. In contrast to previous studies that proposed a possible in-situ

$DO^{14}C$ production in glacier ice, we did not find such a bias. Thus, we conclude that radiocarbon microanalysis with DOC from glacier ice is both technically feasible and physically meaningful and can now contribute to future cryospheric science.

Contents

Summary **v**

Contents **viii**

1 Introduction **1**
1.1 Alpine glaciers as archives for paleoclimatology 1
1.2 Dating of ice cores 2
1.3 Radiocarbon dating 4
1.3.1 General concept 4
1.3.2 Radiocarbon dating of glacier ice 5
1.3.3 In-situ production of radiocarbon in ice 7
1.3.4 Radiocarbon analysis with the MICADAS AMS 8
1.4 Organic carbon 10
1.4.1 General classification 10
1.4.2 Organic carbon in glacier ice 10
1.5 Extraction of dissolved organic carbon 13
1.5.1 Contamination 13
1.5.2 Separation from particulate organic carbon 14
1.5.3 Removal of inorganic carbon 15
1.5.4 Oxidation of dissolved organic carbon 15
1.6 Aim of this work 18

2 Setup **20**
2.1 Concept and Overview 20
2.2 Melting vessel and filtration unit 23
2.2.1 Glass setup 23
2.2.2 Ultra-high purity helium supply 23
2.2.3 Melting vessel 24
2.2.4 Filtration unit 25
2.3 Photo-reactor 26

2.3.1 Reactor head and cooling finger . . . 26
2.3.2 Photo-reactor and UV source . . . 28
2.3.3 Cryogenic water traps . . . 29
2.4 Vacuum line . . . 31
2.5 User protection . . . 34
2.6 Operation protocol . . . 37
2.6.1 Ice sampling . . . 37
2.6.2 Preparation and installation . . . 38
2.6.3 Cleaning . . . 38
2.6.4 Melting . . . 40
2.6.5 Filtration and oxidation . . . 40
2.6.6 Sampling . . . 41
2.6.7 Next measurement . . . 42

3 Characterisation **44**
3.1 CO_2 sample processing . . . 44
3.1.1 CO_2 sample transport . . . 44
3.1.2 CO_2 trapping . . . 45
3.1.3 Recovery of CO_2 from the liquid sample . . . 46
3.1.4 Quantification of CO_2 and sample concentration . . . 48
3.2 Oxidation of dissolved organic carbon . . . 49
3.2.1 Production of dissolved organic carbon standards . . . 50
3.2.2 Oxidation process . . . 51
3.2.3 Oxidation efficiency . . . 53
3.3 Method blank . . . 55
3.3.1 CO_2 sample processing blank . . . 55
3.3.2 Oxidation blank . . . 55
3.3.3 Overall dissolved organic carbon blank . . . 59
3.3.4 Particulate organic carbon blank . . . 61
3.4 Discussion . . . 63
3.4.1 Overview . . . 63
3.4.2 Limitations . . . 65
3.4.3 Comparison with existing methods . . . 66

4 Validation **69**
4.1 Site and ice sample description . . . 69
4.2 Particulate organic carbon . . . 72
4.3 Dissolved organic carbon . . . 73
4.4 Conclusions . . . 75

5 Conclusion and Outlook **77**

A List of Suppliers **83**

B Supply electronics box **87**

C Calibrations **89**
C.1 Sample mass measurement 89
C.2 Manometry 90
C.2.1 External calibration of the pressure transmitter 90
C.2.2 Calibration of the manometry cell volume 91
C.2.3 Calibration of the vacuum line parts volumes 92
C.3 Non-dispersive infrared CO_2 detector 93

D Operation Manual **96**

E MICADAS Measurement Data **110**

Bibliography **114**

List of Symbols and Abbreviations **126**

Acknowledgements **128**

Declaration **130**

Chapter 1

Introduction

The study of ice cores from alpine glaciers for paleoclimatology requires expertise in multiple disciplines ranging from demanding field work and logistics, trace level chemical analysis of ice samples and a broad understanding of the underlying chemical, physical and climatic processes for well-grounded interpretation. A crucial element is the accurate dating of the climatic record. In this chapter, we introduce the fundamentals of our approach – radiocarbon dating of dissolved organic carbon.

1.1 Alpine glaciers as archives for paleoclimatology

Glaciers and ice sheets are very valuable archives for paleoclimatology. Precipitation deposits as snow on their surface and forms firn and ice with proceeding time, layer by layer. This offers a record of the deposited aerosols, entrapped atmospheric air and the amount of precipitation as well as its chemical and isotopic composition. Analysing such archives allows to follow environmental changes and climate variability over time [Schwikowski and Eichler, 2010]. For this purpose, ice cores have been drilled at glaciers and ice sheets of interest all over the globe (for example, see Fig. 1.3). Among other paleoclimatic proxies such as tree rings, corals, lake and ocean sediments or speleothems, ice cores belong to the most accurate and direct proxies of past atmospheric conditions.

Ice cores from the Greenland ice sheet and Antarctic ice sheet extend to depths of several thousand meters and cover time periods of up to 800 000 years [Lambert et al., 2008; Jouzel, 2013], recent efforts try to extend this scale to 1.5 million years [Fischer et al., 2013]. Whereas these records are of great use for the reconstruction of global climate history, alpine glaciers store regional climate signals. Although smaller in extend of both time

Figure 1.1: Snow crystals at Colle Gnifetti (Italian–Swiss border, 4450 m a.s.l.) reflecting the full-moon. The lights of Milan glow on the horizon and visibly demonstrate the vicinity of human activity.

and depth, ice cores from alpine glaciers situated in mid- and low latitudes represent the climate in regions where the majority of humankind lived and still lives (for example, see Fig. 1.1). Prominent alpine ice core sites such as Illimani (6300 m a.s.l., Andes) or Colle Gnifetti (4450 m a.s.l., Alps) have an ice thickness on the order of 100 m and hold ice from all over the Holocene period [Sigl et al., 2009; Jenk et al., 2009].

For an optimal preservation of the climatic signal, ideal ice core sites have only minimal lateral ice flow and are non-temperate[1]. Under these conditions, alpine glaciers are invaluable environmental archives. For example, ice cores that have been drilled at the above mentioned sites could be used to reconstruct the history of lead pollution in South America over the past 2000 years and the European heavy metal emissions since the 1650s [Eichler et al., 2015; Barbante et al., 2004].

1.2 Dating of ice cores

For a meaningful interpretation of ice cores, accurate dating is essential. Establishing a reliable depth–age relationship usually employs different, complementing methods, as shown in Fig. 1.2. Annual layer counting, comparable to tree ring counting, is the most straightforward method. It takes advantage of seasonal variations of the concentration or isotopic composition of the respective variable such as ammonium or $\delta^{18}O$, the stable isotope

[1] Ice temperature always below the corresponding pressure-melting point.

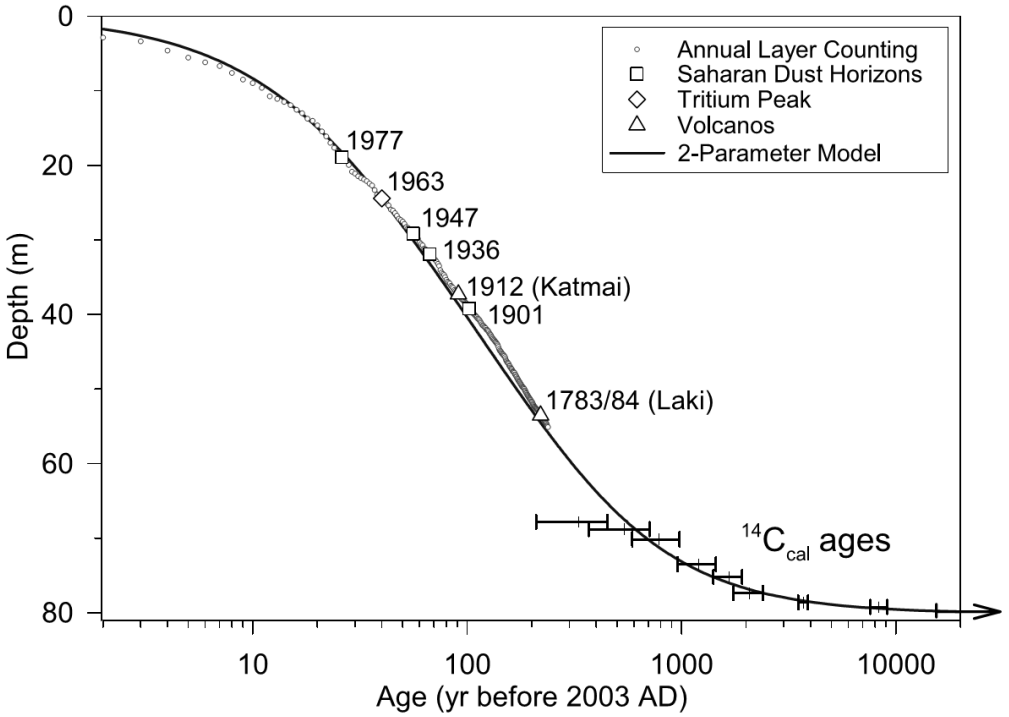

Figure 1.2: Dating of an ice core from Colle Gnifetti with complementing dating methods. While annual layer counting and distinct time markers work well in the upper part of the ice core, ^{14}C ages derived from POC analysis and a two-parameter model extend the depth–age relationship to the full scale of the archive. Figure from Jenk et al. [2009].

ratio of oxygen [Eichler et al., 2000; Thompson et al., 1998]. However, this approach breaks down at the lower parts of ice bodies, where the annual layers suffer thinning below the counting resolution due to strain induced ice flow. Additionally, reference horizons such as known volcanic eruptions, Sahara dust events or the tritium peak produced by nuclear weapon tests in the 1960s provide very good time markers to tie down the depth–age relationship [Knüsel et al., 2003; Jenk et al., 2009]. Physical ice flow models can improve the dating even further, however in the lower part of the ice body the small scale geometry of the bedrock hampers high resolution modelling [Lüthi and Funk, 2001].

The nuclear analysis of radioisotopes contained in the ice offers time information in sections where other approaches suffer limitations due to layer thinning or complex ice flow as it does not rely on a resolvable stratigraphy. For example ^{210}Pb (half-life 22.3 a) dating is well established and very useful for short time-scales [Crozaz and Langway, 1966; Gäggeler et al., 1983]. Radiocarbon (^{14}C, half-life 5730 a) is especially suitable for the dating of

ice cores from alpine sites as it is particularly powerful from pre-industrial ages to several 10 000 years. While the straightforward analysis of gaseous CO_2 from air bubbles in the ice is hampered by the in-situ production of ^{14}C (see Sec. 1.3.3) and requires large amounts of ice, radiocarbon analysis of the organic carbon contained in the ice has proven to be very successful (see Sec. 1.3.2).

1.3 Radiocarbon dating

1.3.1 General concept

Carbon naturally exists in the three isotopes ^{12}C (abundance 98.9%, stable), ^{13}C (abundance 1.1%, stable) and ^{14}C (abundance 1 ppt, radioactive) [Weast and Astle, 1982]. The carbon cycle describes the mixing and redistribution of carbon on the global scale between its reservoirs such as the atmosphere, hydrosphere, lithosphere, cryosphere and biosphere. Radiocarbon is produced mainly in the atmosphere from nitrogen in a spallation reaction with neutrons which were generated from cosmic rays:

$$^{14}_{7}\mathrm{N} + \mathrm{n} \rightarrow ^{14}_{6}\mathrm{C} + \mathrm{p}.$$

Radiocarbon is unstable and decays in a β-decay with half-life $t_{1/2} = 5730 \pm 40$ years:

$$^{14}_{6}\mathrm{C} \rightarrow ^{14}_{7}\mathrm{N} + \mathrm{e} + \bar{\nu}_\mathrm{e},$$

where p is a proton, e is an electron and $\bar{\nu}_\mathrm{e}$ an electron anti-neutrino [Demtröder, 2009].

These processes lead to an equilibrium of radiocarbon within the carbon cycle, which however is not stable over time. Changes in solar activity modulate the cosmic ray flux and thus influence the ^{14}C production. Also the combustion of ^{14}C depleted fossil fuels measurably increases the $^{12}C/^{14}C$ ratio of CO_2 in the atmosphere, known as the Suess effect. Vice versa, the nuclear weapon tests performed from 1945 on produced large amounts of excess ^{14}C, the so-called bomb peak.

To correct for the changes of the $^{12}C/^{14}C$ ratio over time, calibration curves are established based on well-dated archives, such as tree rings [Reimer et al., 2013]. By this, the radiocarbon age which results from the exponential decay law[2] can be converted to the calendar age.

The 'start of the radiocarbon clock' is set by the end of the carbon mixing with the environment, e.g. the death of an organism or the isolation

[2] $A(t) = A_0 e^{-\ln 2 \cdot t \,/\, t_{1/2}}$, where $A(t)$ is the activity at time t and A_0 is the initial activity

of a formed carbonaceous aerosol: no more new ^{14}C is added and because of the unceasing radioactive decay the $^{12}C/^{14}C$ ratio starts to increase.

Apart from a calibration, also fractionation effects have to be taken into account for meaningful ^{14}C measurements. Fractionation summarises various physical and chemical effects that alter the isotopic ratio in dependence of the different isotope masses. Carbon typically experiences fractionation in biochemical processes such as the differential uptake of its isotopes in plants. To compare the carbon isotope ratios from samples of different origin, the carbon ratios are normalised to samples from wood [Stenström et al., 2011].

Furthermore, measured ^{14}C values are referenced to a standard substance[3] for absolute comparability. This gives rise to the unit-less and time independent quantity 'fraction modern' $F^{14}C$:

$$F^{14}C = \frac{A_{SN}}{A_{ON}}$$

where A_{SN} is the normalised ^{14}C activity of the sample and A_{ON} is the normalised ^{14}C activity of the standard material. $F^{14}C$ is normalised and standardized and does not depend on the year of measurement. With the use of a calibration curve, $F^{14}C$ can be transformed to a calendar age [Stenström et al., 2011].

1.3.2 Radiocarbon dating of glacier ice

Carbon is found in the ice matrix in different reservoirs. In exceptional cases, fragments of organic material such as leaves or insects have been discovered and were used for dating [Thompson et al., 1998, 2006; Nesje et al., 2012; Uglietti et al., 2016].

A more projectable approach, and also one of the early cornerstones in polar ice core science, is the analysis of the entrapped atmospheric air that contains carbon dioxide (CO_2), methane and organic gases. However, due to the large required sample mass, it is not favoured for the use in alpine ice cores. Furthermore, the time lag between snowfall and pore close off in the ice as well as in-situ production of $^{14}CO_2$ pose additional challenges [Van De Wal et al., 1994; Petrenko et al., 2013].

Mineral dust deposition on glacier, e.g. Saharan dust in the Alps, also contributes to the carbon stock with carbonates [Maupetit and Delmas,

[3]The absolute radiocarbon standard is defined to have a specific activity of 226 Bq/kg C and is intended to correspond to the specific activity of the atmosphere in 1950.

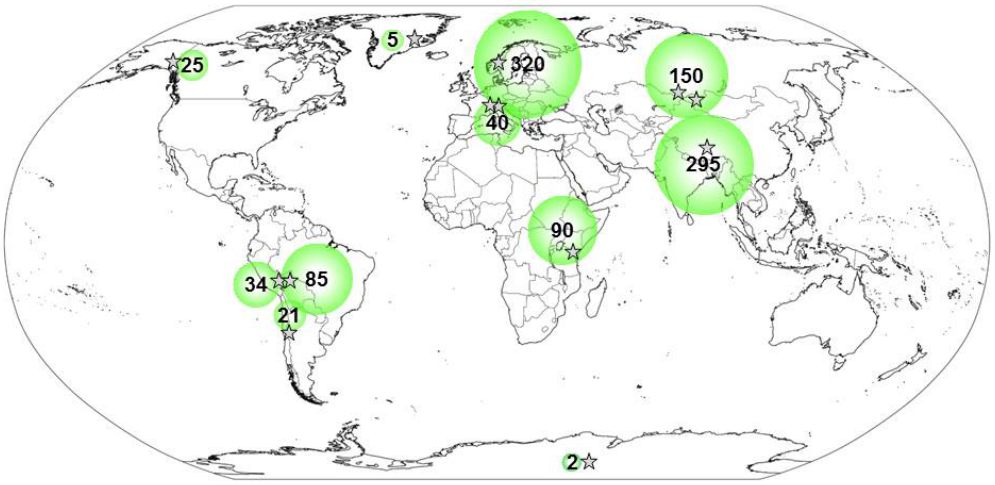

Figure 1.3: World map showing the sites from which ice samples were analysed with the PO^{14}C method (grey stars). The average POC concentration in μg C/kg ice at each site is indicated with green bubbles. Figure from Uglietti et al. [2016].

1994; Schwikowski et al., 1995], but these compounds are old and thus depleted in ^{14}C.

Elemental carbon (EC) originates from pyrolysis during incomplete combustion [Bond et al., 2013] and is found in glacier ice. It can be used as a proxy for fire reconstruction [Legrand et al., 2016], however too low concentrations hamper its use for radiocarbon dating [Lavanchy et al., 1999; Hagler et al., 2007].

Similarly, the organic matter of bacteria and snow algae that reside on the glacier has too low concentration for an application of radiocarbon dating [Yoshimura et al., 2000; Takeuchi et al., 2006].

The bulk of organic carbon (OC) offers the most abundant carbon reservoir in glacier ice. It can be operationally divided into the two sub-fractions of dissolved organic carbon (DOC) and particulate organic carbon (POC) (see Sec. 1.4), both sub-fractions have been used for radiocarbon dating.

In particular POC proved to be a robust candidate and has been applied to several alpine ice samples (see Fig. 1.3and Steier et al. [2008]) and even firn samples [Cao et al., 2013] which pose additional challenges concerning the sample decontamination. The used method [Jenk et al., 2007] originates from procedures established for radiocarbon analyses of aerosols. It involves the thermal oxidation of OC that is extracted from ice samples by filtration. However, the very low POC concentrations of only few μg C/kg ice at remote

sites limit the use of this method in particular for high-latitude sites [Hagler et al., 2007].

Compared to POC, the DOC concentrations are higher by a factor of 5 to 10 [Legrand et al., 2013a], making this fraction very attractive for dating purposes. DOC has been extracted from glacier ice for radiocarbon dating by May [2009] and Steier et al. [2013], both using a wet ultraviolet (UV) photo-oxidation setup. Nevertheless, its analysis proofed to be difficult especially in terms of contamination (see Sec. 1.5.1), and even the hypothesis of possible in-situ production of ^{14}C in DOC in glacier ice was proposed (see Sec. 1.3.3). Still, DO^{14}C could be applied for a source apportionment study with contemporary ice samples from Col du Dôme [May et al., 2013] as well as a qualitative comparison of DOC ages of ice samples from 26 Alpine glaciers [Singer et al., 2012].

1.3.3 In-situ production of radiocarbon in ice

Apart from the major production path from nitrogen in the atmosphere, ^{14}C production from oxygen can also play a role when considering ice samples. In this case neutrons – and to a lesser degree also muons – that are generated from cosmic rays activate the parent nuclide by spallation:

$$^{16}_{8}\mathrm{O} + \mathrm{n} \rightarrow ^{14}_{6}\mathrm{C} + \mathrm{p} + \mathrm{p} + \mathrm{n}.$$

This process occurs at much lower rates than the common production path in the atmosphere. However, for high-latitude or high-altitude sites it is important to account for it because of the enhanced exposure to cosmic rays.

For example, hot ^{14}C atoms oxidise successively to CO and CO_2 and thus disturb the original radiocarbon budget of the contained CO_2. Lal et al. [1987] took advantage of this effect to estimate ablation and accumulation rates of glaciers from the bias in ^{14}C content. Furthermore, based on the ratio ^{14}CO to $^{14}CO_2$ van Roijen et al. [1995] proposed a method for correction of in situ ^{14}C in ice.

While this in-situ production of ^{14}CO, $^{14}CO_2$ and $^{14}CH_4$ in polar ice is well known and understood [Petrenko et al., 2009, 2013], it is not yet fully resolved to what extend this effect may influence DO^{14}C in alpine ice samples. In principle, the ^{14}C in-situ production rate is higher at a low-latitude high-altitude site than at a high-latitude low-altitude site [Masarik and Beer, 1999; Lal and Jull, 1990]. However, it is questionable whether a notable production of organic compounds from the in-situ produced ^{14}C

can take place and if these compounds would be preserved in the the firn until the pore close off.

May [2009] reports super-modern and inconclusive ^{14}C values of DOC extracted from several ice samples from Colle Gnifetti (Alps) and attributes this to the effect of in-situ produced DO^{14}C. In a follow-up study, Hoffmann [2016] performed laboratory experiments in which ice samples were intensely irradiated with fast neutrons from a deuterium-tritium source. A strongly increased ^{14}C content of the DOC fraction of these artificial samples gives the proof-of-principle for this process. However, if and to what extend this is relevant for real alpine ice samples still has to be investigated with real ice samples and an unambiguous method.

1.3.4 Radiocarbon analysis with the MICADAS AMS

First radiocarbon dating experiments were performed with Geiger counters, gas proportional counters and later-on also by liquid scintillation counting [Libby et al., 1949]. As all these methods rely on the measurement of decay events, while ^{14}C only shows weak radioactivity due to its long half-life, large sample masses are required while resolution and limit of detection still are limited. The advent of accelerator mass spectrometry (AMS) tremendously widened the horizon for ^{14}C measurements as this direct approach allows to detect the ^{14}C atoms itself and not only their decay [Bennett et al., 1977; Nelson et al., 1977].

Likewise within the field of AMS there has been immense progress. Initially, large Tandem accelerators that operate in the MeV energy range had to be used. Improvements in ion sources, ion separation and detection allowed substantial reduction of the required ion energies down to 45 keV [Synal et al., 2013]. Thus, common high voltage power supplies can be used and in consequence cheaper and smaller designs are available. Additionally, thanks to the development of gas ion sources for AMS systems it is possible to circumvent the otherwise needed graphitisation step for sample preparation, which is work intensive and can introduce additional contamination. Instead, with a gas ion source that is fed with a gas inlet system (GIS), the direct handling of gaseous ^{14}C samples in the form of CO_2 has become possible [Ruff et al., 2007].

All ^{14}C measurements of this study have been performed at the Laboratory for the Analysis of Radiocarbon with AMS (LARA) at University of Bern with the AMS instrument MICADAS [Szidat et al., 2014]. The Mini radioCarbon Dating System (MICADAS) was developed at the department

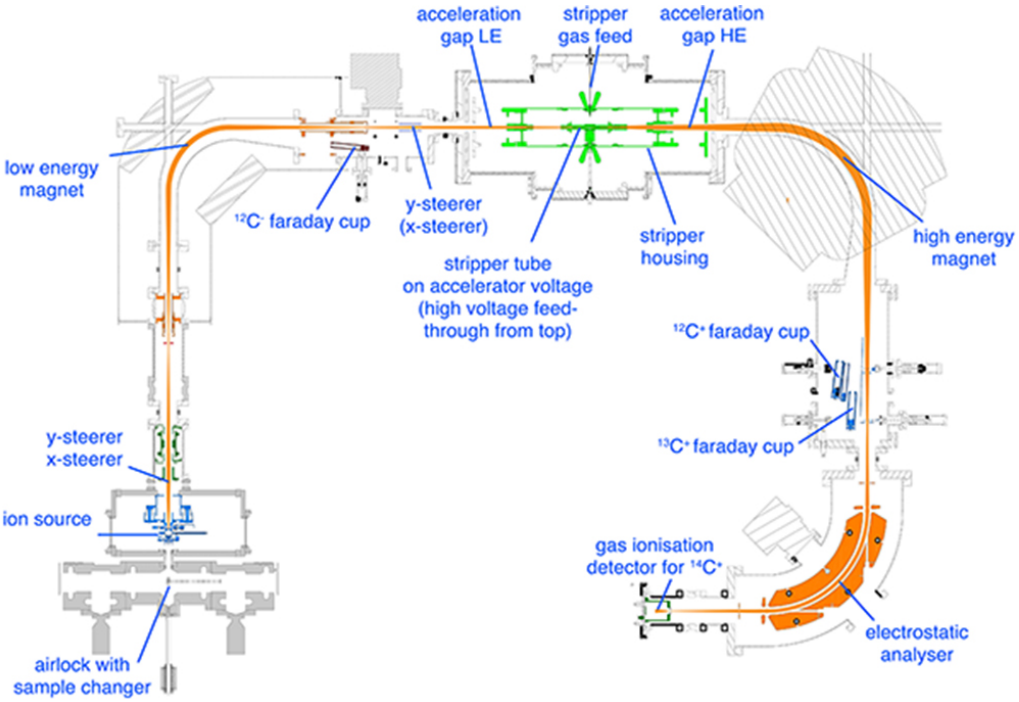

Figure 1.4: Schematic of the MICADAS AMS system and its individual compounds. Figure from Ionplus AG [2015].

for Ion Beam Physics at the Swiss Federal Institute of Technology Zurich [Synal et al., 2007].

A schematic of the setup is shown in Fig. 1.4, its working principle can be described briefly as follows. Glass ampoules containing CO_2 are opened with the help of a cracker unit in the GIS, mixed with helium and transferred with a syringe to the gas ion source of MICADAS. A caesium sputter ion source creates a beam of Cs^+ ions that ionize the carbon of the gas sample on a titanium surface which is used as a catalyst. The resulting C^- beam is accelerated towards the high voltage section by the ion source potential of -40 kV, passing a deflection magnet acting as a first mass selector. In the accelerator segment at 200 kV, the carbon ions enter a stripper tube filled with nitrogen. Collisions lead to a charge state conversion from C^- to C^+, thus the carbon atoms are accelerated further and leave the acceleration unit at a energy of 440 keV. This Tandem accelerator configuration has not only the advantages of using the potential difference twice and having both ends of the accelerator on ground potential, furthermore the stripping process also destroys interfering molecules such as ^{13}CH. A second magnet splits the ion beam for the individual determination of the ^{12}C, ^{13}C and ^{14}C atoms in Faraday cups and an gas ionisation detector, respectively.

With this setup, radiocarbon can be determined in samples ranging from only 3 μg to 100 μg carbon mass in routine operation with a detection limit of $\approx$ 52 kyr before present (BP) at an uncertainty of 3%. The raw data is processed in the data evaluation program 'BATS' [Wacker et al., 2010] that corrects for systematic effects, applies a background correction based on measured blank samples, accounts for isotope fractionation using the ^{13}C measurement, normalises to measured standard samples and deduces the uncertainty of the reported result.

1.4 Organic carbon

1.4.1 General classification

While a concluding and detailed chemical speciation of the individual compounds of the OC contained in an ice sample is difficult because of the manifold different organic compounds, a classification according to the properties of interest is sufficient for many applications.

A possible classification of carbonaceous compounds found in glacier ice is shown in Fig. 1.5. The total organic carbon (TOC) can be subdivided according to its refractory and optical properties to elemental carbon (EC) and OC. EC originates from the incomplete combustion of biomass or fossil fuels, is strongly light absorbent and thus also known as black carbon (BC). OC can also be produced in combustion processes, while to a large part it is emitted directly from the biosphere or formed in the atmosphere from gaseous precursors. It can be subdivided further according to its water solubility into a soluble (WSOC) and an insoluble (WIOC) fraction [Uglietti et al., 2016]. In a melted ice sample, this corresponds to DOC and POC, and thus this nomenclature is used in this work. The inorganic carbon (IC) comprises CO_2, carbonic acid, carbonate and bicarbonate.

1.4.2 Organic carbon in glacier ice

Following its emission from natural or anthropogenic sources, OC is transported to glaciers via the atmosphere. While POC consist mainly of primary organic aerosol that were directly emitted, DOC derives rather from secondary organic aerosol that are formed within the atmosphere from volatile organic compounds [Gelencsér et al., 2007]. These carbonaceous aerosol suffer ageing processes such as photo-oxidation and thus their lifetime is limited to 4.5 to 7 days [Müller, 1984]. Hence, OC is a proxy that is determined mainly by local- to regional-scale emissions.

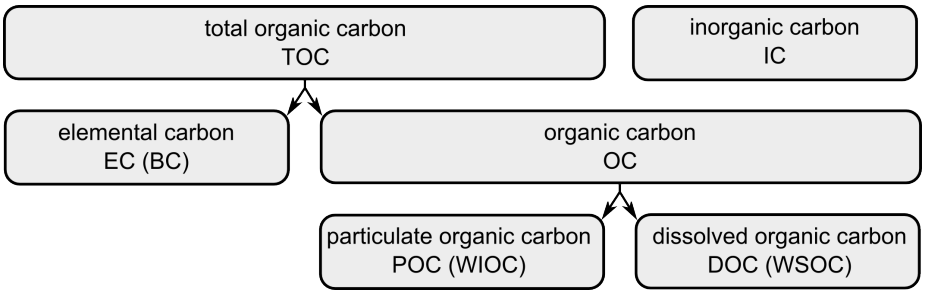

Figure 1.5: Schematic overview on the operational classification of the total organic carbon of an ice sample. The respective abbreviations and, where appropriate, the alternative nomenclature is given in brackets: BC = black carbon, WIOC = water-insoluble carbon, WSOC = water-soluble carbon.

OC is scavenged from the atmosphere by both wet and dry deposition and is incorporated to the snow-pack [Lavanchy et al., 1999; Legrand et al., 2007]. Another pathway is the dissolution of organic gases in the firn layer[4]. However, it is unclear how well volatile compounds are retained in the firn column and how much is re-emitted to the atmosphere [Legrand et al., 2007]. In general, post-depositional processes can alter the OC within the snow, as observed by the degradation of POC in snow in Greenland [Grannas et al., 2007].

While the OC concentration in glacier ice is highly dependent on the geographic location, season and time period, DOC concentrations are in general much higher than POC concentrations. Ice samples from Col du Dôme (Mt. Blanc, French Alps) have a POC/DOC ratio of 1/5, ice samples from Summit (Greenland) have a POC/DOC ratio of only 1/10 [Legrand et al., 2007]. Because of the vicinity to OC sources, total DOC concentrations are highest in the Alps. Here, pre-industrial ice typically has DOC concentrations of around 70 μg C/kg ice, while DOC concentrations in Greenland and Antarctica are much lower at around 20 μg C/kg ice and 10 μg C/kg ice, respectively [Legrand et al., 2013a].

In the Alps, a seasonal variation of OC concentration is observed, with lower OC values in winter because of the reduced source activity and the enhanced stratification of the atmosphere limiting transport to high-alpine sites. Also on longer time-scales OC concentrations are variable: during the industrialisation, anthropogenic activities resulted in a strong increase of OC concentrations. In addition, biogenic emissions were enhanced be-

[4]In the accumulation zone of a glacier, snow accumulates over several years, forming a snow-pack with increasing density (firn) before it turns to glacier ice. It is characterised by open pores and densities from 400 kg/m^3 to 830 kg/m^3, and a typical thickness of 10 m to 50 m [Cogley et al., 2011].

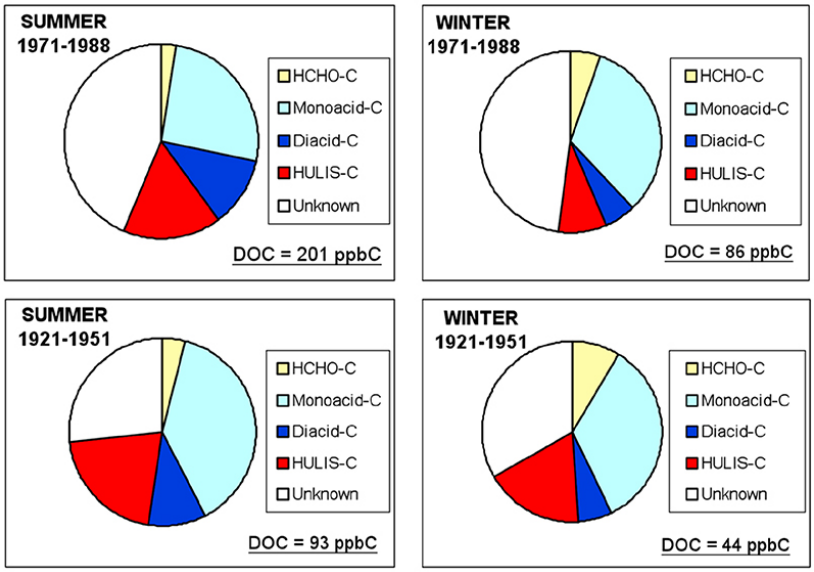

Figure 1.6: Chemical composition of ice samples from Col du Dôme (French Alps, 4250 m a.s.l.) with seasonal resolution (left and right panels) from two time periods of the 20th century (top and bottom panels). HCHO-C (formaldehyde), monocarboxylic acids (formic, lactic, acetic, glycolic and glyoxylic acid), dicarboxylic acids (oxalic, malic, malonic, succinic, and glutaric acid), HULIS (humic like substances). Graph from Legrand et al. [2013b].

cause of higher temperatures and higher atmospheric CO_2 concentrations [Legrand et al., 2013a]. Both the seasonal variation and the human imprint are visible in the absolute DOC concentrations from Col du Dôme shown in Fig. 1.6.

Legrand et al. [2013b] analysed DOC from Col du Dôme ice samples on a compound-class specific level (see Fig. 1.6). Overall, monocarboxylic acids (in particular formic acid) and humic like substances represent the most abundant compounds apart from a large unidentified fraction. As shown by Müller-Tautges et al. [2016] for ice samples from Grenzgletscher (Swiss Alps, 4200 m a.s.l.), formic and oxalic acid are highly correlated with calcium, indicating the relevance of mineral dust for OC transport. While OC found in glacier ice is highly diverse, it is also very bioavailable. Thus, besides being a non-negligible global carbon storage, glaciers and ice sheets also supply downstream organisms with the OC contained in the run-off [Singer et al., 2012; Hood et al., 2015].

1.5 Extraction of dissolved organic carbon

For quantification and ^{14}C analysis, the carbon of the DOC fraction needs to be extracted from the sample as CO_2 in a reproducible and efficient way. Because of the low carbon masses in the 10 to 100 μg range, the procedural blank furthermore needs to be very low and stable both considering its mass and its isotopic signature to allow for reliable correction of the result. Therefore, all sample processing steps need consideration in terms of contamination and efficiency. An overview of the different extraction steps and the chosen method is shown in Fig. 1.7: after decontamination and melting of the frozen ice sample, POC and IC need to be extracted before DOC can be oxidised to a CO_2 sample that can be analysed offline with MICADAS AMS for ^{14}C.

1.5.1 Contamination

Any trace analysis requires dedicated techniques to minimise sample contamination by the sample preparation and measurement itself. Several factors stress this need in the case of DO^{14}C analysis. First, DOC consists of numerous different organic molecules that all contribute to it and similarly also a wide rage of possible contaminants has to be addressed. Second, a sample in liquid form in general is more prone to contamination as it dissolves and releases contaminations from touching surfaces and is also in strong exchange with the gas phase around it.

Druffel et al. [2013] reported an increase in DOC concentrations of duplicate samples that have been thawed, refrozen and remeasured 21 days later again. They also emphasized the influence of DOC leachable plumbing such as polyvinyl chloride tubes of an ultra-pure water dispenser on the apparent ^{14}C age of the ultra-pure water.

In a review on DOC concentrations measured in snow and ice, Legrand et al. [2013a] attributed most inconsistencies between the different results to contamination resulting from non-dedicated sampling and storage involving containers and tools made from plastic material. Furthermore, it is assumed that the drill fluids used for the drilling of deep ice cores can contaminate ice samples via micro cracks in the sample. Fortunately, this threat is in general not given for the shallower alpine ice cores which are drilled without the use of drill fluids as at these depths no hole stabilisation is needed.

May [2009] observed the release of DOC from preheated quartz fibre filters into the filtrate. In general, not much attention is paid to the filtration step that separates DOC from POC, however apart from a clean filter also

the mixing with surrounding gas has to be prevented. Commonly used filtration units are not gas-tight and do induce a strong mixing with ambient air due to pressure gradients.

Apart from tests that emphasise the problem of sample contamination by contact with various plastic materials such as polytetrafluoroethylene (PTFE), perfluoroalkoxy (PFA), polyethylene, or polypropylene, Preunkert et al. [2011] presented uptake curves of DOC from lab air to liquid water samples. In dependence of the ambient laboratory air, uptake rates of up to 250 $\frac{\mu g\,\mathrm{C}}{\mathrm{kg\,hour}}$ were observed for 50 ml samples with a surface area of 8 cm^2. It is assumed that formic and acetic acid are major players in the dissolution of DOC from atmospheric air. A further decontamination experiment of ice samples showed the need and effect of thorough sample cleaning. Ice samples that were only decontaminated by mechanical removal of outer layers with a saw showed strongly increased DOC concentrations compared to ice samples that were additionally washed with ultra-pure water [Preunkert et al., 2011].

In account of these findings, it is evident that it is vital to exclude any sources of contamination during DOC extraction. For ultra-pure sample processing, an inert gas atmosphere has to be used and any contact with plastic material has to be avoided.

1.5.2 Separation from particulate organic carbon

As illustrated in Fig. 1.7, after the ice sample has been cut, decontaminated and melted, the POC fraction is removed from the liquid sample by filtration. The separation of POC from DOC is operationally defined by filtration, thus the cut-off size of the used filter sets the partitioning of POC and DOC. Quartz fibre filters are the most common used filters for this method. They are especially suitable because they do not contain organic material and have high thermal stability that allows for thermal cleaning before use. Although quartz fibre filters do not exhibit a precisely known pore size because of their construction as a fibre matt, it is estimated that the cut-off size lies in the 100 nm range [Hagler et al., 2007].

Since the wet UV photo-oxidation for DOC extraction reportedly does not oxidise the POC fraction by all means [Preunkert et al., 2011], several methods do not separate POC from the sample prior to UV oxidation [Legrand et al., 2007; Preunkert et al., 2011; Legrand et al., 2013a,b; May et al., 2013]. For polar ice samples, with a generally low relative POC concentration, the induced error may be negligible compared to other un-

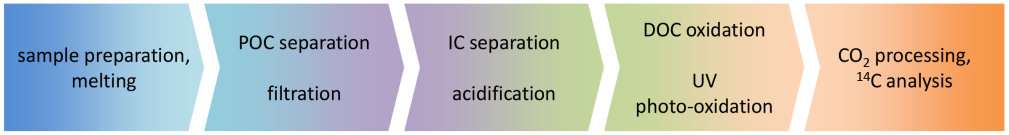

Figure 1.7: Flowchart of the different steps and methods used for the extraction of DOC from glacier ice to a CO_2 sample that can be analysed for ^{14}C.

certainties [Legrand et al., 2013a]. However, it is important to declare the analysed fraction of OC: TOC, DOC or the 'UV oxidisable OC'.

1.5.3 Removal of inorganic carbon

In a next step, IC needs to be removed as it originates from a different carbon pool than OC and would bias the DO^{14}C result. In the liquid sample, CO_2, carbonic acid (H_2CO_3), bicarbonate ions (HCO_3^-) and carbonate ions (CO_3^{2-}) exist in a pH-driven chemical equilibrium. Lowering the pH by acidification shifts the carbonate equilibrium: at a pH value of 2 almost all IC is in the state of dissolved CO_2 [Sharp, 2002] and can be removed by degassing of the solution.

Phosphoric acid (H_3PO_4) proved to be specifically suitable for the acidification of the solution thanks to its lower volatility and strength compared to hydrochloric acid, limiting unwanted oxidation and corrosive side products [Lang et al., 2012; Beaupré et al., 2007].

Bubble degassing extracts the dissolved CO_2 by diffusion to a carrier gas that is sparged through the solution. This is the most straightforward technique for degassing and decreases the CO_2 and IC concentration of the solution exponentially.

CO_2 can also be separated with a semi-permeable membrane as used in flow-through systems [Federer et al., 2008]. However, since the applied membranes consist of plastic material and introduce additional surfaces to the setup, bubble degassing allows a higher degree of contamination control and is in addition not vulnerable to plugging.

It has to be noted that volatile organic species can be lost in parallel with IC removal, however their contribution to the total DOC load is small [Sharp, 2002].

1.5.4 Oxidation of dissolved organic carbon

Several methods exist for the oxidation of the DOC in the solution to a CO_2 sample for ^{14}C analysis with AMS. The most suitable method has to

be chosen in terms of possible contamination, expected sample size and oxidation yield.

Historically, DOC was first used as a proxy in seawater and freshwater research. Early measurements were performed by oxidising DOC with the help of oxidants such as hydrogen peroxide or potassium persulphate [Duursma, 1961; Menzel and Vaccaro, 1964]. Although this is suitable for large sample volumes and even isotopic analysis has been performed using this wet chemical oxidation technique, the use of chemicals imposes the risk of sample contamination and no complete DOC oxidation is attained [St-Jean, 2003; Lang et al., 2012].

A full and rapid oxidation is achieved by the high temperature combustion, a technique widely used for automated laboratory applications [St-Jean, 2003; Sugimura and Suzuki, 1988]. While this method has also been used for isotopic analysis, small sample sizes restrict its use to samples with higher DOC concentrations than typically found in glacier ice [Lang et al., 2007].

le Clercq et al. [1998] developed a setup for the oxidation of DOC in the supercritical state of water at 350 bar and 650 °C. Despite technical challenges it is especially suitable for seawater samples as salts do not precipitate in this state.

Dry combustion has been used in past studies, involving lyophilisation of the sample and sealed-tube combustion with the help of a catalyst [Fry et al., 1996; Loh et al., 2004]. The complex sample handling increases the risk of contamination and possible loss of material in the drying step has to be considered with this method.

The photo-oxidation of liquid samples by UV radiation has been used for several applications for radiocarbon microanalysis of DOC from ice samples [May, 2009; Steier et al., 2013] and is minimal invasive. Widely applied for waste-water treatment [Oppenländer, 2007], this method has the advantage that no chemicals need to be added as the oxidants are produced within the solution itself by the irradiation. Apart from comparably long sample processing times, large sample volumes can be handled. Two groups can be distinguished according to the type of UV source and its resulting radiation spectrum.

Low-pressure mercury (Hg) lamps emit at the two distinctive wavelengths of 185 nm and 254 nm and have only low power below 100 W [Schalk et al., 2006]. The 185 nm line produces hydroxyl radicals from the water which then oxidise the DOC [Golimowski and Golimowska, 1996]. Several systems applied this technique for the measurement of DOC concentrations

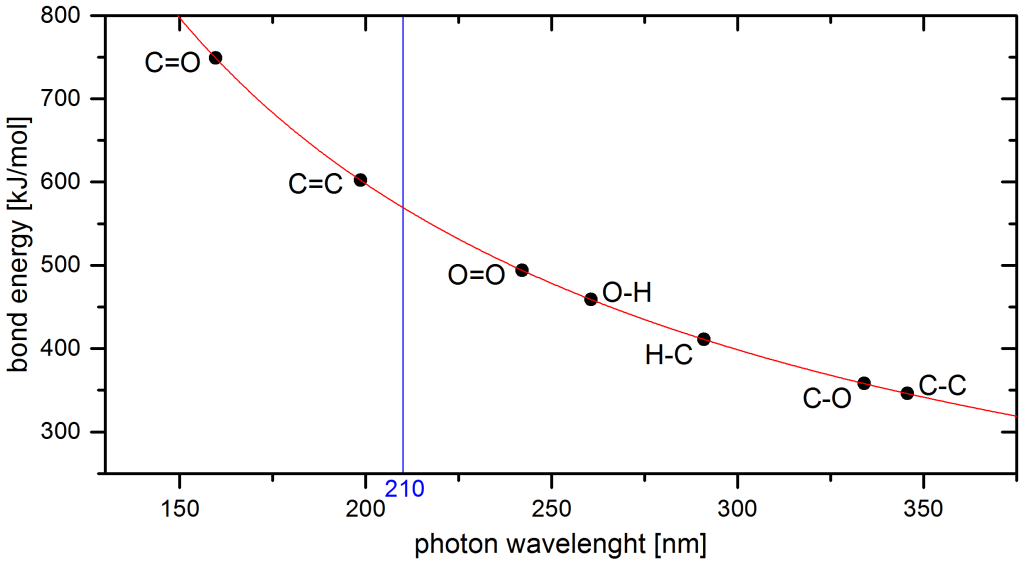

Figure 1.8: Average bond energy at 0 °C versus photon wavelength for photo-dissociation of a molecular bond. Raw data from Petrucci et al. [2016], the blue line at 210 nm indicates the lowest wavelength of the high-pressure Hg lamp that we use in our work (see also Sec. 2.3.2).

[Federer et al., 2008; Preunkert et al., 2011] as well as for radiocarbon analyses of DOC from glacier ice [May, 2009; Steier et al., 2013].

The advantage of medium- and high-pressure Hg lamps is their higher photon flux thanks to their higher power of up to several kW. However, their spectrum does not reach as far into the vacuum UV range as for low-pressure Hg lamps, limiting the maximal photon energy. Still, with a rich spectrum down to 200 nm [Schalk et al., 2006], their radiation can produce hydroxyl radicals and can also directly dissociate intra-molecular bonds of most organic compounds without the need of additional oxidants or catalysts [Golimowski and Golimowska, 1996; Weast and Astle, 1982]. Fig. 1.8 shows the average bond energy of typical molecular bonds of organic compounds and the respective wavelength for photo-dissociation. High-power UV irradiation systems were the first ones used for isotopic DOC analyses of seawater [Armstrong et al., 1966; Williams et al., 1969] and later also of freshwater including studies of glacial water [Stubbins et al., 2012; Raymond and Bauer, 2001]. Whereas early studies had to oxidise large sample volumes, the advent of AMS technology allowed substantial reduction of sample volumes and irradiation times [Williams and Druffel, 1987; Bauer et al., 1998; Beaupré et al., 2007].

1.6 Aim of this work

In this work, we developed and constructed a setup for ultra-clean DOC extraction from ice samples to further improve the sensitivity, precision and application spectrum of radiocarbon dating of ice cores. Compared to the well-established method of PO^{14}C analysis in ice and firn, the use of the DOC fraction promises several advantages. The higher concentrations of DOC allow to analyse smaller samples or samples with lower OC concentrations, such as polar ice samples. Furthermore, for the ^{14}C analysis, the signal-to-noise ratio is increased and the procedural blank contribution is not as limiting as for POC. DOC comprises reactive molecules that only show a reduced reservoir effect and represent a contemporary carbon source for dating. The intended application of this new method is, apart from DOC concentration measurements itself, the dating of ice samples from pre-industrial times back to more than 10 000 years BP. This suits the typical age range of alpine ice cores and helps to establish dating in sections of the ice core where common dating methods such as annual layer counting or the assignment of reference horizons are strongly limited or fail.

To meet the requirements for ultra-clean extraction of large samples with isotopic fidelity, we developed the extraction setup as follows: ice samples of up to 450 g are rinsed and melted under inert gas conditions in a melting vessel and transferred to a photo-reactor, passing a quartz filter. This step separates the POC fraction which can be additionally analysed with the standard PO^{14}C method. The filtrate is acidified and IC is removed by bubble degassing with helium. To oxidise the DOC to CO_2, external UV irradiation with two 250 W medium-pressure Hg lamps is applied. The high UV transmission of the quartz glass photo-reactor allows a minimal invasive oxidation with high efficiency within 45 min. Evolving CO_2 is degassed and led through cryogenic traps for separation from water vapour and the carrier gas itself. The manometric determination of the CO_2 mass in combination with the known fill level of the photo-reactor allow to measure the DOC concentration. Finally, the CO_2 is sampled to glass vials for ^{14}C analysis with the GIS and MICADAS AMS.

For the correct interpretation and application of this new method, extensive characterisation of the oxidation efficiencies, the overall CO_2 recovery and most important the procedural blank mass and its isotopic signature are needed. For this, we operated the system with dedicated liquid standard substances and blank ice samples. To proof the working principle,

we performed a validation study using ice from the well-dated Juvfonne ice tunnel, including a direct comparison with the PO^{14}C method.

This thesis is structured as follows. A broad introduction to the context and techniques of this work is given in this chapter. Chapter 2 explains the construction and concept of the extraction setup in detail. A thorough characterisation of its performance and benchmarks is found in Chapter 3. First measurements of glacier ice samples are used for a validation study presented in Chapter 4, before concluding remarks and an outlook are drawn in Chapter 5.

Chapter 2

Setup

Because of the specific challenges for radiocarbon analysis of DOC from ice samples such as the low carbon concentrations and its vulnerability to contamination, a sophisticated extraction setup is needed. To meet the requirement of processing large samples with low and stable procedural blank, we chose a system that can handle ice samples completely in inert gas and uses the minimal invasive UV photo-oxidation technique. In this chapter we present the extraction setup and its working principles in detail.

2.1 Concept and Overview

As discussed in Sec. 1.4.2, DOC concentrations in glacier ice are in the range of 10 to 100 μg C/kg ice [Legrand et al., 2013a]. With current state-of-the-art AMS analysis of gaseous CO_2 samples, carbon masses of as low as 3 μg are sufficient for dating (see Sec. 1.3.4 and Ruff et al. [2007]), what translates to typical required ice sample mass of several 100 g. This is relatively large considering that an ice core that was drilled with the electro-mechanical drill FELICS [Ginot et al., 2002; Schwikowski et al., 2014] has a diameter of 80 mm and annual layers can reach the sub-cm range due to layer thinning in the lower part of the ice body. Since the available ice mass is limited while DOC concentrations are low, a method with high yield is vital. Furthermore, DOC is prone to contamination, in particular when handling a liquid sample (see Sec. 1.5.1). Thus, for microgram radiocarbon determination with isotopic fidelity, the need for an ultra-clean and efficient extraction setup is even more pronounced.

After sample preparation in the cold lab and a first decontamination by rinsing with ultra-pure water (UPW)[1] in a laminar flow box, the ice sample is solely treated in an inert gas atmosphere to prevent contamination by the uptake of organic gases or particles from laboratory air. For further cleaning, melting, filtration and oxidation an all-glass setup is used that allows to handle the sample without any contact to carbon containing materials. This minimises carbon input by out-washing of organic compounds from synthetic material [Preunkert et al., 2011; Druffel et al., 2013]. By the photo-oxidation, DOC is transformed to CO_2 and thus is less sensitive to contamination. Still, the processing of the gaseous sample is carried out in a stainless steel vacuum line with the reduced use of O-rings and without the use of any lubricants to minimise possible contamination from out-gassing. For a minimal invasive oxidation with a high yield, we chose the UV photo-oxidation technique. To provide a high photon flux, we use two medium pressure Hg lamps with a power of each 250 W. The photo-reactor is irradiated externally and fabricated from UVC-transparent quartz glass to allow for efficient oxidation (see Sec. 1.5.4).

Fig. 2.1 shows a schematic of the complete extraction setup. In a brief overview, the following steps are performed for the extraction of DOC from ice: a pre-cleaned ice sample is inserted into the pre-cleaned glass melting vessel and flushed with ultra-high purity (UHP) helium. After rinsing with UPW, which is discarded, the sample is transferred to the pre-cleaned photo-reactor passing a quartz filter. In the photo-reactor, the liquid sample is acidified and is degassed to a vent. During the subsequent photo-oxidation, the carrier gas stream is led through two cryogenic traps that retain water vapour and one further cryogenic trap that captures the CO_2 sample from the gas stream. In the vacuum line the CO_2 is further cleaned and its mass is determined manometrically. In a last step, the CO_2 is sampled in a glass vial for ^{14}C analysis with the GIS and MICADAS.

The following, detailed description of the individual components refers to Fig. 2.1 and the nomenclature used in the figure. To facilitate the reference, we highlight components that are indicated in green text in the figure in *italics* when used for the first time in the text.

[1] Resistivity $\geq 18\,\mathrm{M\Omega cm}$.

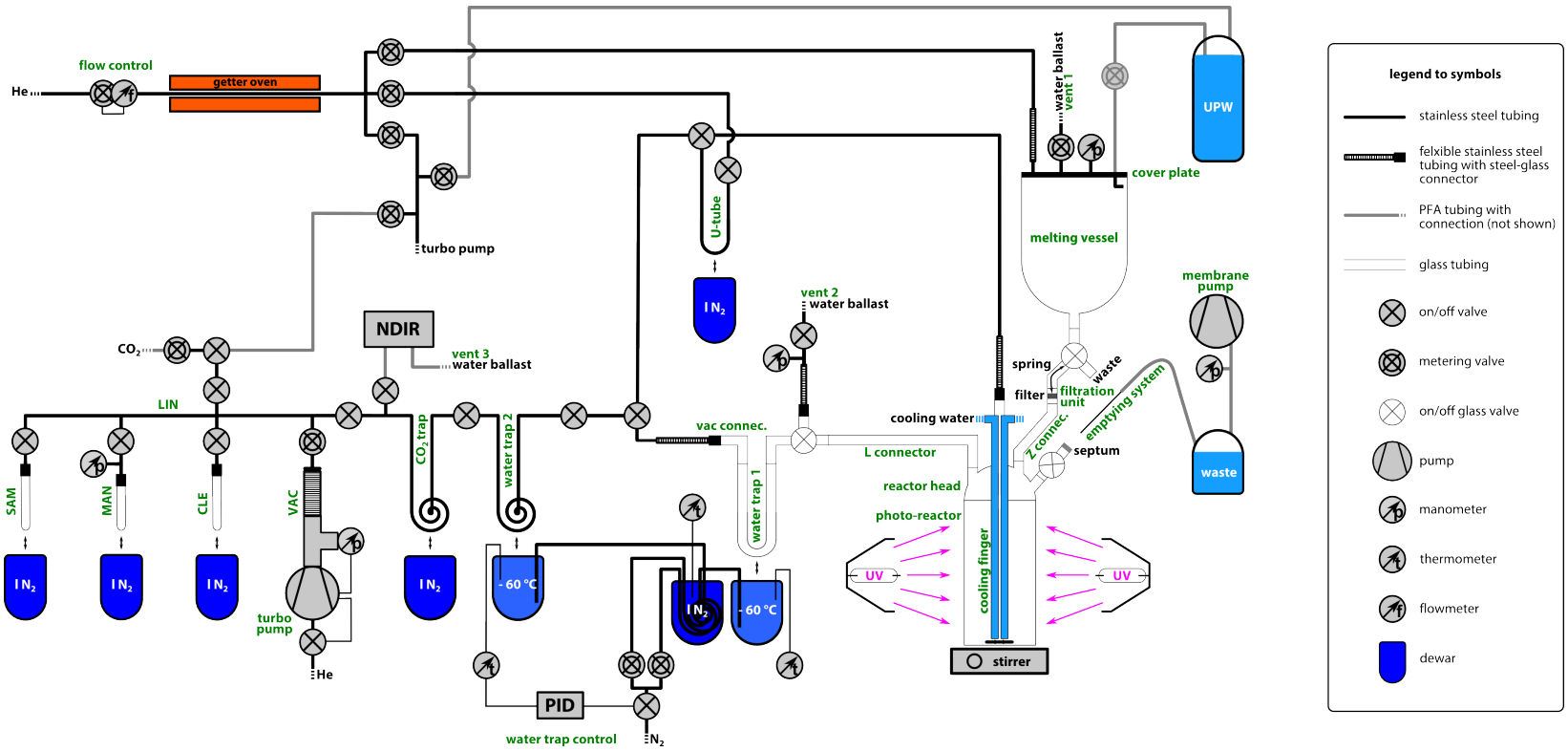

Figure 2.1: Schematic of the complete extraction setup. Black text indicates additional hardware that is not shown, green text labels individual components. UPW (ultra-pure water), lN_2 (liquid nitrogen), PID (temperature controller), NDIR (CO_2 detector), LIN (vacuum manifold), VAC (pump manifold), CLE (cleaning tube), MAN (manometry cell), SAM (sampling tube).

2.2 Melting vessel and filtration unit

In the *melting vessel*, the ice sample is introduced to the extraction setup, further cleaned and melted. The *filtration unit* allows the separation of POC from the liquid sample under inert gas conditions.

2.2.1 Glass setup

The handling of the liquid sample after ice melting until DOC oxidation is performed solely in a demountable all-glass setup (see Fig. 2.6 a)). The complete glass setup was custom-made by GlasKeller Basel AG (see App A for a list of suppliers for all specific compounds). Except for the photo-reactor, all parts are manufactured from borosilicate 3.3 glass. The use of glass has several advantages: it can be easily and thoroughly cleaned and its transparency allows to monitor the sample and to detect any visible contamination. Furthermore, memory effects from water molecules remaining at the surfaces are less pronounced for glass than for stainless steel.

Except for the cover plate and the photo-reactor where we use flat flanges, all connections of individual glass parts are realised with spherical joints (SJ). Apart from a large surface area for sealing, the spherical shape allows to angle different components. This is not only user friendly, but this possibility to bend gives flexibility to the otherwise stiff construction and reduces the danger to break glass.

Commonly, ground glass joints are sealed with organic lubricants. In order to avoid sample contamination by leaching of lubricants we use phosphoric acid (H_3PO_4) instead, similar to Beaupré et al. [2007]. As we confirmed in a pilot study, H_3PO_4 is suitable for sealing and greasing ground spherical glass joints, ground flat flanges and ground stopcocks thanks to its high viscosity. It does not suffer strong evaporation and thus avoids jammed connections. Last, and most important, since H_3PO_4 does not contain any carbon, sample contact or out-washing are no issue of contamination, provided high quality H_3PO_4 is used.

2.2.2 Ultra-high purity helium supply

Helium is used both as inert gas and as carrier gas. Therefore, an UHP supply of helium is essential to prevent sample contamination. Helium of 5.0 quality[2] is provided by the in-house supply and purified further by a home-made getter oven. The getter oven consists of an insulated, resistively

[2]Purity $\geq$ 99.999%

heated Inconel[3] tube filled with 15 g tantalum wire. A VARIAC[4] power supply powers the oven and is controlled by a proportional-integral-derivative (PID) controller to constantly heat to 950 °C. At this temperature, tantalum reacts with carbon containing impurities from the gas stream and binds them chemically [Espe et al., 1950], resulting in a UHP helium gas stream.

As shown in Fig. 2.1, a *mass flow controller* (MFC) is installed prior to the getter oven for a precise gas flow-rate, independent of the source pressure. Both in front of the MFC and downstream of the getter oven, a 10 μm stainless steel filter and a sinter filter are used to ensure a particle-free gas supply (not shown). The UHP helium emerging the getter oven is distributed via metering valves to i) the *turbo pump* ventilation valve, ii) the vacuum line, iii) the UPW dispenser system, iv) the *photo-reactor* via the *cooling finger* and to v) the melting vessel.

In contrast to other studies that utilised synthetic air [May, 2009] or pure oxygen [Steier et al., 2013], we chose helium as carrier gas. Although it does not promote the photo-oxidation such as oxygen via the formation of ozone, UHP helium can easily be produced as described. However, most important, the separation of CO_2 from the helium gas stream can be performed with simple cryogenic traps that are submerged in liquid nitrogen (lN_2) (see 2.4). Oxygen has a lower vapour pressure and would freeze at -196 °C, therefore, either more complicated, warmer cryogenic baths (2-methylbutane slush bath operating at -136 °C [Szidat et al., 2004]) or a heated platinum catalyst [May, 2009] would have to be used for the separation of CO_2 from the carrier gas stream.

2.2.3 Melting vessel

The melting vessel, as shown in Fig. 2.2 a) and Fig. 2.6 b), is a glass vessel of 100 mm inner diameter and has a volume of approximately 1.3 l. Its top is open and connects with a DN 100 flat flange to the stainless steel *cover plate*. A support holds the vessel and fixes the cover plate to the vessel by spring tension. The flange connection is sealed by a PFA coated O-ring, that does however not touch the liquid sample.

As illustrated in Fig. 2.1, the cover plate gives access to several connections via 5 holes with $G^1/_4$ inch thread: i) the helium supply, ii) a metering valve with a bubble counter that acts as a vent with water ballast (*vent 1*), iii) a manometer for pressure monitoring and iv) the UPW supply.

[3] A high temperature resistant nickel-chromium-based super-alloy
[4] A variable AC voltage controller

The UPW dispenser system consists of a glass bottle that is filled with UPW and that is connected to both the helium supply and the cover plate with PFA tubes. By applying pressure via the helium supply, UPW is pushed to the melting vessel, where a bent water outlet dispenses the UPW to the side wall of the vessel. The UPW bottle has to be refilled manually from our UPW system[5].

The base of the melting vessel is curved and provides an outlet with a SJ 29/15 connection. As shown in Fig. 2.2 a) and Fig. 2.7 a), a 3-way all-glass valve is connected to the melting vessel outlet. The valve either seals the melting vessel, directs the flow to the waste outlet or leads the sample to the filtration unit.

2.2.4 Filtration unit

The filtration unit as shown in Fig. 2.2 a) and Fig. 2.7 a), is shaped as an adapter piece from SJ 41/25 to SJ 19/7. In the centre, a frit of 8 mm diameter with porosity 0 [6] serves as a support for a quartz fibre filter with a diameter of 20 mm. In the same way as for PO^{14}C analysis [Jenk et al., 2006], a quartz fibre filter that had been pre-cleaned by baking at 800 °C for 4 hours is used for the separation of POC from the liquid sample.

In contrast to common lab vacuum filtration units, this setup allows filtration at inert gas conditions thanks to its self-contained design. Without proper sealing, the filtration would lead to a strong mixing of the sample with ambient air and thus contaminate the liquid sample, as observed in a pilot study with a common lab vacuum filtration unit.

To fix the quartz fibre filter, we use a stainless steel spring that is restrained between the frit and the 3-way glass valve. The spring is the only non-glass component that does touch the liquid sample, but is necessary for a flexible fixation of the filter in the otherwise stiff setup.

The *Z connector*, a Z shaped glass tube connects the filtration unit with the reactor head. This adaptor piece provides a horizontal offset of the axes of melting vessel and photo-reactor. In combination with the bendable spherical joints, this design endows the stiff glass setup with vertical flexibility. This reduces strain in the glass parts and makes the assembly more user-friendly.

[5] 'Milli-Q Direct with UV lamp', Merck Millipore
[6] Pore size 160 – 250 μm

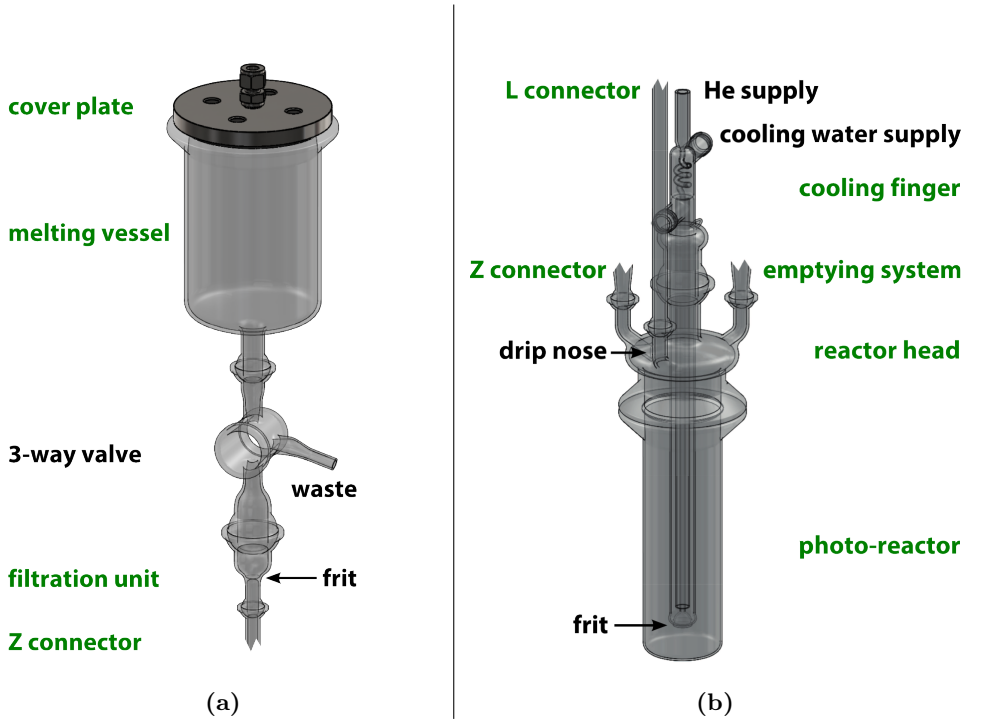

Figure 2.2: View of (a) melting vessel, filtration valve and filtration unit and (b) the photo-reactor, reactor head and cooling finger. Green text refers to the labelling introduced in Fig. 2.1, black text refers to connections or emphasises special features.

2.3 Photo-reactor

After melting and filtration, the sample is acidified and degassed from IC in the photo-reactor. By external UV irradiation, DOC is photo-oxidised to CO_2 and degassed with a helium carrier gas flow. The carrier gas is dried from water vapour by passing two cryogenic traps before the CO_2 is retrieved in the vacuum line.

The principle design of the photo-reactor was inspired by and adapted from the extraction setup of Beaupré et al. [2007].

2.3.1 Reactor head and cooling finger

The *reactor head* serves as an adapter to the four connections that enter and exit the photo-reactor. It is fabricated from Boro 3.3 glass and connects to the photo-reactor with a ground flat DN 60 flange that is sealed with H_3PO_4. Both parts are held and fixed to each other by a support and spring tension. As illustrated in Fig. 2.1 and Fig. 2.2 b), the Z connector, the *L connector*, the *emptying system* and the cooling finger are attached to the reactor head by ground spherical joints.

Via the Z connector the liquid, filtered solution is introduced to the photo-reactor. The arm that attaches the Z connector to the reactor head is prolonged inside the reactor head and finishes off with a drip nose (highlighted in Fig. 2.2 b)). This is a simple, yet important detail as it leads the sample directly into the photo-reactor and prevents it from flowing along the reactor head wall and into the flat flange connection.

In the centre of the reactor head, the cooling finger is inserted via a SJ 41/25 connection and reaches down close to the base of the photo-reactor. The cooling finger has several functions. It is constructed from three concentric glass tubes. The outer two tubes serve as a pipe to lead cooling water down and back up along the cooling finger. GL 14 glass threads allow to connect the in-house cooling water supply. The cooling water flow can be monitored via a flow meter and is additionally stabilised by a thermostat. In combination with external cooling by air ventilation, this internal cooling is essential to reduce the sample temperature and thus the unwanted production of water vapour during the photo-oxidation (see Sec. 2.5).

The innermost glass tube of the cooling finger delivers UHP helium to the base of the photo-reactor for the degassing of the liquid sample. The helium supply connects with a steel–glass adapter piece[7] to the top of the cooling finger. As illustrated in Fig. 2.2 b), the innermost tube is spiral-shaped in the top section to compensate for thermal stress. This is necessary since the different wall thickness of the different tubes could otherwise cause glass breakage due to temperature gradients. The helium supply tube finishes off with a frit of porosity 4 [8]. The frit creates small helium bubbles, which increase the bubble degassing efficiency of the liquid sample and reduces inflow of the liquid sample into the helium supply tube.

The L connector is a simple glass tube that leads the carrier gas from the photo-reactor towards the vacuum line. It connects to a 3-way valve with three cryogenic traps further downstream.

The fourth port of the reactor head is used for the emptying system. Here, a 2-way valve with SJ 19/7 connection to the reactor head and a 10 mm open ended glass tube on the other side has the function of an airlock. A silicone septum plugs the glass tube end and gives access to a long stainless steel needle. The needle can reach down to the very base of the photo-reactor and is connected to a *membrane pump* in a Woulff bottle style configuration (see Fig. 2.1). This setup allows to empty the photo-

[7] A custom made adapter from a 6 mm steel tube to a 10 mm glass tube, similar to the Ultra-Torr vacuum fittings supplied by Swagelok. By tightening a screw-nut, 2 O-rings are pressed against the glass tube and seal the connection.

[8] Pore size 10 – 16 μm

reactor by drawing out the sample with the emptying syringe. Thanks to the airlock created by the septum and valve, this abstraction involves virtually no introduction of ambient air. The 2-way valve closes off septum and photo-reactor so that during the UV photo-oxidation step no synthetic material is in contact with the sample or its head space volume. However, it has to be noted that in this first version of the setup a PTFE valve plug was used for practical reasons of availability. The same holds true for the valve plug of the 3-way valve following the L connector. However, both valves are designed as all-glass valves and could easily be exchanged in the future.

2.3.2 Photo-reactor and UV source

The photo-reactor is the heart piece of the glass setup. Since we perform the UV photo-oxidation of the liquid sample by external irradiation, it is crucial to choose suitable glass for the manufacture of the photo-reactor. In general, quartz glass is UV-transparent in contrast to common glass types such as Boro 3.3. Doping of the quartz glass can further promote its ability to transmit radiation in a broad range of wavelengths in the UV range. In match with the emission spectrum of the used Hg medium-pressure lamps, we chose ilmasil PS, a quartz glass with high transparency down to below 190 nm [Qsil GmbH, 2012], manufactured by Qsil GmbH.

The photo-reactor itself consist of a cylindrical glass vessel with flat, closed base and a DN 60 ground flat flange at the top. The flange is a standard component and transition glasses have to be used to fit the quartz glass cylinder to the flange. Thus, although the overall height of the photo-reactor is 200 mm, only the lower 110 mm consist of pure quartz glass. The cylinder has a diameter of 60 mm and a wall thickness of 2 mm.

To mix the sample and promote homogeneous oxidation and efficient degassing, we use a magnetic stirrer. The magnetic stir bar is encapsulated in glass to avoid contamination. As described in Beaupré et al. [2007], the glass casing has two circular sliding rails that reduce friction on the base of the photo-reactor and ensure a stable spinning of the stir bar.

Once completely assembled with stir bar and cooling finger, the photo-reactor can handle liquid samples of up to 350 ml volume. To determine the DOC concentration, both the DOC carbon mass as well as the sample volume have to be known. The latter is measured with a home-made calliper to determine the fill level of the photo-reactor. With the help of a calibration curve consisting of 2 linear regression lines, the sample volume can be determined (see App. C).

As described in Sec. 1.5.4, many different UV sources are available with their individual strengths and disadvantages. Because of the high power and easy handling, we chose medium-pressure Hg lamps. The MH-Module 250W Hg XL from Heraeus, consists of a medium-pressure Hg lamp that is installed inside of an infrared (IR) transparent UV reflector. In this way, the lamp axis can be installed perpendicular to the photo-reactor. Thus, the IR radiation emitted by the lamp transmits through the reflector and does not directly heat the photo-reactor. Nevertheless, the UV radiation is reflected and directed towards the photo-reactor for the photo-oxidation. As mentioned above, this contributes to minimize the heat uptake of the liquid sample.

Both lamp modules are installed opposite of each other and embrace the photo-reactor in 3 cm distance. The protection box that surrounds photo-reactor and UV lamps enhances the photon-yield further thanks to its reflective aluminium construction. We use two MH-Modules with a power of 250 W each, featuring a rich emission spectrum down to 210 nm [Heraeus Noblelight GmbH, 2012], see also Fig. 1.8.

The medium-pressure Hg lamps have to be operated with an igniter and a ballast, the corresponding circuit diagram is found in App. B. A photograph of photo-reactor, UV lamps and calliper is shown in Fig. 2.7 b).

2.3.3 Cryogenic water traps

The helium carrier gas is led via the cooling finger through the liquid sample in the photo-reactor for bubble degassing. Before passing through a cryogenic trap for CO_2 extraction in the vacuum line (Sec. 2.4), it is dried from water vapour in two consecutive cryogenic water traps. This is essential as the sample is heated by the photo-oxidation and thus the carrier gas is humid. However, a high water content would hamper the reproducible and efficient extraction of CO_2 from the carrier gas stream.

As illustrated in Fig. 2.3, a 3-way valve connects to the L connector. One flow path leads to a metering valve with a bubble counter that acts as a vent with water ballast (*vent 2*). The vent is connected by a steel–glass adapter and comprises a simple manometer to monitor the pressure inside the glass setup. Vent 2 is used as a direct exhaust without passing the cryogenic traps for the cleaning and IC degassing steps.

The other flow path of the 3-way valve leads the carrier gas stream though *water trap 1* and *water trap 2* which are interconnected by the *vac connector* and a steel–glass adapter. Water trap 1 is a U-shaped, 200 mm long glass tube with 10 mm inner diameter and SJ 19/9 connections at both

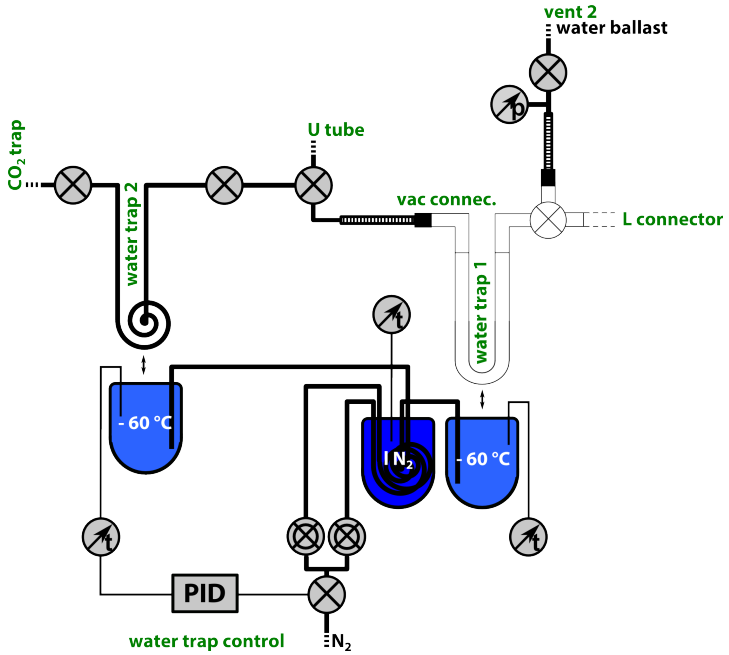

Figure 2.3: Excerpt from Fig. 2.1 showing the cryogenic water traps and the cold gas system.

ends. Its downstream leg is filled with glass capillaries to increase the surface area for enhanced thermal contact with the passing carrier gas. Water trap 2 is a 2 m long, 6 mm outer diameter (OD) stainless steel tube that is bent to a coil.

To freeze out water vapour from the carrier gas stream, both water traps are immersed in cooling baths that are filled with cold nitrogen. For the selective removal of water vapour without affecting the CO_2, the cooling bath temperature has to be well below 0 °C and above -80 °C. Commonly used for such applications are slush baths, e.g. an Ethanol – dry ice (solid CO_2) mixture that has a temperature of -72 °C. However, they require careful use, frequent monitoring and involve potentially dangerous chemicals. Therefore, we use a home-made cold gas system (*water trap control*) for the stable, long-term supply of cold nitrogen with defined temperature as a coolant for the cooling baths.

The principle layout of the cold gas system is illustrated in Fig. 2.3, the detailed circuit diagram for the PID temperature control is found in App. B. The system relies on the controlled transfer of nitrogen through a heat exchanger to the cooling bath. A PID controller measures the cooling bath temperature; whenever this temperature is above the manually adjustable set-point, it opens a magnetic valve and thus cooled nitrogen flows to the

cooling bath. The nitrogen is cooled upstream in a heat exchanger coil that is situated in a bath of liquid nitrogen. Once enough cold nitrogen is supplied to the cooling bath such that the set-point is met, the PID controller closes the valve. By this controlled influx of cold nitrogen, a stable temperature for the long-term operation of the cryogenic water traps is maintained.

To extend the system for the use with two cooling baths, we installed a second heat exchanger plus a cold nitrogen supply line to water trap 1. It is manually coupled to the PID control-circle of water tap 2: downstream of the magnetic valve, the line is split and two metering valves allow to tune the fraction of nitrogen that is led through each of the two supply branches. If set correctly, both cooling baths are PID temperature controlled to the same temperature, one directly, the other one indirectly by the gas splitting.

The system is very user friendly and can provide a long term temperature stability of $\pm$ 0.2 K at an operation temperature of -60 °C. Depending on the volume of the liquid nitrogen reservoir, its refilling is required every few hours. We use a thermometer to monitor the fill level of liquid nitrogen.

2.4 Vacuum line

In the vacuum line the CO_2 from the oxidation of DOC is recovered from the carrier gas stream, is cleaned, quantified and packaged in glass vials for subsequent ^{14}C analysis. In its function and its principle layout, the vacuum line is similar to the vacuum line employed for the THEODORE system [Szidat et al., 2004].

Except for the cryogenic *CO_2 trap* that operates at ambient pressure for the CO_2 extraction, the vacuum line works at high-vacuum conditions at around 10^{-7} mbar. To facilitate ultra-clean high vacuum conditions, we chose only dedicated materials. All compounds were cleaned thoroughly before assembly in several ultrasonic baths (acetone, methanol or isopropanol and UPW) and all steel compounds except the valves were additionally baked in vacuum. Most components are based on 6 mm OD stainless steel tubes and stainless steel Swagelok tube fittings. Except for the steel–glass adapters and Klein Flange connections for the turbo-molecular pump, no O-rings are used. To prevent contamination from out gassing lubricants, only full-metal bellow-sealed valves were employed (Swagelok BN4-, BM- and H- series). To minimize wear, we use valves with on/off function wherever applicable and dosing valves only where needed.

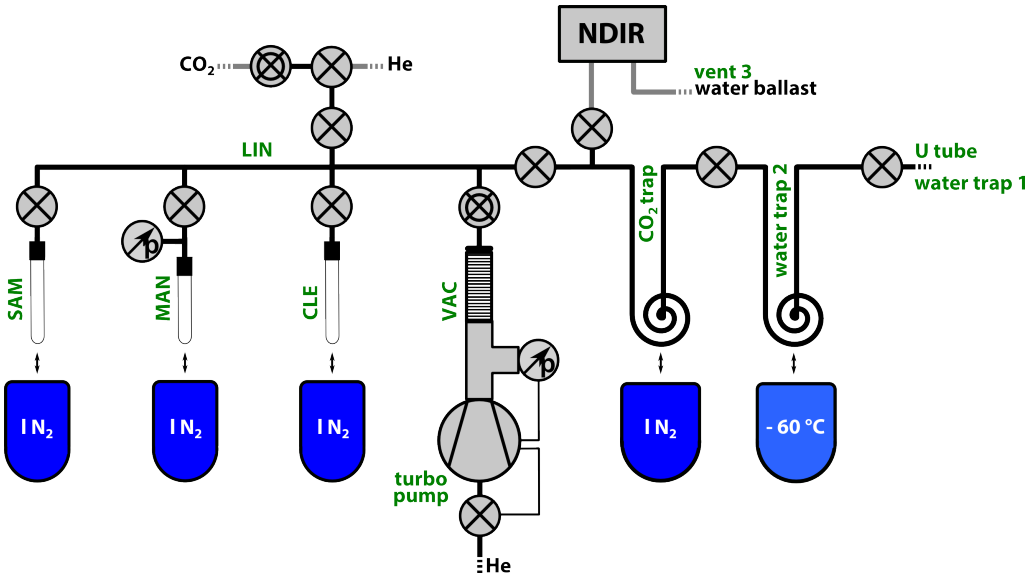

Figure 2.4: Excerpt from Fig. 2.1 showing the vacuum line.

As sketched in Fig. 2.4 (see also photograph in Fig. 2.9), after drying in the cryogenic water traps, the carrier gas stream is transferred to the cryogenic *CO_2 trap*. The trap is made from two connected, 2 m long, 6 mm OD stainless steel tubes that are bent as two interleaved coils. The coils can fit into a cooling bath that is filled with liquid nitrogen. At this temperature (-196 °C), CO_2 is frozen to the trap surface while the carrier gas, helium, passes the trap unaffected.

In flow-through mode, the carrier gas is lead through the trap and exits the setup via *vent 3* after passing a non-dispersive infrared (NDIR) CO_2 detector[9] and a bubble counter that acts as water ballast. With this configuration it is possible to monitor the CO_2 content in the carrier gas stream whenever the cryogenic trap is inactive. Once the trapping tube is immersed in the liquid nitrogen, CO_2 is retained in the trap and the CO_2-free gas stream that is vented from the setup can be monitored with the NDIR detector. After the extraction step, the CO_2 trap can be isolated and evacuated.

A turbo-molecular pump[10] establishes high-vacuum conditions while its oil-free operation guarantees clean operation. It is equipped with a Pirani gauge[11] for pressure measurement and a venting valve[12] for automatic vent-

[9] Model 'LI-820A' from LI-COR
[10] Model 'HiCube 80 Eco' from Pfeiffer Vacuum AG
[11] Model 'PKR 251' from Pfeiffer Vacuum AG
[12] Model 'TVF 005' from Pfeiffer Vacuum AG

ing with the connected UHP helium. The vacuum pump is connected to the vacuum line with a dosing valve and KF 40 components that allow efficient pumping thanks to their large diameter of 40 mm (*VAC*). With the dosing valve, it is possible to regulate the gas flow to the pump, what avoids abrupt shock waves that result in high pump loads and possible damages of the vacuum pump.

A central manifold (*LIN*) connects the CO_2 trap, vacuum pump, cleaning tube (*CLE*), manometry cell (*MAN*) and sampling tube (*SAM*). The CO_2 sample can be moved in vacuum from one trap to another by cryogenic pumping: the removal of the liquid nitrogen bath releases the frozen sample from the initial trap, the application of the liquid nitrogen bath to the new trap fixes the sample at the desired position. This mechanism is used to process the sample which was recovered in the CO_2 trap.

In a first step after evacuation of the CO_2 trap, the CO_2 is transferred to CLE. The cleaning tube consists of a 200 mm long, 8 mm OD glass tube that is connected to an on/off valve by a steel–glass adapter and sealed off on the lower end. The use of a glass tube for a cryogenic trap has apart from restrictions in flexibility several advantages. Glass has very low thermal conduction and thus the trapping region is well confined. Furthermore, its transparency allows visual monitoring of the trapping success.

In CLE, the CO_2 sample is first cleaned from more volatile compounds (mainly helium) by exposure of the frozen sample to high vacuum. After this, less volatile compounds (mainly water) are retained in the cleaning tube by installing a warmer ethanol – dry ice cooling bath with a temperature of -72 °C, while the purified CO_2 sample is transferred to MAN.

The manometry cell consists of a 150 mm long, 6 mm OD glass tube that is connected to an on/off valve by a steel–glass adapter and sealed off on the lower end. Furthermore, a T piece connects a piezo-resistive pressure transmitter[13] with front lying, planar membrane to avoid dead volume. The volume of the manometry cell is calibrated to $3.57 \pm 0.08\,cm^3$ (see App. C). Hence, according to the ideal gas law, by expanding the CO_2 sample into MAN at known temperature, its mass can be determined by measuring its pressure.

In a last step, the purified and quantified CO_2 sample is transferred to SAM. The sampling tube consists of a 4 mm OD glass tube that is connected to an on/off valve by a steel–glass adapter and sealed off on the lower end. Once the CO_2 sample is frozen to the lower end, we melt off a 70 mm long piece with the help of a gas torch. This sealed off glass vial contains the

[13]Model 'PBMN flush' from Baumer Electric AG

CO_2 sample which is ready for ^{14}C analysis with the GIS and MICADAS (see Sec. 1.3.4). The 4 mm OD glass tube is a consumable and can quickly be exchanged at the steel–glass adapter. A fresh glass tube can be cleaned by evacuation and external heating with a gas torch.

For vacuum line calibrations with CO_2, a CO_2 supply line is connected to the vacuum line via a dosing valve and a 3-way valve. To flush the vacuum line for cleaning or NDIR calibration, also the UHP helium supply connects to the 3-way valve.

The *U-tube* (see Fig. 2.1) is used for calibrations with gaseous CO_2. It can be loaded from the vacuum line via two 3-way valves and can be released to the photo-reactor by flushing it with helium from the UHP helium supply.

2.5 User protection

The extraction setup employs high-power UV radiation and electricity, both are potentially hazardous for the operator. Therefore, a safe and reliable user protection is vital.

To avoid electric shocks, all electronic devices are connected to the protective earth of the mains power supply according to common standards (see also App. B). Furthermore, since the acidified aquatic solutions that we work with are highly conductive and glassware is prone to breakage, also the metal rack that houses most of the setup is earthed with a large diameter ground line.

The two medium-pressure Hg lamps used for UV photo-oxidation of DOC pose several dangers to the user. Thus, to protect the operator whilst being user friendly, in a similar approach as Beaupré et al. [2007], we constructed a multifunctional protection box that houses the UV lamps and the photo-reactor.

The emitted short-wave, high-energy radiation is the direct threat of the UV lamps. In general, UV radiation is hazardous for eyes and skin. Furthermore, UVC radiation[14] damages nucleic acids, what is also the reason that it is applied for germicidal irradiation.

Therefore, as a general measure during work at the setup, it is obligatory to wear protective glasses and to cover the skin with a lab coat. A direct shielding from the radiation is given by the protection box: it is constructed by a frame made of aluminium profiles[15] and aluminium sheets with several in- and outlets, see Fig. 2.5 for photographs of the protection box setup

[14] Wavelength from 100 – 280 nm
[15] Model '30 mm Blocan' from Phoenix Mecano

and components. The top of the box is connected to the support of the photo-reactor. This is where the reactor head is attached to the exterior of the protection box. A plug with feed-through connects the UV lamps with their power supply. To protect the cable cladding from UV degradation, it is wrapped in aluminium tape. The UV lamps are fixed to the rack by aluminium rods. The photo-reactor is centred between the two lamps. In addition to the shielding from radiation, the protective box also enhances the efficiency of the UV lamps by reflecting the UV radiation to the photo-reactor in the centre.

The only major opening where harmful UV radiation can escape, is by passing through the UV transparent quartz glass photo-reactor to the reactor head that is outside of the protection box. However, the liquid sample in the photo-reactor absorbs most of the UV radiation. Any residual UV radiation should be blocked by the reactor head which is made from Boro 3.3 glass and thus non-transparent to UV radiation. Still, measurements with a radiometer[16] showed a 7% transmission of UV-C radiation through the reactor head. Therefore, we build an additional shielding around the reactor head that also reduces the overall light emission of the setup. Six connections enter and exit the reactor head, thus a flexible and easy mountable shielding is needed. This is realised with two triangular-shaped sleeve sheets that connect to the box and to each other with a Velcro fastener and efficiently shield the bright light from the UV lamps (shown as '12' in Fig. 2.5 b), see also photograph in Fig. 2.8 b)).

Besides the large amount of waste heat, an indirect threat of the UV lamps is ozone that is unintentionally produced by the UV irradiation of laboratory air. UVC radiation produces ozone by photo dissociation of oxygen following a recombination to ozone. This process is used for ozone generation in laboratory applications, but in our case unwanted for two reasons. First, ozone is a noxious gas and thus a health hazard for the operator. Second, ozone strongly absorbs UVB radiation[17], thus dims the UV radiation needed for photo-oxidation in the photo-reactor and thereby limits the efficiency of the setup.

To reduce ozone concentrations, we installed a ventilation of the protection box. Two air inlets on the front lid supply fresh air that is drawn through the protection box by a strong ventilator[18]. The air is vented to the fume hood via a 100 mm diameter flexible tube that is attached to the

[16] Model 'RM-12' with UV-C sensor from Opsytec Dr. Gröbel
[17] Wavelength from 280 – 315 nm
[18] Model 'TT 100 A' by Extravent with an airflow of 3.3 m^3/min

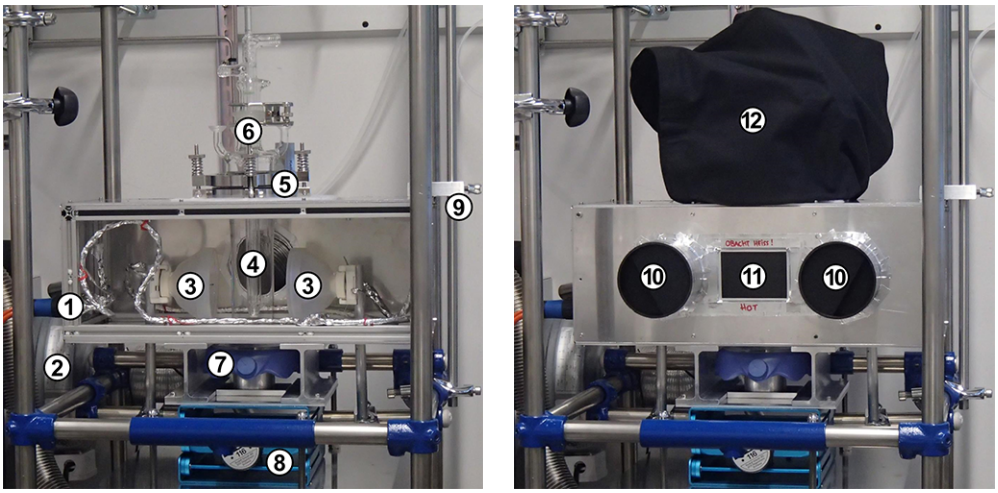

(a) **(b)**

Figure 2.5: Photographs of the protection box, (a) opened and (b) closed with front lid and sleeve. The numbers mark individual components: 1 plug for electrical supply, 2 ventilator, 3 UV lamps (electrical connections wrapped in aluminium and holders fixed to the rack below), 4 photo-reactor and air outlet to the ventilator in the back, 5 photo-reactor support, 6 reactor head with cooling finger, 7 magnetic stirrer, 8 lifting platform, 9 fixation, 10 air inlets, 11 window, 12 sleeve. For clarity, the setup is not fully assembled, actual connections would be fed through the sleeve.

rear wall of the box (shown as '10' in Fig. 2.5 b) and '4' in Fig. 2.5 a)). By drawing air through the box, leaks and the need for thorough air-sealing are circumvented. However, it is important to maintain the shielding from UV radiation. Therefore, we designed the air inlets in a convoluted layout and use aluminium parts that are anodised in black to absorb all light along the interlaced inlet path.

The two medium-pressure Hg lamps consume 500 W of power, yet only a fraction of it is emitted as UV radiation. Hence, a lot of waste heat needs to be dissipated. As mentioned (Sec. 2.3), the IR transmitting reflector of the used MH modules is designed to direct only UV radiation to the reactor while emitting IR radiation to its circumference. By this, the sample does only suffer limited heating and it is possible to dissipate the waste heat efficiently by air cooling. In this way, both the ozone ventilation and air cooling can rely on the same ventilation system. Further cooling is realised by the water cooling of the sample via the cooling finger (see Sec. 2.3).

The observed operation temperatures show that both cooling systems do work properly and that they are necessary: although the lamp sockets heat up to 150 °C, the temperature of the photo-reactor wall stays below 100 °C and the protection box is colder than 40 °C. Without the water cooling,

the liquid sample in the reactor would heat up to close to its boiling point during irradiation. However, with the active water cooling[19], the sample temperature rises only to a maximum of 40 °C.

Several further demands for user-friendly operation are met by the protection box. Since the glass setup is, apart from the movable Z connector, stiff in the vertical axis, a precise vertical alignment and flexibility are required for its assembly. Therefore, the protection box is mounted on a lifting platform that is movable in the vertical direction. To be stable, once installed in the right position, the box can be fixed to the rack by a locking screw (shown as '8' and '9' in Fig. 2.5 a)). In between the box and the lifting platform, the magnetic stirrer is fit to turn the magnetic stir bar inside of the photo-reactor (shown as '7' in Fig. 2.5 a)). Access to the protection box is given by the removable front lid which is fixed by ten screws. To monitor the photo-reactor during UV irradiation, a window is installed in the centre of the front lid (shown as '11' in Fig. 2.5 b), see also photograph in Fig. 2.8 a)). It is a welder's lens and blocks all UV radiation while a remaining fraction of visible light gives visual access.

2.6 Operation protocol

In a synthesis of the theoretical understanding (Chapter 1), the involved hardware (Chapter 2) and its characterisation (Chapter 3), the actual protocol for a reproducible and meaningful measurement was developed. Described in a very detailed and applied manner, App. D gives a step-by-step description of the operation protocol and is meant as a manual for the actual user of the extraction setup. In this section, we rather explain the conceptual outline and procedure of a measurement with the extraction setup. Again, all names refer to the nomenclature as shown at Fig. 2.1.

2.6.1 Ice sampling

By default, the respective ice samples need to be prepared in a first step. This is done similar as for the PO^{14}C method [Jenk et al., 2007]. In the cold room (T = -20 °C), ice blocks are cut and decontaminated by removing the outer layers with a stainless steel bandsaw. The required sample mass depends on the DOC concentration and can be as high as 500 g. For intermediate storage and transport to the laboratory, ice samples are put into

[19] Flow-rate 20 l/min, room-temperature warm water

polyethylene terephthalate glycol-modified (PETG) containers[20] that have been pre-cleaned three times by rinsing and soaking with UPW.

2.6.2 Preparation and installation

In general, a sufficient supply of UPW both for the wash bottles and the UPW dispenser system, of liquid nitrogen and of pre-baked quartz fibre filters[21] is needed. The quartz fibre filters are first punched to 20 mm large circles and then baked for 4 hours at 800 °C to remove any contaminants. Until usage, the filters are stored in the freezer, wrapped in aluminium foil. The PID controlled cooling baths for the two cryogenic water traps are set to operation since the cool down requires more than one hour of time. During the entire measurement, the fill level of the supplying liquid nitrogen reservoir has to be monitored and refilled if needed. Also the getter oven is powered and the helium supply line is flushed.

If not mounted from previous measurements, the complete glass setup needs to be installed (see Fig. 2.6 a)). Thanks to the spherical joints, flat flanges and steel–glass adapters, this is easy and quick, yet care has to be taken when handling with the H_3PO_4 that is used for sealing. A fresh quartz fibre filter is installed together with the spring for fixation in the filtration unit. Apart from the glass setup itself, also all supplies such as the ventilation, the cooling water, helium and the emptying syringe are installed.

2.6.3 Cleaning

The cleaning step consumes even more time than the measurement itself, but it is necessary for reliable, ultra-clean analysis in the μg carbon range with reproducible initial conditions. Although all glass parts have been cleaned before installation (see Sec. 2.6.7), this cleaning step in inert gas conditions with UPW and UV radiation is still required.

After flushing the vacuum line with UPH helium and zeroing the NDIR CO_2 detector, the glass setup is completely flushed with UHP helium to create the inert gas atmosphere. By monitoring the system pressure, this helium flush can also confirm the leak-free assembly of the glass setup. In the next step, the melting vessel is filled with 300 ml UPW which is subsequently rinsed to the photo-reactor. This 'cleaning sample' washes out contaminations from the quartz fibre filter and the glass surfaces. The

[20] Model 'Verpackungsdose PETG 1000 ml' by Semadeni
[21] Model 'Tissuquartz 2500 QAT-UP' by Pallflex

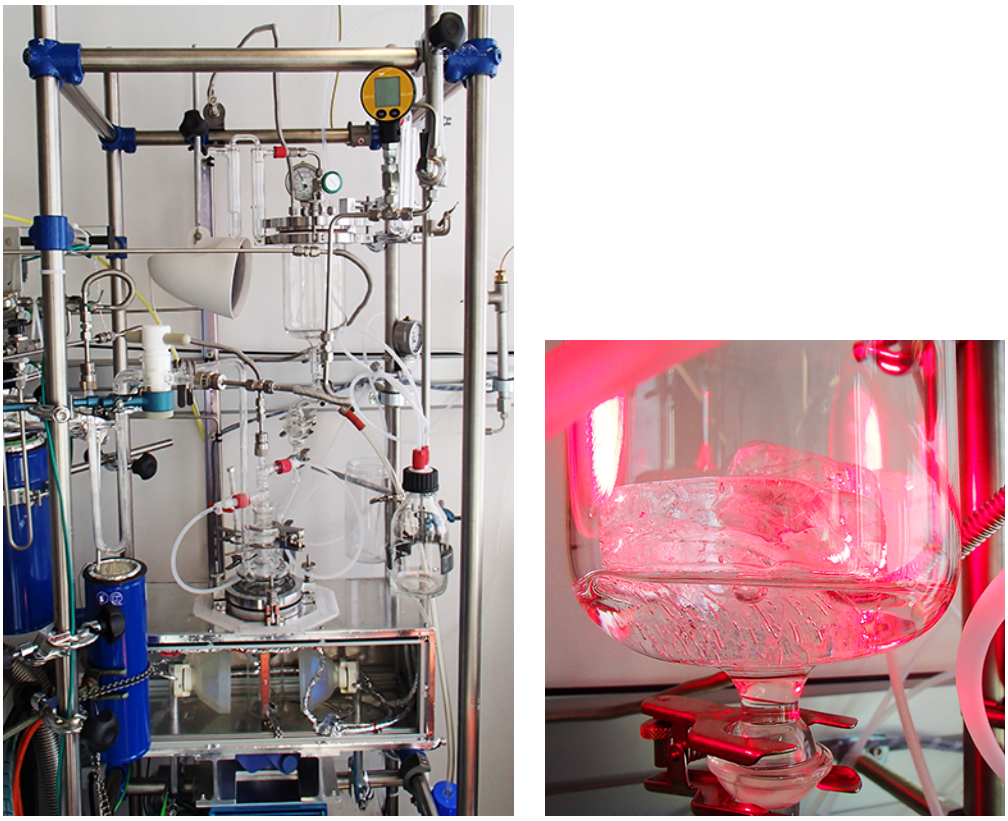

(a) **(b)**

Figure 2.6: Photographs of (a) the complete, assembled glass setup and (b) an ice sample in the melting vessel whilst IR irradiation for melting.

cleaning sample is acidified to pH 1.4 by adding 5 ml H_3PO_4 [22] with a glass syringe and a long stainless steel needle injected in parallel with the emptying syringe. The cleaning sample is degassed from IC and ambient air while the UV oxidation is started simultaneously to remove any oxidiseable contaminants. The carrier gas stream that degasses the sample is led through the NDIR CO_2 detector to monitor the cleaning process. Once the CO_2 concentration drops asymptotical below a set threshold to indicate the successful and finished cleaning, the UV lamps are turned off.

With the emptying syringe, the cleaning sample is removed from the photo-reactor, except for 50 ml. This residue is used later on to acidify the real sample. In this way, the acidification of the real sample can be done with a pre-oxidised and degassed solution of H_3PO_4 and UPW. The resulting solution then has a pH value below 2 and was prepared in an ultra-

[22] Analytical grade orthophosphoric acid 85%, 'EMSURE'

clean manner. Therefore, we use the cleaning sample twofold: to clean the glass setup and to provide an ultra-clean solution for acidification of the sample itself. All cleaning steps are performed in inert gas conditions at ambient pressure (flow-through mode) or with a light overpressure (closed mode).

2.6.4 Melting

During the oxidation of the cleaning sample in the photo-reactor, the melting of the real sample can be performed in the already cleaned melting vessel. Prior to processing, the ice sample is tempered at room temperature for 15 min to prevent cracking of the ice sample in the first rinsing step. In a laminar flow box, the ice sample is rinsed from all sides with UPW and placed into the melting vessel which is closed again with the cover plate. After flushing with UHP helium to create the inert gas atmosphere for sample processing, the ice sample is rinsed another time with UPW: for best results, the melting vessel is flooded with UPW until the ice sample floats and is drained to the waste via the 3-way valve at the bottom of the melting vessel. The two rinsing steps account for a sample mass loss of 25% – 30%. With the help of an IR lamp and a hot air gun, the cleaned sample is melted under a stream of UPH helium (see Fig. 2.6 b)).

2.6.5 Filtration and oxidation

Once the ice sample has completely molten, it is transferred to the cleaned photo-reactor by opening the 3-way valve and setting the melting vessel to overpressure. During the transfer, the liquid sample passes the filtration unit with the quartz fibre filter, where particulates including POC are separated from the sample (see Fig. 2.7 a)). In the photo-reactor, the filtrate mixes with the acidified residue from the cleaning sample.

The fill level is measured before and after the sample transfer to determine the sample volume for DOC concentration measurements (see Fig. 2.7 b)). The liquid, acidified sample is degassed from IC by bubble degassing with UHP helium delivered via the cooling finger. To monitor the degassing, the carrier gas stream is led through the NDIR CO_2 detector.

Once the degassing is finished, the CO_2 trap is activated by installing the liquid nitrogen cooling bath. The UV lamps are switched on to photo-oxidise the liquid sample (see Fig. 2.8). The carrier gas stream is led through the two water traps and the CO_2 trap where the DOC that has been photo-

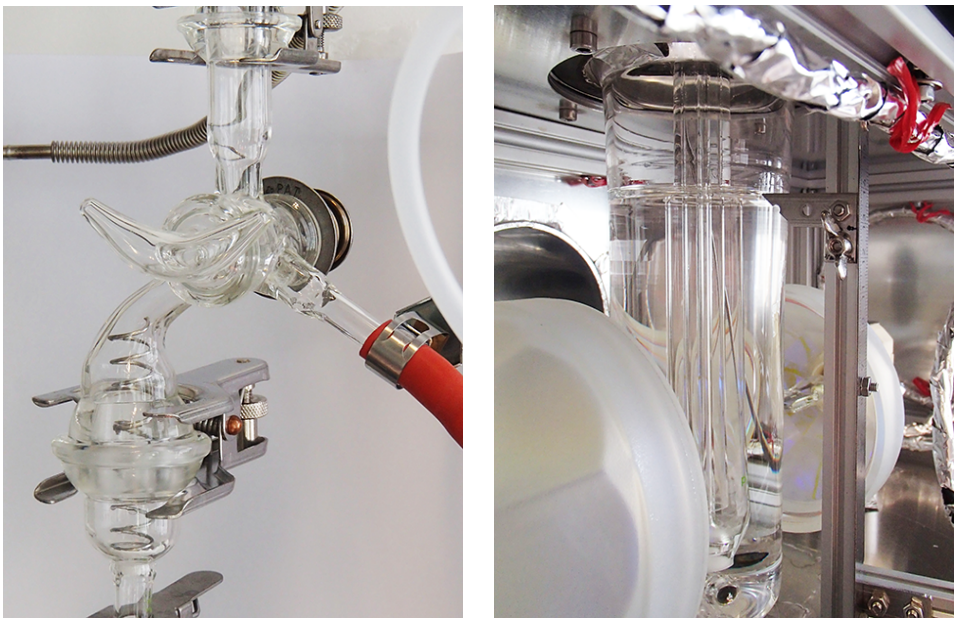

(a) (b)

Figure 2.7: Photographs of (a) the full-glass 3-way valve with the filtration unit beneath and (b) the photo-reactor with UV lamps and calliper.

oxidised to CO_2 is captured. After 45 min of oxidation, the UV lamps are switched off and the CO_2 trap is closed.

2.6.6 Sampling

The DOC has successfully been oxidised to CO_2 and is trapped in the CO_2 trap. In a first step, the helium is removed from the trap by exposure to the turbo-molecular pump while the cryogenic trap is still active. At the temperature of -196 °C, CO_2 stays solid even at pressures as low as 10^{-7} mbar. After the evacuation of helium and volatile species, the trap is closed and the cooling bath is removed to thaw the CO_2 sample.

The gaseous CO_2 sample is transferred to the cleaning tube by cryogenic pumping. Once frozen into the cleaning tube, residual volatile compounds (mainly helium) are removed from the sample by exposure to the turbo-molecular pump. In the next step, the CO_2 sample is transferred to the manometry cell, while water vapour is retained in the cleaning tube. For this, the CO_2 in the cleaning tube is thawed, a warmer cooling bath with a temperature of -72 °C is installed around the cleaning tube and a cooling bath with liquid nitrogen is installed around the glass tube of the manometry cell.

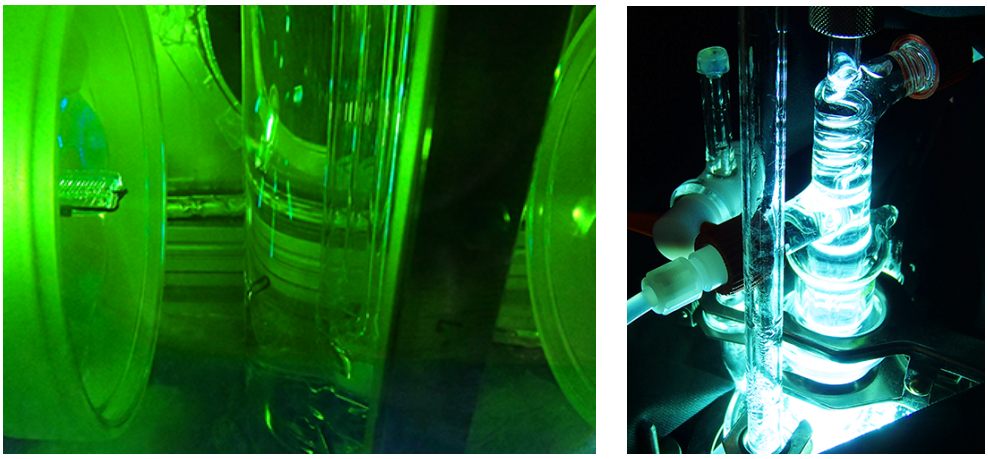

(a) (b)

Figure 2.8: Photographs during UV irradiation of (a) the photo-reactor, as seen through the welder's lens and (b) the reactor head with cooling finger, as seen inside the protective cloth.

After the transfer, the purified CO_2 sample is thawed in the manometry cell. The corresponding pressure of the expanded gas sample in the calibrated volume is read from the pressure transmitter and can be converted to the respective carbon mass.

For sampling for AMS analysis, the CO_2 sample is transferred to the sampling tube. With a gas torch, the lower 70 mm of the sampling tube are sealed off while the CO_2 sample is frozen to the bottom of the tube. The resulting glass ampoule contains the CO_2 sample and can be introduced to the GIS system of the MICADAS via the ampoule cracker for offline ^{14}C measurement. See Fig. 2.9 for a photograph of the complete vacuum line.

2.6.7 Next measurement

Before the next measurement, several final steps have to be performed. The quartz fibre filter that holds the POC of the ice sample is taken from the filtration unit. It is dried in a laminar flow box and stored in a freezer for analysis according to the PO^{14}C method.

Thanks to the emptying system, the glass setup can be reused for several samples without the time consuming disassembly and pre-cleaning of all individual glass parts. First, the analysed liquid sample is withdrawn from the photo-reactor with the emptying syringe. In parallel, the cryogenic water traps are reset: water trap 2 is thawed and evacuated to the turbo-

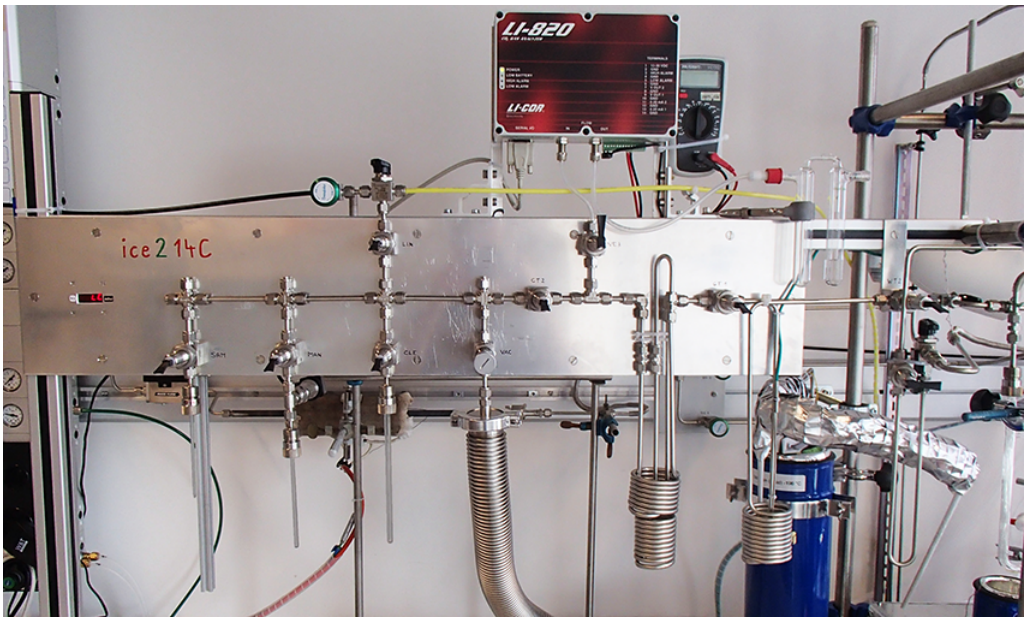

Figure 2.9: Photograph of the vacuum line for CO_2 sample preparation. The glass setup (see Fig. 2.6 a)) is connected to the right.

molecular pump, water trap 1 is replaced with a fresh glass U-tube that is filled at one leg with glass capillaries.

Especially the glass surfaces that have been in contact with the unfiltered and unoxidised sample need to be cleaned. Thus, the disassembled filtration unit is washed with UPW and the melting vessel is rinsed to both exits of the 3-way valve with UPW. Also the Z connector is rinsed to the photo-reactor with UPW.

Once a fresh quartz fibre filter for the next sample is inserted, the filtration unit is installed and the photo-reactor is emptied again. Finally, the extraction setup is ready for the next sample, restarting at the cleaning step (Sec. 2.6.3).

If the setup is not reused, all glass parts are disassembled and cleaned. The cooling finger and the emptying syringe are stored in a UPW bath, whereas all other glass parts and the steel spring are cleaned in several steps. First, the parts are kept overnight in a water bath with DECONEX, a laboratory cleaning agent. Next, the parts are first washed with deionised water, then with UPW. Finally, after drying in an oven at 50 °C, the parts are stored in a cupboard until the next assembly.

Chapter 3

Characterisation

To perform meaningful measurements, both a reliable operation procedure and an appropriate blank correction for the measurement itself have to be established. For this, we characterise the extraction setup in terms of the efficiencies, blank and timing of the individual steps. In this chapter, we present results from the characterisation of the CO_2 sample processing, the oxidation of DOC and of the procedural blank.

3.1 CO_2 sample processing

The CO_2 sample processing includes all steps from the formation of CO_2 at the photo-oxidation of DOC until the production of CO_2 sample vials for the ^{14}C measurement.

3.1.1 CO_2 sample transport

With first, basic tests we confirmed the proper function of the CO_2 sample transfer by cryogenic pumping. A cleaned, pure CO_2 sample was quantified in the manometry cell, expanded to the complete, evacuated vacuum line (SAM, MAN, CLE, LIN, CO_2 trap) and refrozen to the manometry cell where it was isolated and thawed to measure the recovery. In dependence of the refreezing time t_{freeze}, we found a recovery of 100% for $t_{\text{freeze}} \geq 60\,\text{s}$.

Next, the recovery of CO_2 from the CO_2 trap was measured for the same conditions, but over a range of sample masses and with fixed $t_{\text{freeze}} = 2\,\text{min}$. Within the uncertainty of the pressure transmitter we found a recovery of 100% for the full range of sample masses from $0.5\,\mu\text{g}$ C to $650\,\mu\text{g}$ C.

However, in the real measurement, the CO_2 sample transport is not done in high-vacuum conditions but with residual helium from the carrier

gas. Therefore, we repeated the CO_2 trap recovery experiment with the same procedure and conditions as in the real measurement. The CO_2 trap contained the frozen CO_2 sample and was filled with helium. First, the helium was removed by evacuation of the active trap to the turbo-molecular pump until the pressure at the pump was below 10^{-6} mbar. Next, the CO_2 trap was thawed and the sample was transferred to the manometry cell to determine the recovery.

Since not all helium is removed in the first step, the residual helium hampers the transfer of CO_2 in the vacuum line by decreasing its mean free path. Therefore, the freezing time for full recovery is longer. We re-determined the freezing time for the conditions of a real measurement and found a full recovery of CO_2 from the CO_2 trap for $t_{\text{freeze}} \geq 270\,\text{s}$.

Thus for the real measurement, we use $t_{\text{freeze}} = 5\,\text{min}$ for the transfer of the CO_2 sample to the cleaning tube. Once residual helium and water are removed in the cleaning step, a freezing time of $t_{\text{freeze}} = 2\,\text{min}$ can be used for the cryogenic pumping sample transfers thanks to the high-vacuum conditions.

3.1.2 CO_2 trapping

The CO_2 trap is built from a 4 mm inner diameter stainless steel tube that is bent to a coil and can be immersed in a cooling bath (see Sec. 2.4). To validate its proper function and to quantify its capacity, we performed the following experiments.

First, we tested the capability of the CO_2 trap to capture an impulse of CO_2 from the helium carrier gas stream. For this, a large CO_2 sample was transferred and frozen to water trap 2. A helium carrier gas stream with a flow-rate of 100 nccm, passing through water trap 2 and the CO_2 trap was established. Its CO_2 concentration was monitored downstream of the traps with a mass spectrometer[1] that was connected to vent 3. Once the CO_2 trap was activated (immersed in liquid nitrogen), the CO_2 sample was released by thawing water trap 2 and thus transported to the CO_2 trap with the carrier gas stream.

For the initial setup of the CO_2 trap, which consisted of a 2 m long stainless steel tube, an increase in the CO_2 signal after the release of the CO_2 sample from water trap 2 was observed for this experiment. Due to this trap loss, we reconstructed the CO_2 trap by extending its overall length to 4 m. In the new, improved version no more trap loss was detected for this

[1] Atmospheric pressure gas analysis system 'Cirrus 2' from MKS Instruments

experiment. This confirmed the function of the CO_2 trap to fully capture an impulse of CO_2 with a corresponding carbon mass of several mg at a carrier gas flow-rate of 100 nccm.

Apart from the incomplete capture of a CO_2 impulse, another mechanism that can induce CO_2 loss from the CO_2 trap is leaking. Although the CO_2 trap may succeed to freeze out CO_2 from the carrier gas, the constant input of fresh, warm gas into the trap can induce a transport of already trapped CO_2 along the CO_2 trap. This relocation of CO_2 by repeated thawing and refreezing can result in the loss of CO_2 from the CO_2 trap and depends both on the total amount of carrier gas that passes the trap as well as on the flow-rate of the carrier gas.

To monitor and quantify this effect, we loaded the CO_2 trap with a CO_2 sample of 350 μg C and activated the trap. A helium carrier gas stream was established through the trap and the concentration was monitored downstream with a mass spectrometer connected to vent 3. At a flow-rate of 200 nccm, we observed a steady increase of the CO_2 concentration in the gas stream after 20 min, corresponding to a CO_2 loss from the trap. However, with a lower flow-rate of 100 nccm, no CO_2 loss was detectable for at least 130 min (measurement stopped after 130 min). This confirmed that for the conditions of the real measurement ($\leq$ 50 min trap operation at 100 nccm carrier gas flow), the CO_2 trap does not show detectable leaking.

To quantify the total recovery of CO_2 in the CO_2 trap, we performed a third experiment. Similar to the first test, a CO_2 sample was released from water trap 2 and captured in the CO_2 trap. The initial and the recovered CO_2 sample were quantified by pressure measurement in the manometry cell. The carrier gas flow-rate was 100 nccm and the captured sample was processed for quantification as described in Sec. 3.1.1 . For a set of ten CO_2 samples ranging from 40 μg C to 600 μg C, we found a recovery of $(99.0 \pm 0.6)\%$.

Additionally, two blank measurements were performed. We repeated the same experiment without a CO_2 sample in water trap 2 and could not detect any CO_2 in the CO_2 trap. This confirmed the clean operation of the CO_2 trapping and the validity of the measured recovery.

3.1.3 Recovery of CO_2 from the liquid sample

Once DOC is oxidised to CO_2 in the photo-reactor, the generated CO_2 is extracted from the liquid solution by bubble degassing with helium. Then, the CO_2 is separated from the helium gas stream in the CO_2 trap, is purified in the cleaning tube and is quantified in the manometry cell. To charac-

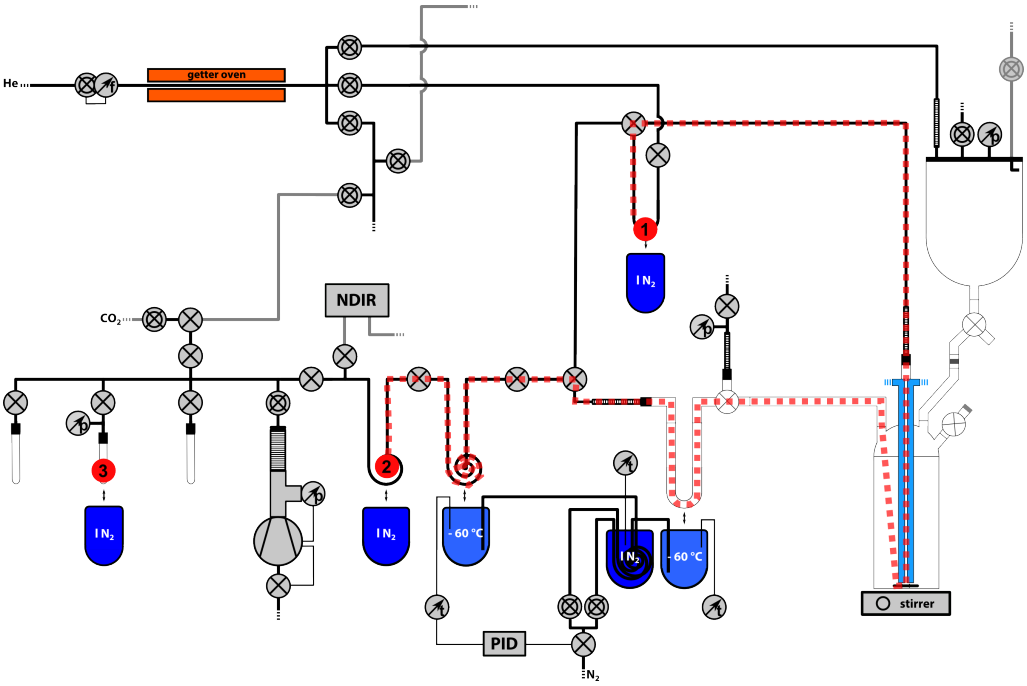

Figure 3.1: Experimental setup to determine the recovery of CO_2 from the liquid sample. '1': the U-tube is loaded with a known CO_2 sample, '2': the CO_2 is transferred through the setup with the helium carrier gas stream (red, dashed line) and captured in the CO_2 trap. '3': the recovered mass is determined in the manometry cell. The detailed and complete setup is shown in Fig. 2.1.

terise this complete CO_2 sample treatment, we performed another recovery experiment as shown in Fig. 3.1.

The setup was completely assembled for normal operation, the photo-reactor was filled with 300 ml UPW, acidified to pH 1.5, degassed and cleaned with UV irradiation. In a first step, the the vacuum line including the U-tube was filled with CO_2 to a known pressure p_0. Next, the U-tube was isolated and the CO_2 sample was frozen to the U-tube while the rest of the vacuum line was evacuated. A helium carrier gas stream of 100 nccm was established through the getter oven, the U-tube with the frozen CO_2 sample, the photo-reactor with UPW sample, the active water traps, the active CO_2 trap and vent 3. Then, the cryogenic bath was removed from the U-tube and the CO_2 sample was released and transported with the carrier gas stream, as shown by the red, dashed line in Fig. 3.1. The CO_2 sample was flushed through the water-filled photo-reactor and separated from the carrier gas stream in the CO_2 trap. According to the envisaged operation, the CO_2 trap was operated for 45 min, then the carrier gas stream was stopped. As for real measurements, the CO_2 sample was cleaned from helium and

water vapour in the cleaning tube and finally transferred to the manometry cell for quantification. The measured pressure p_1 was compared to the expected pressure $p_{\mathrm{exp}} = p_0\, V_{\mathrm{U-tube}}/V_{\mathrm{MAN}}$ from the initial CO_2 sample.

With this setup, we analysed four samples of medium size (30 – 95 μg C) and found an average recovery of (98 ± 2)%. Despite the lower sample number, this compares well with the CO_2 trap recovery determined in Sec. 3.1.2 . This high recovery shows that the CO_2 sample processing is very efficient and comprises almost no mass loss. However, with this experimental layout it is not possible to mimic the degassing of CO_2 according to the real measurement. Still, in view of the high recovery and the general confirmation of the degassing time constants by monitoring with the NDIR CO_2 detector, the settings for the CO_2 sample processing are suitable.

Apart from ^{14}C measurements (see Sec. 3.3.1) we also performed blank recovery measurements to exclude input of extraneous CO_2. We used the same procedure as before, however no CO_2 sample was loaded to the U-tube. All three blank measurements confirmed the clean operation as no CO_2 could be detected within the detection limit of 0.6 μg C.

Additionally, this first experiment of the complete CO_2 sample treatment also demonstrated the proper function of both water traps. Whereas water trap 1 captured several ml of water during the operation, typically only few μg of water vapour were separated from the sample in the last cleaning step before CO_2 quantification.

3.1.4 Quantification of CO_2 and sample concentration

The carbon mass of the oxidised DOC is determined by the pressure measurement of the CO_2 sample in the manometry cell. We approximate CO_2 as an ideal gas and derive the carbon mass m_{C} from the pressure $p_{\mathrm{CO_2}}$ of the CO_2 sample:

$$m_{\mathrm{C}} = \frac{p_{\mathrm{CO_2}}\, V_{\mathrm{MAN}}\, \mathrm{M_C}}{\mathrm{R}\, T_{\mathrm{CO_2}}}$$

where V_{MAN} is the calibrated volume of the manometry cell, $\mathrm{M_C}$ is the molar mass of carbon, R is the universal gas constant and $T_{\mathrm{CO_2}}$ the temperature of the gas sample. We confirmed that this approximation is valid at these conditions (room temperature and low pressure) by a comparison with the more accurate Van-der-Waals equation. Although this equation also accounts for inelastic collisions between molecules and the volume of the molecules [Demtröder, 2012], the calculated mass differed from the mass derived with the ideal gas law only in the per mill range. In view of the overall uncertainties this is negligible and thus the ideal gas law can be used

to calculate the carbon mass of the CO_2 sample from the manometry cell pressure.

The range of CO_2 sample masses that can be measured in the manometry cell is determined by its volume and by the pressure range of the used pressure transmitter. The volume of the manometry cell has been calibrated and is (3.57 ± 0.08) ml. The pressure transmitter measures absolute pressure from 0 to 400 mbar with an uncertainty of 0.04 mbar (for both, see App. C.2). In terms of carbon mass, this translates to measurable samples of up to 695 μg C with a resolution of 0.04 μg C. The respective uncertainty is determined for each measurement by error propagation and is around 3% for typical sample sizes.

To derive the DOC concentration of the ice sample, we measure also the mass of the liquid sample. As detailed in App. C.1, the sample mass is determined from the fill level height in the photo-reactor. Thus, the DOC concentration can be calculated as $[\mathrm{DOC}] = m_\mathrm{C}/m_\mathrm{sample}$.

To estimate the minimal DOC concentration of an ice sample that is measurable with the current setup, we make the following considerations. Taking into account the maximum photo-reactor volume of 350 ml and the cleaning residue of 50 ml for acidification, the sample mass is limited to 300 ml. In principle, the lowest measurable carbon mass would be 0.6 μg C, however for a meaningful measurement we have to consider the procedural blank mass (see Sec. 3.3.3). Considering a minimal sample mass of three times the method blank mass (3.5 μg C) as a benchmark for a reliable measurement, the minimal DOC concentration for ice samples is currently limited to 33 μg C/kg ice.

3.2 Oxidation of dissolved organic carbon

The wet photo-oxidation of DOC to CO_2 is the central process of the complete extraction. Apart from the high fraction of unknown organic compounds in alpine glacier ice, the multitude of possible oxidation pathways for the numerous organic compounds makes a theoretical prediction impractical. Rather, we quantified the oxidation process by monitoring the CO_2 production over time and by measuring the recovery of DOC for several standard substances. Although we are interested in the bulk DOC for the ^{14}C analyses, the analysis of selected single organic standards gives a comprehensive picture for the understanding of the oxidation process in our extraction setup.

3.2.1 Production of dissolved organic carbon standards

We selected four different organic compounds for the production of standard substances. According to Legrand et al. [2013b], the major known constituents of DOC in alpine glacier ice are monocarboxylic acids, humic like substances and dicarboxylic acids. Except from a standard for humic like substances, we chose formic, acetic and oxalic acid as standards to represent both mono- and dicarboxylic acids. Oxalic acid furthermore is available as an isotopic standard with known, yet different ^{14}C content and used for the blank measurements (see Sec. 3.3.2). For a comparison with other existing systems and DOC analysers, we also included potassium hydrogen phtalate (PHP), a commonly used DOC standard.

We produced the standards in the desired concentration by ourselves to provide ultra-clean conditions. First, UPW was acidified, photo-oxidised and degassed in inert gas conditions in the photo-reactor. Pre-cleaned 50 ml glass vials were filled with 0.5 – 1 g of the respective chemical, filled with argon as inert gas and closed with a septum. Next, 30 – 50 ml of the cleaned UPW was withdrawn from the photo-reactor with a long stainless steel needle and a glass syringe via the septum of the emptying system. It was added to the glass vial which we sonicated for dissolution. This first standard with concentrations of around 10000 – 20000 ppm was dissolved further in a second vial in the same procedure with another 30 – 50 ml of the cleaned UPW. The final standards had concentrations of around 200 – 300 ppm, what results in typical DOC masses on the order of magnitude of 10 to several 100 μg C when using 0.2 – 5 ml of standard.

We checked the concentration of the produced standards by analysis with ion chromatography. For oxalate, the prepared concentrations were confirmed, yet the measurements revealed that the used chemical for all three isotopic standards was not pure oxalic acid but oxalic acid dihydrate. Formate and acetate could not be measured reliably due to interference with the acidified matrix. For phtalate no suitable column was available. Tab. 3.1 summarizes the used standards and the prepared concentrations.

In retrospect, although the production of the ultra-clean standards was successful, we recommend a less elaborate production method for future applications. At the time of production, it was unclear whether the DOC content of UPW is low enough to produce clean standards, therefore it was pre-oxidised. However, for the high concentrations of the standards normal UPW can be used directly for the standard production under inert gas conditions.

standard	**chemical used for preparation**	**[DOC] (mg C/kg)**
oxalic acid ($C_2H_2O_4$)	oxalic acid dihydrate, fossil	45
oxalic acid ($C_2H_2O_4$)	oxalic acid dihydrate, half-modern IAEA-C7, $F^{14}C = 0.4953$	51
oxalic acid ($C_2H_2O_4$)	oxalic acid dihydrate, modern NIST 4990C, $F^{14}C = 1.34033$	41
acetic acid ($C_2H_4O_2$)	sodium acetate	74
formic acid (CH_2O_2)	sodium formate	46
phthalic acid ($C_8H_6O_4$)	PHP	140

Table 3.1: Overview of the used standards. The chemical used for preparation is given along with the respective DOC concentration [DOC] in mg C/kg. All standards were prepared with pre-oxidised UPW and in inert gas conditions.

3.2.2 Oxidation process

To monitor the oxidation process and its duration in real-time, we observed the CO_2 which is produced at the oxidation with the NDIR CO_2 detector. For this, we ran the extraction setup in normal operation mode with the photo-reactor filled with 300 ml acidified, oxidised and degassed UPW. However, during sample oxidation, the CO_2 trap was inactive and thus the CO_2 concentration of the carrier gas stream could be monitored with the NDIR detector at vent 3. Few ml of a liquid standard were injected into the photo-reactor via the septum of the emptying system and the UV irradiation was started. The resulting CO_2 signal over time is characteristic for each substance as it depends on the respective molecular bonds that have to be dissociated to oxidise the organic molecule to CO_2.

Fig. 3.2 shows the CO_2 concentration in the carrier gas stream as recorded with the NDIR CO_2 detector versus the oxidation time for the four used standards oxalic acid (OXA, fossil), acetic acid (ACE), formic acid (FOR), and phthalic acid (PHP). The oxidation peaks are normalized to a sample size of 100 μg C (i.e. the area is identical for all shown peaks) to allow the comparison of the individual line shapes.

Oxalic acid and formic acid are oxidised rapidly, resulting in high and sharp peaks of the CO_2 signal. The broad peak of acetic acid represents

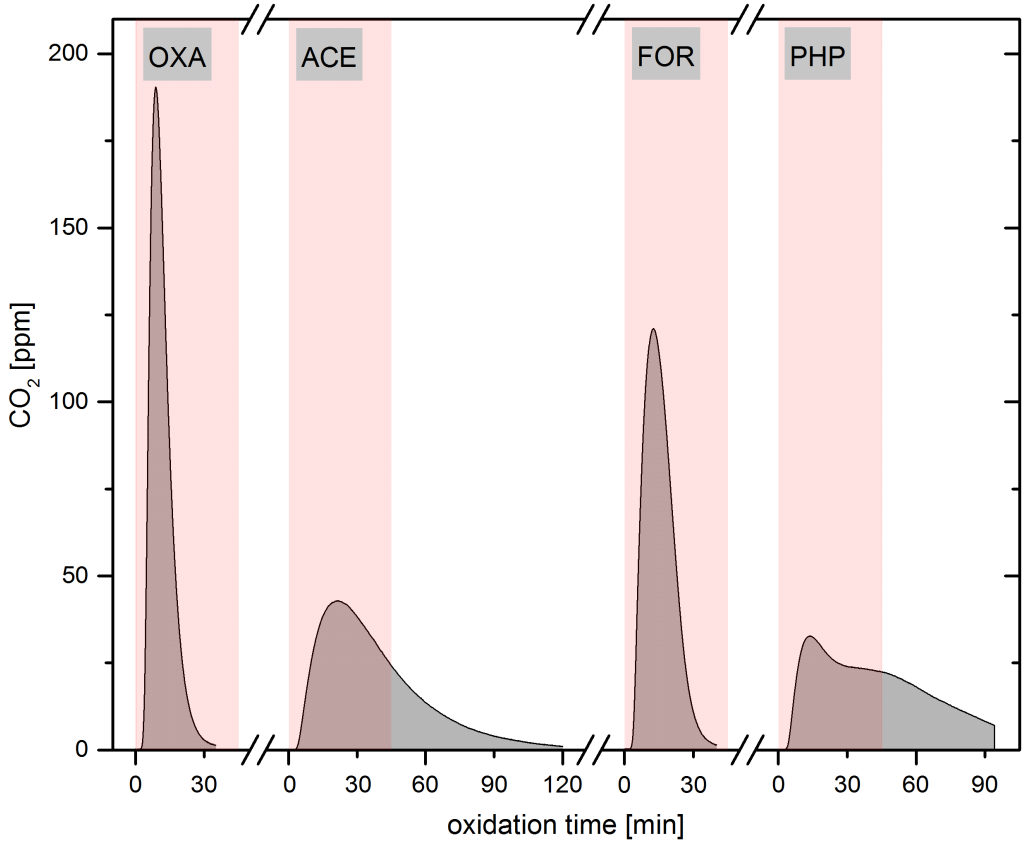

Figure 3.2: Oxidation peaks for different standards, normalized to 100 μg C sample mass. The recorded CO_2 signal is shown versus the oxidation time for the four standards oxalic acid (OXA), acetic acid (ACE), formic acid (FOR) and phthalic acid (PHP). Indicated in red is a time window of 45 min that corresponds to the normal oxidation time.

a slow, energy intensive oxidation. Phthalic acid also features a broad, flat CO_2 signal, however the double peak suggest the superposition of two oxidation processes. The cut-off in the tail of the PHP CO_2 signal is due to stopping of the experiment and is corrected for in related calculations.

Indicated as red shaded regions in Fig. 3.2 are 45 min time frames that correspond to the oxidation and trapping time in normal operation mode. As clearly seen, oxalic acid and formic acid are completely oxidised within this time frame and thus recovered to 100% (without accounting for the oxidation efficiency). Due to the slower oxidation, acetic acid and phthalic acid are only recovered to 70% and 55%, respectively.

Nevertheless, we decided to use an oxidation time of 45 min for normal operation, since two of the three standards that are relevant for DOC from alpine ice are fully oxidised in this time while the third standard still is

oxidised to 70%. Apart from a reduced analysis time, keeping the oxidation time as short as necessary also reduces contamination by a possible background input. Furthermore, as tested in a single, preliminary experiment with a real glacier ice sample, 90% of the oxidisable DOC was oxidised within the first 45 min. However, in future studies, a possible fractionation effect resulting from preferential oxidation of certain compounds should be addressed according to Beaupré and Druffel [2012].

3.2.3 Oxidation efficiency

The efficiency of the oxidation process is given as the ratio of the injected carbon mass to the carbon mass of the measured CO_2. We derive it from the NDIR measurements of the previous experiment (Sec. 3.2.2). The injected carbon mass is calculated from the mass of the injected standard with known carbon concentration (Tab. 3.1). The carbon mass of the detected CO_2 is derived from the recorded signal of the NDIR CO_2 detector. As described in App. C.3, the NDIR CO_2 detector has been calibrated to use it for the quantitative measurement of CO_2 by integration of the CO_2 signal at a carrier gas flow-rate of 100 nccm. Furthermore, the detected mass is blank corrected (see Sec. 3.3.2).

Tab. 3.2 summarises the results for the four measured standards. Acetic acid, formic acid and phthalic acid were only measured once, the corresponding CO_2 signal is shown in Fig. 3.2. To estimate the uncertainty of the measurements, the oxalic acid standard was measured 5 times with varying sample size. The oxidation efficiency is given in three ways. The oxidation efficiency for a complete oxidation represents the general capability of the setup to oxidise a certain compound. The oxidation efficiency for an oxidation over 45 min represents the capability of the setup to oxidise a certain compound within 45 min – the used oxidation time for normal operation. Finally, for a comparison with other systems, the oxidation efficiency for complete oxidation is given normalized to the efficiency of the commonly used TOC standard PHP.

Oxalic acid showed a good absolute oxidation efficiency of (85 ± 7)% (mean ± standard deviation of 5 measurements). Since oxalic acid was fully oxidised within 45 min, the oxidation efficiency is the same for both considered scenarios. Further measurements of different oxalic acid isotopic standards (see Sec. 3.3.2) confirmed the determined oxidation efficiency within the uncertainties even though the recovered carbon mass was determined directly in the manometry cell and not by the indirect NDIR measurement.

standard	sample size (μg C)	oxidation efficiency (%) for complete oxidation	oxidation efficiency (%) within 45 min	oxidation efficiency (%) relative to PHP
oxalic acid (modern)	16 – 121	85 ± 7	85 ± 7	86
acetic acid	163	93	66	95
formic acid	102	111	111	114
phthalic acid	165	98	56	100

Table 3.2: Oxidation efficiencies for the different standards. Sample size is given in the corresponding carbon mass, the oxidation efficiency is given in absolute numbers for a complete oxidation and a 45 min long oxidation. For comparison, the efficiency for complete oxidation is given relative to the efficiency of a complete oxidation of phthalic acid. The efficiency for oxalic acid was determined by five measurements, thus the standard deviation is given as uncertainty.

For acetic acid we found similar good oxidation efficiency for a complete oxidation. However, since the full oxidation took longer, the recovery from a 45 min long oxidation is reduced to 66%.

Formic acid was recovered nominally to 111%, this has to be interpreted with regard to the uncertainties. As shown with the oxalic acid standard, large uncertainties have to be expected. Apart from the mass measurements itself, also the complete sample preparation of the standards as well as the oxidation experiment introduce uncertainties. Therefore, we estimate that formic acid is oxidised and recovered completely.

Since both of the more volatile standards showed such high recoveries, we assume that our setup does presumably not suffer a loss of volatile species in the acidification and degassing steps prior to the oxidation.

Phthalic acid was also completely oxidised given the oxidation is long enough. For a 45 min long oxidation phthalic acid was recovered only to 56%.

Normalised to phthalic acid, the efficiencies of the complete oxidation are high throughout. A study by Preunkert et al. [2011] that used a low-pressure UV lamp for photo-oxidation found normalised oxidation efficiencies for oxalic acid, acetic acid and formic acid of (102 ± 6)%, (114 ± 11)% and (112 ± 10)%, respectively. Compared to our setup, oxalic acid and acetic acid show higher oxidation efficiencies, however our results should only be seen as a first estimation.

3.3 Method blank

To know the procedural blank (i.e., the background value) of a measurement is essential to assess the performance of the method and to be able to correct for this inherent contamination effect. Therefore, in addition to the blank mass being as low as possible, both the blank mass and blank ^{14}C content need to be stable over time for a meaningful correction, in particular for small samples. To track the different contributions to the overall procedural blank, we performed a step-wise blank characterisation.

3.3.1 CO_2 sample processing blank

To check for possible leaks or fractionation effects during CO_2 extraction and sampling after the oxidation process, we repeated the experiment from Sec. 3.1.3 and additionally measured the ^{14}C content of the CO_2 sample. In short, gaseous, fossil CO_2 from a CO_2 cylinder was introduced via the U-tube to the extraction setup at normal operation conditions with a pre-cleaned water sample. The CO_2 sample was recovered in the CO_2 trap, quantified in the manometry cell and sampled to glass vials for ^{14}C analysis with the GIS and MICADAS in Bern. As a reference, we also directly measured the ^{14}C content of the CO_2 from the cylinder by sampling it with a gas mouse.

The untreated reference sample was graphitised for the AMS measurement and has a ^{14}C content of $F^{14}C_{\text{ref}} = 0.0024 \pm 0.0003$ corresponding to fossil CO_2. Four samples with masses ranging from 30 μg C to 96 μg C were treated as described above and measured directly as gaseous samples via the GIS at the MICADAS. Their average ^{14}C content is $F^{14}C_{\text{sampling}} = 0.003 \pm 0.001$, the indicated uncertainty corresponds to the standard deviation of the four samples. All measurement results are shown in App. E (samples 'cal03' – 'cal07').

Within the uncertainty, no increase of the ^{14}C content due to the handling of the gaseous CO_2 sample could be detected. As already shown by the blank measurements in Sec. 3.1.3, this underlines the clean and leak-free operation of the CO_2 sample handling from the extraction up to the sampling.

3.3.2 Oxidation blank

The photo-oxidation step oxidises the DOC of the liquid sample to CO_2. But also contaminants that enter the photo-reactor with the liquid sample

or that have not been fully removed beforehand, can be oxidised together with the sample itself and thus falsify the CO_2 sample mass and ^{14}C content. To correct for such a bias, we determined the blank mass m_{blank} and blank ^{14}C content $F^{14}C_{\mathrm{blank}}$ in Sec. 3.3.3. However, in a first step, we estimated the blank contribution of the oxidation step itself (m_{oxi} and $F^{14}C_{\mathrm{oxi}}$), without accounting for contaminations from the previous sample preparation steps. As shown in Sec. 3.3.1, no background contribution arises from the subsequent processing of the CO_2 sample. Therefore, to quantify the oxidation blank, we performed the following experiments.

We operated the extraction setup in normal operation mode starting from the photo-reactor which was filled with 300 ml acidified and degassed UPW. This 'blank sample' was oxidised until it was free of DOC as confirmed by the CO_2 signal that we monitored at the NDIR CO_2 detector. Next, we added one of the three ultra-pure oxalic acid isotopic standards (see Sec. 3.2.1) by means of a glass syringe with a long stainless-steel needle via the septum and the valve of the emptying system. After the degassing of this 'standard sample', we activated the CO_2 trap and started the UV irradiation for 45 min. After oxidation, the CO_2 sample was cleaned, quantified and sampled to glass vials for the subsequent ^{14}C measurement with the MICADAS and GIS.

In this way, we performed eight successful measurements with isotopic standards of different ^{14}C content and mass ($F^{14}C = 0$, $F^{14}C = 0.4953$ and $F^{14}C = 1.34033$ with masses of 10 – 27 μg C), the measurement results are shown in App. E (samples 'cal10', 'cal11', 'cal12', 'cal15', 'cal16', 'cal17', 'cal18' and 'cal19'; 'cal09' and 'cal14' were identified as potential outliers and thus are not used for the analysis).

To calculate the oxidation blank, we considered the isotopic mass balance equation:

$$m_{\mathrm{tot}}\, F^{14}C_{\mathrm{tot}} \;=\; m_{\mathrm{sta}}\, F^{14}C_{\mathrm{sta}} \;+\; m_{\mathrm{oxi}}\, F^{14}C_{\mathrm{oxi}} \tag{3.1}$$

where m_{tot} and $F^{14}C_{\mathrm{tot}}$ are the measured total mass and total ^{14}C content of the sample. $F^{14}C_{\mathrm{sta}}$ is the ^{14}C content of the added standard and thus known by default. Although m_{sta} is known from the mass of added standard, this is not accurate enough as it was only measured indirectly via the mass of the filled syringe and the respective concentration of the standard. m_{tot} was measured more precisely in the manometry cell and thus we use $m_{\mathrm{sta}} = m_{\mathrm{tot}} - m_{\mathrm{oxi}}$, as derived from common mass balance.

Furthermore, for the fossil standards, $F^{14}C_{\mathrm{sta}} = 0$, thus Eq. 3.1 simplifies to: $m_{\mathrm{tot}}\, F^{14}C_{\mathrm{tot}} \;=\; m_{\mathrm{oxi}}\, F^{14}C_{\mathrm{oxi}}$.

With this theoretical basis and the results of the eight standard measurements, we calculated m_{oxi} and $F^{14}\mathrm{C}_{\mathrm{oxi}}$ in an iterative optimisation approach: Starting from a randomly chosen range for $F^{14}\mathrm{C}_{\mathrm{oxi}}$, the results of the fossil and modern ($F^{14}\mathrm{C} = 1.34033$) standard were first used to confine the possible range of m_{oxi}. Then, the results of the half-modern ($F^{14}\mathrm{C} = 0.4953$) standard were used to further restrict the initially chosen range of $F^{14}\mathrm{C}_{\mathrm{oxi}}$. These steps were performed iteratively until the values stopped converging. We included the uncertainties of the individual measurements in this process by calculating a possible range for each parameter. Thus the resulting values for the blank can be given with the associated uncertainties:

$$m_{\mathrm{oxi}} = (2.0 \pm 0.5)\,\mu\mathrm{g\,C} \quad \text{and} \quad F^{14}\mathrm{C}_{\mathrm{oxi}} = 0.57 \pm 0.11$$

We can correct for the measurement bias that is induced by the oxidation step by applying Eq. 3.1 with the values found for the oxidation blank. As shown in Fig. 3.3, this correction strongly improves the quality of the measurement. The measured $F^{14}\mathrm{C}$ of the isotopic standards is displayed as red data-points. Their nominal $^{14}\mathrm{C}$ content is known and indicated by the blue horizontal lines ($F^{14}\mathrm{C} = 0$, $F^{14}\mathrm{C} = 0.4953$ and $F^{14}\mathrm{C} = 1.34033$). Blue data-points represent the same measurements, but have been corrected for the oxidation blank. Open circles refer to the measurements that we used to calculate the oxidation blank, filled circles are further independent measurements.

For sample masses below $20\,\mu$g C, the oxidation blank correction shifts all standard measurements to the expected $^{14}\mathrm{C}$ content of the respective standard. In particular for small sample masses, the measurement uncertainty is increased due to the comparatively strong correction. Also for bigger sample masses, the blank correction works in principle, however does not completely correct for biases. Furthermore, when comparing the measurements that were used to calculate the oxidation blank (open circles) and independent measurements (filled circles), it can be seen that the blank correction is not self-optimised to the used data-points but works for arbitrary measurements.

Although the used standards were prepared in an ultra-clean manner (see Sec. 3.2.1), they could in principle also contain a contamination and thus wrongly contribute to the oxidation blank which should only account for sources that are related to the oxidation step itself.

To test this, we performed another set of measurements with the same experiment as described above. We measured four standard samples of the fossil oxalic acid standard over a wide mass range from $9\,\mu$g C to $105\,\mu$g C

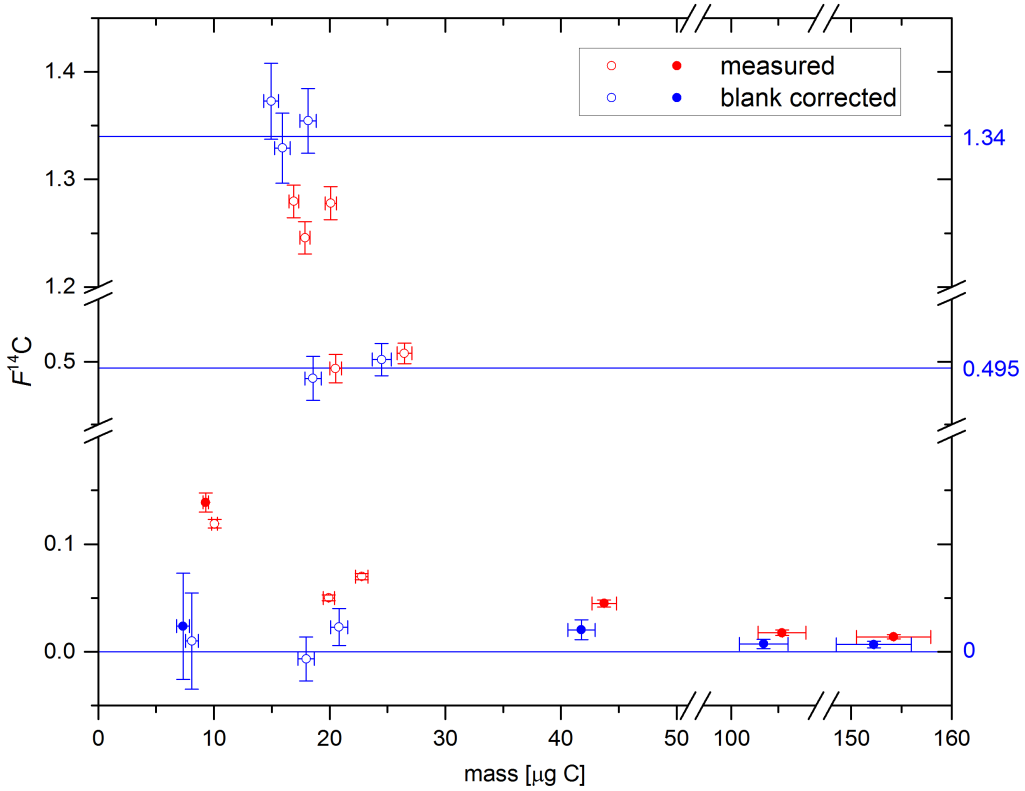

Figure 3.3: $F^{14}C$ of measured isotopic standards with known ^{14}C content (horizontal blue lines: $F^{14}C = 0$, $F^{14}C = 0.4953$ and $F^{14}C = 1.34033$). Red data-points show the measurement results, blue data-points are corrected for the oxidation blank (m_{oxi} and $F^{14}C_{oxi}$). Open circles refer to the measurements that were used to calculate the oxidation blank, filled circles are further independent measurements.

(results shown in App. E, samples 'cal21' – 'cal25', and in Fig. 3.3 as filled circles).

We formulated the isotopic mass balance equation (Eq. 3.1) for different contamination scenarios:

1. constant blank: $m_{tot}\,F^{14}C_{tot} = m_{sta}\,F^{14}C_{sta} + m_{oxi}\,F^{14}C_{oxi}$
2. mass dependent blank: $m_{tot}\,F^{14}C_{tot} = m_{sta}\,F^{14}C_{sta} + \alpha\,m_{sta}\,F^{14}C_{oxi}$
3. mixed blank: $m_{tot}\,F^{14}C_{tot} = m_{sta}\,F^{14}C_{sta} + (m_{oxi} + \alpha\,m_{sta})\,F^{14}C_{oxi}$

Here, α is a dimensionless factor ($0 \leq \alpha \leq 1$), that relates the mass of the blank with the mass of the added standard. We fitted our measurement results to the different models to derive the most probable contamination scenario. From this, we could exclude the purely mass dependent blank model (case 2) and found only a small contribution of a mass dependent

blank input ($\alpha = 0.005$) for the mixed blank model (case 3). Thus, the assumption of a constant oxidation blank with m_{oxi} is well grounded in a first order approximation and in spite of the relatively large uncertainties and small number of available measurements.

In any case, m_{oxi} can be seen as an upper limit of the oxidation blank mass since we could not disentangle the 'pure' oxidation blank from contaminations that arise from the injection of the standards to the photo-reactor.

The determined oxidation blank is only valid for the described (standard) experimental settings. In particular the oxidation time has an influence on the oxidation blank and thus the reported values can only be used for an UV irradiation of 45 min. A preliminary experiment indicated that in a first order approximation, the oxidation blank mass is direct proportional to the oxidation time, further experiments are needed for a rigorous investigation. This also emphasises the need to keep the oxidation time as short as possible for a low procedural blank mass, while on the same hand it needs to be long enough to guarantee a high and representative DOC yield.

3.3.3 Overall dissolved organic carbon blank

To determine the overall method blank (m_{blank} and $F^{14}\mathrm{C}_{\mathrm{blank}}$), we need to consider the complete extraction process of DOC from an ice sample to the CO_2 sample. This includes not only the CO_2 sample processing (Sec. 3.3.1) and the oxidation (Sec. 3.3.2), but also the ice sample preparation, melting and filtration steps. However, we can not simply extend and pursue the method used in Sec. 3.3.2. Whereas the standards used for the oxidation blank were liquid (and were prepared by the dissolution and dilution of known, pure chemicals), frozen standards are needed to characterise the complete process. Apart from being ultra-pure, the frozen standards additionally need to be homogeneously mixed. Due to the complexity of ice nucleation dynamics and the requirements for a clean and reproducible production of frozen standards, we decided to determine the overall method blank without the use of standards.

In a first, unsuccessful approach, we tried to disentangle the different blank contributions by measuring liquid and frozen aliquots of UPW and tap water samples (App. E , samples 'cal27', 'cal30', 'cal32', 'cal33', 'cal34'). All sample processing steps were performed according to the standard procedures (see Sec. 2.6) for a frozen ice sample. However, for the liquid aliquots we skipped the ice preparation, melting, filtration and transfer steps. Instead we added the liquid samples directly to the photo-reactor by opening the Z-connector at the reactor head including subsequent thorough de-

gassing. In this way, by the measurement of the same sample (both frozen and liquid) with the different processing paths, we could cancel out the mass and ^{14}C content of the water or ice sample itself. In principle, this would allow to derive the blank contribution from the sample treatment.

First, with the known oxidation blank and the results of the liquid aliquot ($m_{\mathrm{tot}}^{\mathrm{liquid}}$ and $F^{14}C_{\mathrm{meas}}^{\mathrm{liquid}}$), we calculated the carbon mass and ^{14}C content of the water sample (m_{matrix} and $F^{14}C_{\mathrm{matrix}}$) from the isotopic mass balance equation (Eq. 3.1). For the frozen aliquot, the isotopic mass balance furthermore includes the blank contribution from the ice sampling, melting, filtration and transfer steps (m_{sam} and $F^{14}C_{\mathrm{sam}}$). From the measurement results of both the liquid and frozen ($m_{\mathrm{tot}}^{\mathrm{ice}}$ and $F^{14}C_{\mathrm{meas}}^{\mathrm{ice}}$) aliquot, m_{sam} and $F^{14}C_{\mathrm{sam}}$ could be directly calculated[2]. Thus, the overall blank mass m_{blank} is the sum of both contributions m_{sam} and m_{oxi} and $F^{14}C_{\mathrm{blank}}$ corresponds to the mass-weighted average of $F^{14}C_{\mathrm{sam}}$ and $F^{14}C_{\mathrm{oxi}}$.

Although this approach promises an elegant solution to determine the overall blank, we could not apply it. Since all contributions to m_{tot} are very low, the associated uncertainties are high. Furthermore, a single result (m_{sam} and $F^{14}C_{\mathrm{sam}}$) requires two correlated, successful measurements (liquid and frozen aliquot of the same sample). Despite the general low number of data-points, this lowers the available data further. Thus, we could not produce a meaningful estimation of the overall blank from the eight measurements that we performed.

Therefore, in a second approach, we determined an upper limit of the overall blank from the measurement of ultra-pure ice (UPI) samples. UPI samples are also known as 'blank ice' and used to determine method blanks or detect contaminations for various trace-element analyses used in our laboratory. The reason why we did not choose this option from the start is that although ultra-pure, UPW in principle still does contain non-negligible amounts of DOC. However, the system we use[3], does not only deionize and filter the water, it even photo-oxidises it. According to manufacturer's data [EMD Millipore Corp., 2013], the TOC content is below 5 μg C/kg for the supplied UPW. Thus, in spite of the difficulties associated with the first

[2] $m_{\mathrm{sam}} = m_{\mathrm{tot}}^{\mathrm{ice}} - m_{\mathrm{oxi}} - (m_{\mathrm{tot}}^{\mathrm{liquid}} - m_{\mathrm{oxi}}) \frac{m_{\mathrm{sample}}^{\mathrm{ice}}}{m_{\mathrm{sample}}^{\mathrm{liquid}}}$ and

$F^{14}C_{\mathrm{sam}} = \left[m_{\mathrm{tot}}^{\mathrm{ice}} F^{14}C_{\mathrm{tot}}^{\mathrm{ice}} - m_{\mathrm{oxi}} F^{14}C_{\mathrm{oxi}} - \left((m_{\mathrm{tot}}^{\mathrm{liquid}} - m_{\mathrm{oxi}}) \frac{m_{\mathrm{sample}}^{\mathrm{ice}}}{m_{\mathrm{sample}}^{\mathrm{liquid}}} \right) \left(\frac{m_{\mathrm{tot}}^{\mathrm{liquid}} F^{14}C_{\mathrm{tot}}^{\mathrm{liquid}} - m_{\mathrm{oxi}} F^{14}C_{\mathrm{oxi}}}{m_{\mathrm{tot}}^{\mathrm{liquid}} - m_{\mathrm{oxi}}} \right) \right] \left(m_{\mathrm{tot}}^{\mathrm{ice}} - m_{\mathrm{oxi}} - (m_{\mathrm{tot}}^{\mathrm{liquid}} - m_{\mathrm{oxi}}) \frac{m_{\mathrm{sample}}^{\mathrm{ice}}}{m_{\mathrm{sample}}^{\mathrm{liquid}}} \right)^{-1}$

where $m_{\mathrm{sample}}^{\mathrm{ice}}$ and $m_{\mathrm{sample}}^{\mathrm{liquid}}$ are the masses of the frozen and liquid aliquots.

[3] Model Milli-Q Direct with UV lamp from Merck Millipore

approach, we decided to use the UPW for the UPI samples and neglected the contribution of the UPW to the measured DOC mass and ^{14}C content. In this way, we estimated an upper limit for the overall procedural blank m_{blank} and $F^{14}C_{\text{blank}}$.

We filled UPW into PETG containers and froze them to prepare UPI blocks. Then, the UPI samples were cut from the blocks in the cold room and processed in the same way as normal ice samples (see Sec. 2.6). In this way, we successfully measured the DOC mass and ^{14}C content of four UPI samples with masses from 186 ml to 309 ml (see App. E , samples 'cal35', 'cal36', 'cal39', 'cal40'). The extracted carbon masses (3.0 – 4.3 μg C) did not correlate with the UPI sample masses, negating a first order sample mass dependence of the blank mass. Thus, likewise as for the POC blank (see Sec. 3.3.4), we calculated the procedural blank mass simply as the average carbon mass of these four UPI samples, and give the respective standard deviation as an estimate of the uncertainty. The procedural blank $F^{14}C_{\text{blank}}$ was calculated as the mass-weighted average of these samples, the mass-weighted standard deviation is given as an estimate of the uncertainty:

$$m_{\text{blank}} = (3.5 \pm 0.6)\,\mu\text{g C} \quad \text{and} \quad F^{14}C_{\text{blank}} = 0.65 \pm 0.04$$

Due to the limited amount of measurements and the low carbon masses, we could not apply more sophisticated methods to determine the procedural blank. Nevertheless, the determined blank mass represents a reasonable upper limit for the procedural blank of the complete extraction method.

In comparison with the oxidation blank mass of 2.0 ± 0.5 μg C, the total blank mass is only 1.5 μg C higher. This amount corresponds to the contamination that is related to the ice preparation, melting, filtration and transfer steps. This value is also well in line with the POC blank mass (see Sec. 3.3.4). This is promising, since for the PO^{14}C method similar processing steps are performed.

The blank ^{14}C content is – considering the uncertainties – similar for both determined procedural blanks $F^{14}C_{\text{oxi}}$ and $F^{14}C_{\text{blank}}$. Also this fits the expectations, since the contaminations are likely to have similar sources: the UPW which is the major cleaning agent for the glass setup and the ice samples.

3.3.4 Particulate organic carbon blank

Although it has rather been described as a side product of the extraction procedure of DOC, the POC fraction itself is a very valuable proxy. Most successful radiocarbon analyses that have been performed up to now in our

group, rely on the well-established and proven method for PO^{14}C analysis of ice samples [Uglietti et al., 2016]. While this work focusses on DOC analysis, the POC fraction is separated from the liquid sample during the filtration step and this filter is readily available once the setup can be opened after the DOC oxidation (see Sec. 2.6.7). This quartz fibre filter can be processed according to the standard method described in Uglietti et al. [2016], which involves acidification for IC removal, drying in a laminar flow box, thermo-optical OC/EC separation and online ^{14}C AMS analysis of the thereby produced CO_2.

We determined the procedural blank for the POC extraction with our setup in the same way as for the original method [Jenk et al., 2007] by the measurement of blank ice samples produced from UPW. For this, we analysed the quartz fibre filters from the previous measurements of UPI samples (Sec. 3.3.3). Although the in total eight UPI samples only produced four DOC results, they yielded seven usable filters for the POC blank determination.

To analyse the filters, each filter was removed from the setup after DOC extraction, dried in a laminar flow box for 1 – 2 hours, wrapped in aluminium foil and frozen. After frozen transport from Paul Scherrer Institute (PSI) to University of Bern, the filters were thawed and acidified with 50 μl of 0.2 M hydrochloric acid, rinsed with 50 ml of UPW, dried in a laminar flow box and frozen again. For ^{14}C analysis, the filters were thawed, punched to rectangular pieces to fit the sample holder of the Sunset OC/EC Analyser and were combusted according to the temperature protocol 'Swiss 4S' in TC mode [Zhang et al., 2012]. To have sufficient carbon mass for reliable ^{14}C analysis, we pooled two to three filters for each combustion. The produced CO_2 sample was directly introduced via the GIS to the MICADAS for ^{14}C analysis. To exclude a blank contribution from the filters themselves or the drying, freezing and thawing steps, we also analysed blank filters. These blank filters confirmed the negligible blank contribution of these steps: even when three filters were pooled, their carbon mass was too low for ^{14}C analysis. The results of the POC blank measurements are given in App. E ('cal35-POC', 'cal36-POC' and 'cal40-POC').

We calculated the POC procedural blank mass simply as the average carbon mass of these seven filters, and give the respective standard deviation as an estimate of the uncertainty. The POC procedural blank F^{14}C was calculated as the mass-weighted average of these filters, the mass-weighted standard deviation is given as an estimate of the uncertainty:

$$m_{\mathrm{POC\,blk}} = (1.3 \pm 0.4)\,\mu\mathrm{g\,C} \quad \text{and} \quad F^{14}\mathrm{C}_{\mathrm{POC\,blk}} = 0.66 \pm 0.04$$

The blank mass is convincingly low and gives first confidence that the POC analysis performed with this setup is comparable to the PO^{14}C method and setup that is used routinely in our group. Here, a long-term (10 years) POC blank of $(1.3 \pm 0.6)\,\mu$g C with $F^{14}\mathrm{C} = 0.69 \pm 0.13$ has been determined [Uglietti et al., 2016].

3.4 Discussion

As shown in the previous sections, the extraction setup is operational and well characterised. Here, we summarise its benchmarks and limitations and compare it with existing methods. A validation study is presented in Chapter 4.

3.4.1 Overview

The setup and method that we have developed for the analysis of radiocarbon in DOC from ice samples meets the requirements of ultra-clean and efficient carbon extraction. This is possible thanks to several features, such as using the minimal invasive UV photo-oxidation method. Moreover, we perform the complete sample treatment under inert gas conditions and we chose only dedicated materials for the individual components of the setup.

We show a summary of the benchmarks and performance of the extraction system in Tab. 3.3. The procedural blank is low for the DOC extraction and comparable with the existing method for the POC extraction. Furthermore, DOC is oxidised with a high yield. Even for more volatile organic species, such as formate and acetate, we found similar oxidation efficiencies as for PHP. Therefore, the method provides the anticipated efficiency and accuracy to analyse DO^{14}C in ice samples from alpine glaciers.

As we confirmed by measuring liquid isotopic standard solutions, the appropriate blank correction is consistent within the given uncertainties. In a conservative approximation, samples with a carbon content of three times the blank mass can be reliably analysed. When we consider the photoreactor volume that limits the maximum sample size, this translates to optimal DOC concentrations of more than 33 μg C/kg ice. In this respect, our method is ready for application to typical Alpine ice samples [Legrand et al., 2013a].

To illustrate the process and timing of a complete measurement, we show the CO_2 concentration signal as recorded with the NDIR detector in Fig. 3.4. In accordance with Sec. 2.6, after installation of the glass setup,

data specification		
sample volume	$\leq 300\,\mathrm{ml}$	see comment 1 in caption and Sec. 2.6
sample carbon mass	$\leq 695\,\mu\mathrm{g\ C}$	uncertainty $\approx$ 3%, resolution $0.04\,\mu\mathrm{g\ C}$, see comment 2 in caption and Sec. 3.1.4
sample DOC concentration	$\geq 33\,\mu\mathrm{g\ C/kg\ ice}$	see comment 3 in caption and Sec. 3.1.4
UV irradiation power	$2 \times 250\,\mathrm{W}$	see Sec. 2.3.2
UV irradiation wavelengths	$\geq 210\,\mathrm{nm}$	UV-C – visible light, see Sec. 2.3.2
UV irradiation time	45 min	see Sec. 3.2.2
UV irradiation efficiency for oxalic acid	$(85 \pm 7)\%$	see Sec. 3.2.3
procedural blank for PO^{14}C analysis	$m_{\mathrm{POC\,blk}} = (1.3 \pm 0.4)\,\mu\mathrm{g\,C}$ $F^{14}\mathrm{C}_{\mathrm{POC\,blk}} = 0.66 \pm 0.04$	see Sec. 3.3.4
oxidation blank for DO^{14}C analysis	$m_{\mathrm{oxi}} = (2.0 \pm 0.5)\,\mu\mathrm{g\,C}$ $F^{14}\mathrm{C}_{\mathrm{oxi}} = 0.57 \pm 0.11$	see Sec. 3.3.2
procedural blank for DO^{14}C analysis	$m_{\mathrm{blank}} = (3.5 \pm 0.6)\,\mu\mathrm{g\,C}$ $F^{14}\mathrm{C}_{\mathrm{blank}} = 0.65 \pm 0.04$	see Sec. 3.3.3
approx. CO_2 sample production time	4 hours	see Fig. 3.4

Table 3.3: Summary on the benchmarks and performance of the extraction system. Comment 1: reactor volume (350 ml) minus acidification solution (50 ml), consider a previous mass loss of $\approx$ 25% for ice sample decontamination. Comment 2: the lower bound for the sample mass is determined by the AMS system for ^{14}C analysis and uncertainties arising from blank correction, typically it is a few μg C. Comment 3: assuming a sample mass larger than three times the procedural blank mass.

further preparations and cleaning with UHP helium, the cleaning sample is introduced to the photo-reactor. It is acidified and degassed while being irradiated in parallel. The degassing of IC of the cleaning sample is seen in the first drop of the CO_2 concentration signal, marked '1'. The oxidation of OC produces CO_2 and thus gives an additional signal ('2') until all OC is oxidised and the cleaning oxidation is finished ('3'). Except for 50 ml acidification solution, the cleaning sample is removed and the meanwhile melted ice sample is introduced to the photo-reactor and degassed from IC ('4'). Once the carrier gas stream has a CO_2 concentration below 1 ppm,

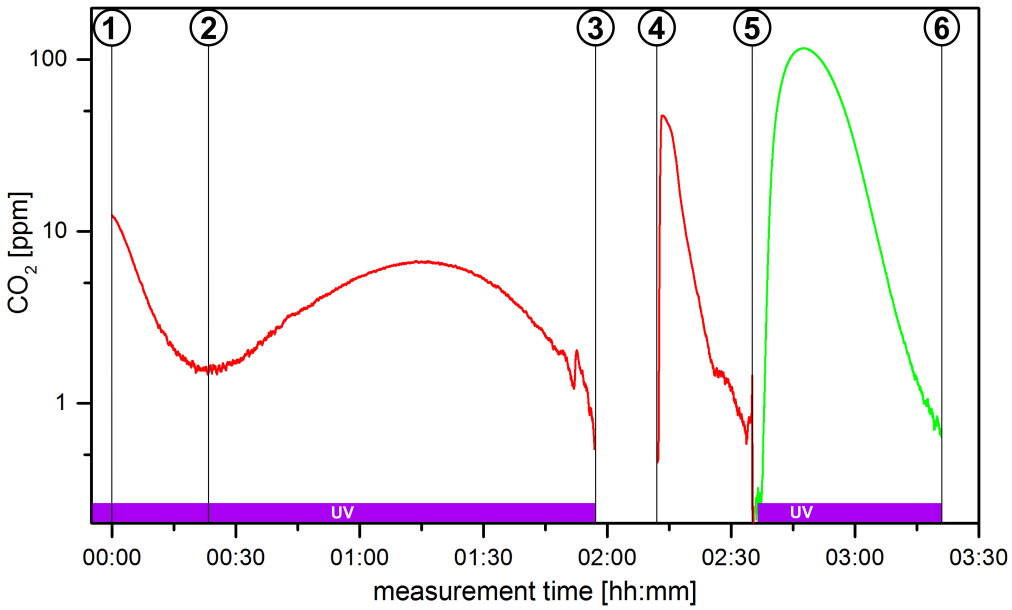

Figure 3.4: CO_2 concentration signal as recorded with the NDIR detector for a complete extraction. In red, we show the recorded CO_2 concentration signal over the measurement time for a UPI sample. For illustration, we also show in green the CO_2 concentration signal of the DOC sample which is oxidised (here a formate standard) and which is captured in the CO_2 trap at normal operation mode (flatline of the red signal). The violet bar indicates active UV irradiation; the numbers refer to the description in the text.

the cryogenic CO_2 trap is activated and thus the CO_2 concentration drops to zero ('5', flatline of the red signal). For illustration, we show in Fig. 3.4 also a hypothetical CO_2 signal in green, corresponding to the CO_2 that is captured in the CO_2 trap during the 45 min long UV oxidation ('6'). Finally, the trapped CO_2 is sampled in the vacuum line.

As can be seen, the cleaning step before each extraction is the most time intensive part of the entire process. However, for a low blank and reproducible measurements this reset is required and can easily be monitored thanks to the NDIR detector.

3.4.2 Limitations

In general, a major limitation is the low sample throughput-rate, although we already could increase it to two samples per day. Thanks to the introduction of an abstraction system, it is possible to reuse the same setup for several samples without the need to dismantle it for the sample removal after analysis. Still, this low throughput-rate only allows us to analyse only selected reference samples. Furthermore, due to the long analysis time per

sample, it is difficult and time consuming to determine background values or to perform standard measures of quality control. However, both the oxidation time and the pre-cleaning step could in principle be shortened by increasing the UV irradiation power, i.e. the use of more UV lamps. In addition, the degassing of the liquid sample can be accelerated by higher carrier gas flow-rates.

Furthermore, due to the rather elaborate extraction protocol the risk to lose a sample is considerable and can only be minimised by sound training and thorough operation.

As our experience with the glass setup shows, the filtration unit (see Sec. 2.2.4) can still be optimised. In some cases, the quartz fibre filter got disrupted during filtration due to missing support from the frit beneath. This caused a loss of POC from the filter and respectively POC input to the sample in the photo-reactor. However, a revised version of the filtration unit with lifted frit can solve this issue.

Another inherent limitation of the analysis of DOC is the requirement of cold glacier ice samples. From a pilot study with ice samples from the ablation region of Rhone glacier (Swiss Alps, 2250 m), we presume a comparable effect as for major ions or other dissolved species in temperate ice. While particulate species such as POC and BC are less affected by mobilisation from percolating melt-water, dissolved species are washed out and their signal is lost [Eichler et al., 2001; Pavlova et al., 2015]. Thus, while we could find datable POC in our pilot study, no carbon deriving from DOC could be detected.

Finally, for samples with lower carbon content, such as polar samples, the method still needs further improvement. One way to further lower the blank mass is to omit the filtration step for samples with a low POC content. This simplification is valid since in this case the determined TOC corresponds in a first order approximation to DOC [Legrand et al., 2013a]. Another option is to extend the maximal possible sample volume. While the rest of the setup can be reused in the same way, simply a taller photo-reactor needs to be used in combination with a longer oxidation time to process a larger sample.

3.4.3 Comparison with existing methods

To put our setup in context, we compare it with the two existing devices for radiocarbon analysis of DOC from glacier ice samples.

The method of May et al. [2013] follows the same extraction steps as used in our work, however the filtration is omitted due to contamination

reference	oxidation efficiency	procedural blank
this work	$(85 \pm 7)\%$ for oxalic acid	$m = (3.5 \pm 0.6)\,\mu g\,C$ $F^{14}C = 0.65 \pm 0.04$
May et al. [2013]	$(96 \pm 1)\%$ for oxalic acid	$m = (6 \pm 3)\,\mu g\,C$ $F^{14}C = 0.71 \pm 0.17$
Steier et al. [2013]	$(64 \pm 17)\%$ for DOC from ice samples	$m = (1.1 \pm 0.7)\,\mu g\,C$

Table 3.4: Comparison of the oxidation efficiency and procedural blank for the existing methods for DO^{14}C analysis of glacier ice samples.

problems. Hence, the extracted OC fraction should rather be termed 'UV oxidisable OC'. The oxidation method is also a wet photo-oxidation, however a low-pressure Hg lamp is used for internal UV irradiation of the liquid sample. The radiocarbon analysis is also performed directly on the gaseous CO_2 sample with a MICADAS AMS.

Despite the difficulties encountered when measuring real ice samples [May, 2009], a high oxidation efficiency and a procedural blank mass of $6 \pm 3\,\mu g$ C were reported (see also Tab. 3.4). The photo-reactor allows to process samples of up to 750 ml volume and the detection limit of the manometry cell is $2\,\mu g$ C. Although our extraction setup is designed in a similar way, the use of dedicated materials and the fact that we perform the full sample treatment under inert gas conditions allow to achieve an even lower procedural blank whilst including the POC separation by filtration. Furthermore, in contrast to the supermodern ^{14}C results for real ice samples explained by the hypothesis of in-situ production of ^{14}C in DOC in ice [May, 2009; Hoffmann, 2016], we did not observe such an influence in our validation study with real ice samples (see Chapter 4).

The method of Steier et al. [2013] follows a different approach. Here, ice samples of several kilogram mass are melted and filtered in the field, acidified and lyophilised to less than 1 ml volume. In a batch mode, nine samples are UV oxidised in parallel by external UV irradiation of small vials with four low-pressure Hg lamps. After 2 hours of oxidation, the produced CO_2 is graphitised for AMS analysis.

The reported carbon yield for DOC from real ice samples is $(64 \pm 17)\%$, which is sufficient for a comparative study as performed in Singer et al. [2012]. However, possible loss of volatile organic species during the lyophilisation step needs to be considered. The possibility to analyse several samples in parallel strongly reduces the effective analysis time per sam-

ple. The reported procedural blank is very low (see also Tab. 3.4), but only accounts for the sample processing from the UV oxidation step and onwards. Thus it can be rather compared to the oxidation blank of our work with $m_{\mathrm{oxi}} = (2.0 \pm 0.5)\,\mu\mathrm{g\,C}$, while no information is given on DOC input from the ice sampling, filtration, acidification and lyophilisation steps.

Chapter 4

Validation

To validate and to further investigate this novel method for radiocarbon analysis of glacier ice, we apply it to well-dated ice samples. For this purpose, we use ice samples from the Juvfonne ice patch, which have already been used for previous validation studies for the $PO^{14}C$ method.

4.1 Site and ice sample description

Juvfonne ice patch is a small perennial ice patch located in Jotunheimen in central southern Norway (61.676 °N, 8.354 °E). It has an approximate area of $500 \times 350\,m^2$ with a maximum depth of 16 m and is situated at an altitude of 1900 m a.s.l.. The ice body has a temperature of -2 to -4 °C and lies on permafrost [Ødegård et al., 2017]. The site is of great interest for glacial archaeology because the ice patch is vanishing due to enhanced melting and thus more and more relicts from prehistoric reindeer hunting are revealed [Nesje et al., 2012].

The fact that the Juvfonne ice body contains both sections of clear ice as well as layers with organic debris such as plant fragments, makes this site also particularly useful for radiocarbon validation studies. In this way, the well-established method of conventional ^{14}C dating of macro-fossils can be applied in parallel to novel methods such as $PO^{14}C$ or $DO^{14}C$ analysis and directly corroborate or refute their use as a proxy for the real age of the ice sample. Furthermore, Juvfonne is very accessible and also the sampling of old ice can be done easily thanks to an artificial ice tunnel that extends into the ice patch (see also Fig. 4.1). In general, high OC concentrations are found in all parts of the ice and thus the AMS analysis is not hindered by low carbon masses.

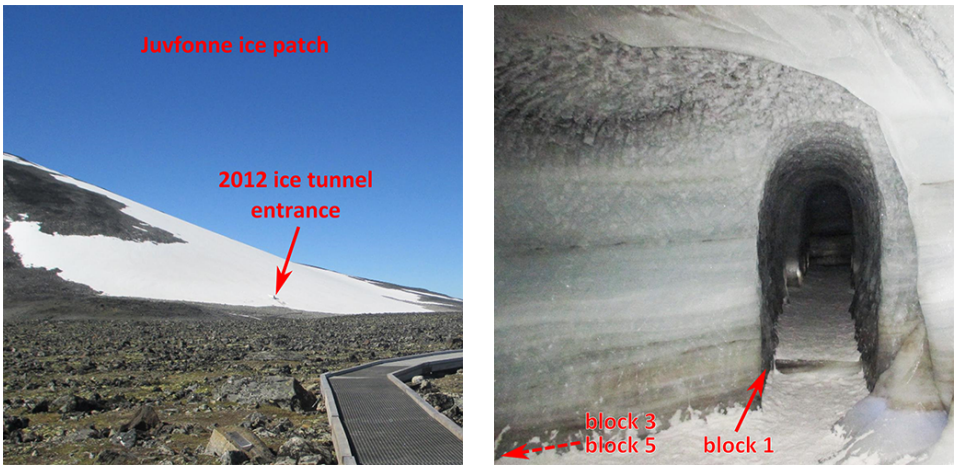

(a) **(b)**

Figure 4.1: (a) Juvfonne ice patch as seen in August 2015 with the entrance to the ice tunnel from 2012. (b) Inside the 2012 ice tunnel, where the ice blocks were sampled with an electric chain saw. Block 1 was taken close to the tunnel floor at the step, block 3 and 5 were taken adjacent to a higher lying plant fragment layer to the left of the picture. Both photographs by Chiara Uglietti.

In a first validation study, eleven samples from the ice tunnel of 2010 were analysed with the PO^{14}C method and compared to ^{14}C ages of adjacent organic remains. The age of the samples ranged from modern to more than 2000 cal BP and good agreement with the conventional results was found [Zapf et al., 2013].

The samples that we used for this validation study were taken from a new, 70 m long ice tunnel, excavated in 2012. In August 2015 five ice blocks were extracted with a pre-cleaned electric chainsaw from the walls of the ice tunnel (see also Fig. 4.1b)). The ice samples contain clear ice and were located adjacent to a plant fragment layer. All ice blocks were subdivided to smaller pieces and transported frozen to PSI. A first set of POC measurements was performed at four of the ice blocks with two samples each to further validate the standard method for PO^{14}C analysis. Good agreement with the age of the adjacent plant fragment layer that was conventionally dated to (6608 $\pm$ 53) cal BP was found, adding another line of evidence that the PO^{14}C method gives the true age of the ice sample [Uglietti et al., 2016; Ødegård et al., 2017].

Here, we used left-over ice samples from the ice blocks 1, 3 and 5 to compare our new method with the existing PO^{14}C method. Six ice samples were analysed according to the described method (see Sec. 2.6) and yielded carbon mass and F^{14}C for the DOC and the POC fraction extracted from

sample	AMS lab number	ice block	method	$F^{14}C$	cal age (cal BP)	C ($\frac{\mu g\,C}{kg}$)
juv1-1	4184.1.1	1	POC	0.48 ± 0.01	7145 – 6447	1383
juv1-2	4380.1.1	1	POC	0.46 ± 0.01	7415 – 7022	1175
juv3-1	4186.1.1	3	POC	0.40 ± 0.01	8371 – 7937	794
juv3-2	4382.1.1	3	POC	0.44 ± 0.01	7786 – 7331	185
juv5-1	4187.1.1	5	POC	0.40 ± 0.01	8348 – 7937	1415
juv5-2	4383.1.1	5	POC	0.45 ± 0.01	7561 – 7026	940
juv1-3	5469.1.1	1	POC*	0.45 ± 0.03	7917 – 6664	28
juv1-4	5470.1.1	1	POC*	0.47 ± 0.01	7156 – 6675	140
juv3-3	5471.1.1	3	POC*	0.43 ± 0.01	7917 – 7336	102
juv3-4	5472.1.1	3	POC*	0.41 ± 0.01	8170 – 7879	654
juv5-3	5473.1.1	5	POC*	0.46 ± 0.01	7419 – 7004	120
juv5-4	5474.1.1	5	POC*	0.42 ± 0.01	7916 – 7611	694
juv1-3	sample lost	1	DOC	-	-	152
juv1-4	5481.1.1	1	DOC	0.48 ± 0.01	6940 – 6474	105
juv3-3	5484.1.1	3	DOC	0.40 ± 0.01	8513 – 7959	104
juv3-4	5483.1.1	3	DOC	0.43 ± 0.01	7791 – 7519	299
juv5-3	5482.1.1	5	DOC	0.49 ± 0.01	6715 – 6297	233
juv5-4	sample lost	5	DOC	-	-	203

Table 4.1: Overview of the used ice samples for method validation. All samples were taken from the Juvfonne 2012 ice tunnel in Norway. Duplicate samples from three different ice blocks were analysed for ^{14}C content and carbon mass with different methods: 1. the standard method for POC extraction ('POC', [Uglietti et al., 2016]), 2. POC extraction according to the standard method, but with the setup of this work ('POC*'), 3. the novel DOC extraction method ('DOC', this work). All results for $F^{14}C$ have been blank corrected with the respective procedural blank. The calibrated ages (cal age) are given in years before present (cal BP, with BP = 1950), their age range corresponds to the 1σ interval. Calibration was done with OxCal v4.2 [Bronk Ramsey and Lee, 2013] using the IntCal13 calibration curve [Reimer et al., 2013]. For the carbon concentration (C) no error is indicated as it is strongly exceeded by the natural variability of carbon concentration in these ice samples. The results for POC are taken from Ødegård et al. [2017], the measurement data for POC* and DOC are found in App. E.

the ice samples. For means of differentiation, we label results for POC obtained with the standard method as 'POC', while results from this new setup are labelled 'POC*'. We show an overview on the samples that we use for this validation in Tab. 4.1.

4.2 Particulate organic carbon

A first validation of this setup is to compare the results of the extracted POC fraction. Since the method is a copy of the well-established standard method for PO^{14}C analysis [Jenk et al., 2007; Uglietti et al., 2016], we expect similar ^{14}C results for different ice samples of the same ice blocks. As described in Sec. 2.6 and in Sec. 3.3.4, only the filtration itself is done in a different setup, the further filter treatment is similar and the combustion step for OC/EC separation is the same.

In Fig. 4.2 we show the F^{14}C results of the validation ice samples. For each of the three different ice blocks, two ^{14}C measurements with the standard PO^{14}C method existed, shown as black open circles with their respective uncertainty. We analysed additionally each two ice samples from the same ice blocks with the method of this work, yielding results for the DOC and the POC (denoted as 'POC*') fraction. The F^{14}C results for POC* are shown as red open circles. In addition, the mass-weighted mean F^{14}C value is shown for each ice block and method as filled circle. All F^{14}C results are blank corrected with the respective procedural blank.

When comparing the results for the individual measurements of POC and POC*, we find a pronounced variability between all samples, independent of the used method. This suggests that the inhomogeneity of the distribution of ^{14}C content of OC within the ice samples itself is larger than differences that could arise from the analysis itself. Therefore, it is useful to compare the mean values of the POC and POC* results for each ice block. Here, we find a perfect match within the uncertainties for all three ice blocks. Although only with a limited dataset, this is a first validation that the POC extraction for radiocarbon dating with this new setup yields comparable results for the ^{14}C content of the ice samples. This is also in line with the findings for the POC blank, which was also comparable to the POC blank of the standard method (see Se. 3.3.4).

Along with the ^{14}C content, also the carbon concentration is measured for each sample. Fig. 4.3 gives an overview on the found concentrations of the different OC fractions for all samples. Comparing the POC and POC* concentrations, we find a very strong variability within the different samples from the same ice block. This is probably in the nature of Juvfonne ice patch as this site features very high OC concentrations that are inhomogeneously distributed, such as the adjacent plant fragment layer. However, in particular for block 1 and block 5 a bias that is due to the used method could be recognisable and needs further consideration. As mentioned in

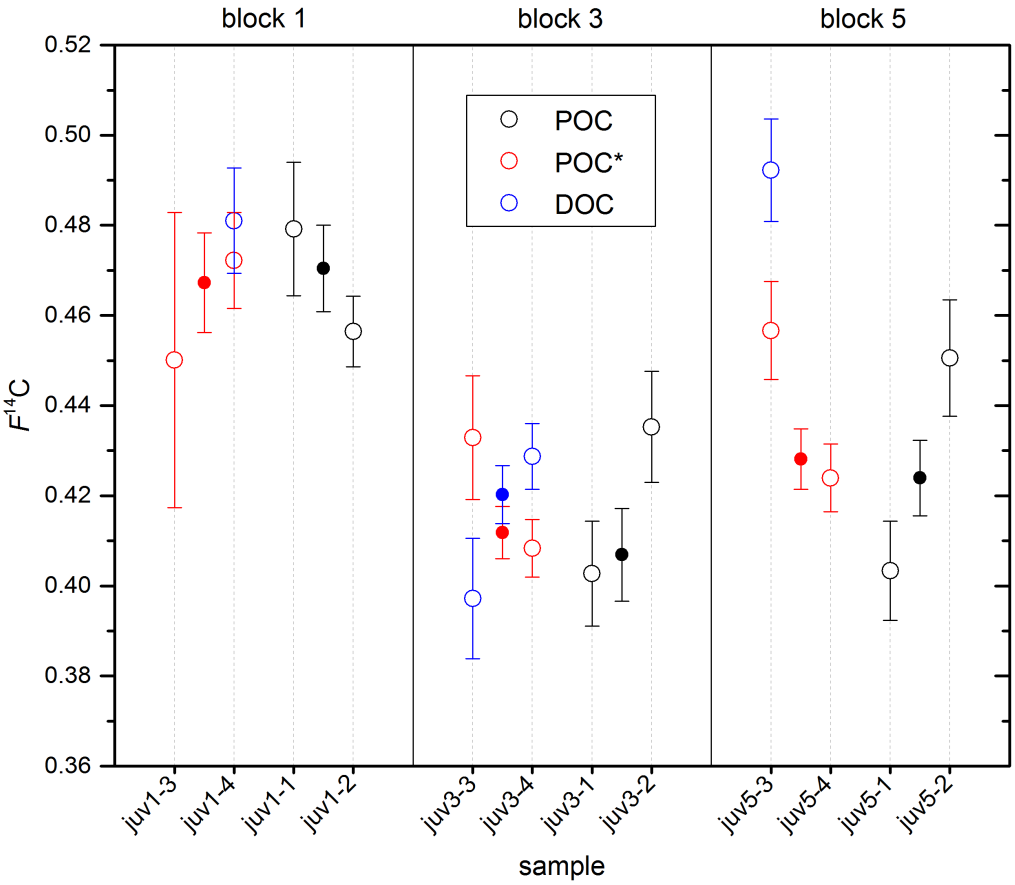

Figure 4.2: $F^{14}C$ of the validation ice samples from Juvfonne ice tunnel, Norway. From each ice block (1, 3 and 5), four ice samples were taken and analysed for ^{14}C. Results obtained with the original method for PO^{14}C analysis are shown in black with the respective uncertainties. The measurements with our new setup reveal the ^{14}C content both from POC as well as from DOC as shown in red and blue, respectively. For all samples, open circles represent individual measurements, filled circles the mean value for each ice block and method. Please note the enlarged y-axis (full scale: 0 – 1).

Sec. 3.4.2, also problems with an incomplete filtration of POC might be a cause for systematically low POC* concentrations.

4.3 Dissolved organic carbon

We extracted the DOC fraction with our new method for all six validation ice samples for AMS ^{14}C analysis. While we could determine the DOC mass for all samples, we had problems with the CO_2 sampling and the AMS measurement itself with two samples. Thus only four validation samples for the ^{14}C content exist from this study (see Tab. 4.1).

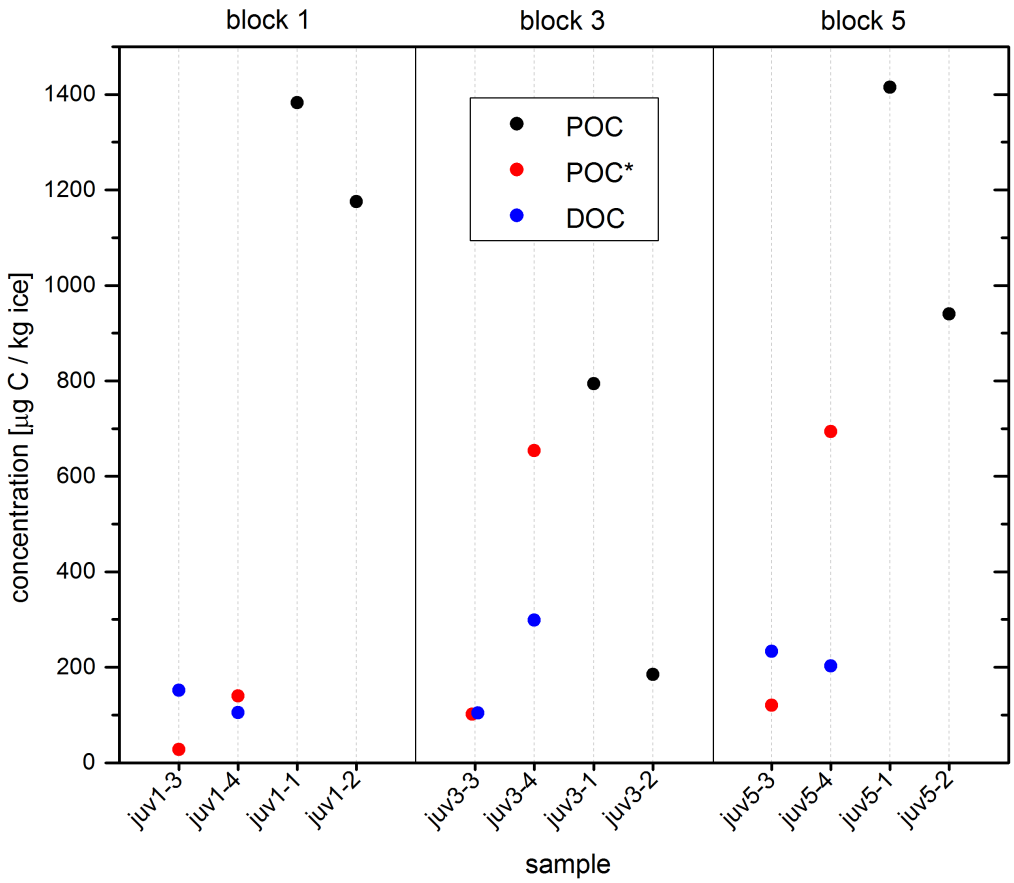

Figure 4.3: Carbon concentrations of the validation ice samples from Juvfonne ice tunnel, Norway. From each ice block (1, 3 and 5), four ice samples were taken and the OC fraction of interest was extracted. Results obtained with the original method for POC extraction are shown in black, the measurements with our new setup reveal the concentration both from POC as well as from DOC as shown in red and blue, respectively.

In Fig. 4.2 the F^{14}C results of the DOC fraction are shown as blue open circles with the respective uncertainties. All results are blank corrected with the procedural blank of the DO^{14}C method and for block 3, where two samples were measured, the respective mass-weighted mean ^{14}C content is shown as a blue filled circle.

Despite the above mentioned strong variability, we find a good overall agreement within the uncertainties. The sample from ice block 1 shows the same F^{14}C as most other samples from this block. Similar to the POC fraction, the DOC results of ice block 3 have larger scatter than their uncertainty, however the mean values for all fractions and methods do fully overlap with each other. Solely the sample from ice block 5 has a higher F^{14}C for DOC than any of the other results for POC. However, with these

validation ice samples, we cannot find any systematic bias of the DOC activities that might indicate methodological, physical or chemical shortcomings. This is also in line with the determined procedural blank for DOC extraction (Sec. 3.3.3).

The DOC concentrations do not show a clear correlation with the POC* concentrations (see blue circles in Fig. 4.3), their overall mean value (183 μg C/kg ice) is lower than for the POC* method (290 μg C/kg ice). Due to the generally high sample to sample variability, a possible unintended input of POC to the DOC fraction (see Sec. 4.2) cannot be detected with these samples. Also an enhanced mobilisation of DOC compared to POC in the case of possible surface melting of the ice patch could explain the lower DOC concentrations (see Sec. 3.4.2). Furthermore, the sample to sample variability of the carbon concentration is strongly reduced for the DOC fraction compared to the POC fraction. A possible explanations is that the DOC is distributed much more homogeneously because of its dissolved nature.

4.4 Conclusions

Although limited in sample number, the results of this first validation study with ice samples from Juvfonne ice patch are very promising and give confidence that both this new extraction setup and the DOC fraction itself are applicable for radiocarbon microanalysis of glacier ice. Both the extracted POC and DOC yield comparable F^{14}C results as found for the samples analysed with the well-established standard PO^{14}C method and suggest that this new extraction system by now performs similar in terms of accuracy and uncertainty.

The glacier ice samples that we analysed for this study span F^{14}C from 0.40 to 0.48, corresponding to calender ages of approximately 8300 to 6300 cal BP. Thus, for a complete validation both modern and very old well-dated ice samples still need to be analysed. Within the uncertainties and in spite of the sample to sample variability, POC and DOC have similar ^{14}C content. In spite of these limitations and the small sample number, no significant differences in F^{14}C between these two OC fractions could be found. Possible differences that could originate from different turn-over times for POC and DOC thus still need further investigations.

In terms of OC concentrations, Juvfonne is a special site. In contrast to classical high-alpine glaciers, where aerosol deposition represents the major OC input, Juvfonne ice patch probably has strong OC influx from local

sources. Because of its low altitude, it is surrounded by biota and even reindeer reside on the ice patch itself in the summer months. Therefore, OC concentrations are generally very high and variable for all fractions. Also the ratio of POC to DOC is unusually high – commonly DOC concentrations are higher than POC concentrations in glacier ice. Hence, while Juvfonne ice patch is very suitable for a validation by comparing the relative ^{14}C content of different methods, the interpretation of absolute values requires to consider the special setting of this site.

The successful validation of the new method for $DO^{14}C$ analysis shows that both the DOC and POC fractions yield comparable age information which is also validated independently with conventional ^{14}C dating. This is in contrast to the findings and hypothesis presented by May [2009] and Hoffmann [2016]. Here, due to super-modern, inconclusive results found for ice core samples from Colle Gnifetti, the authors assume that in-situ produced ^{14}C in the ice matrix could be incorporated to the DOC fraction and bias the results (see also Sec. 1.3.3). In a follow-up study the principal possibility of this in-situ $DO^{14}C$ production was shown by the artificial neutron irradiation of ice samples in the laboratory, concluding that the DOC fraction cannot be used for dating purposes [Hoffmann, 2016].

Even though our validation ice samples are not from Colle Gnifetti, the effect of in-situ $DO^{14}C$ production should also be noticed at Juvfonne ice patch. Although Juvfonne is located at a higher latitude, the neutron flux is still approximately a factor of 3 lower than at Colle Gnifetti because of its low altitude [Lal et al., 1987; Masarik and Beer, 1999]. However, while both ice bodies have ages of several thousand years, Juvfonne ice patch is much thinner and thus the ice matrix has been stronger exposed to neutron irradiation from cosmic rays. Therefore, according to the hypothesis of May [2009] and Hoffmann [2016], a significantly increased ^{14}C content should be found for the samples analysed for DOC compared to POC samples or conventionally dated samples. As discussed in Sec. 4.3 and shown in Fig. 4.2, no such bias was found for the validation ice samples of this study.

Chapter 5

Conclusion and Outlook

In this work, we describe the successful setup, characterisation and validation of a new method for radiocarbon dating of glacier ice. With this new device, few μg C of DOC from ice samples with masses of up to 400 g can be extracted to CO_2 for AMS radiocarbon analysis. For this, ice samples are cut, pre-cleaned, rinsed with UPW and melted under an inert gas atmosphere. By filtration, the POC fraction, which also can be used for ^{14}C analysis, is separated. In a quartz glass photo-reactor the liquid sample is acidified and degassed from IC. By wet photo-oxidation by means of external UV irradiation the DOC in the solution is oxidised to CO_2 and degassed with a helium carrier gas stream. Cryogenic traps first free the carrier gas stream from water vapour and then capture the CO_2 sample. After further cleaning and carbon mass determination in a manometry cell, the CO_2 is sampled to a glass vial. Finally, via a cracker unit and GIS, the gaseous sample is directly introduced to the MICADAS AMS for radiocarbon analysis.

In particular the DOC fraction is very prone to contamination. Thus, to achieve a low and stable procedural blank for this method we perform the complete sample treatment in inert gas conditions and we chose only dedicated materials for the individual components of the setup. Liquid sample handling is done in an all-glass setup while we process the gaseous sample in stainless-steel components with the minimal use of synthetic materials. Furthermore, we use the minimal invasive UV photo-oxidation method without the addition of any chemical oxidants. This method also comprises the high oxidation efficiencies needed for the typically very low carbon concentrations of glacier ice in the μg C/kg ice range.

We characterised the setup with gaseous CO_2 and several ultra-pure liquid DOC standards. For a 45 min long oxidation we found an oxidation

efficiency (85 ± 7)% for oxalic acid, and also more volatile compounds were recovered reliably. We used liquid oxalic acid standards with known, yet different ^{14}C content and determine the procedural blank for DOC oxidation to $m_{oxi} = (2.0 \pm 0.5)\,\mu g\,C$ with $F^{14}C_{oxi} = 0.57 \pm 0.11$. For the overall procedural blank of the DOC extraction including the sample preparation and filtration steps, we used blank ice samples produced from UPW and found $m_{blank} = (3.5 \pm 0.6)\,\mu g\,C$ and $F^{14}C_{blank} = 0.65 \pm 0.04$. From the filters of the same blank ice samples we also determined the procedural blank for POC extraction with this setup to $m_{POC\,blk} = (1.3 \pm 0.4)\,\mu g\,C$ and $F^{14}C_{POC\,blk} = 0.66 \pm 0.04$. These low blank values are well comparable to existing methods and meet the requirements for ultra-clean radiocarbon microanalysis of alpine ice samples. With a maximum sample volume of 300 ml and the requirement of sample masses that are three times larger than the blank mass for a reliable measurement, this translates to a minimal sample DOC concentration of 33 μg C/kg ice.

In a first validation study with ice samples from Juvfonne ice patch we extracted DOC and POC from six ice samples. Ice samples from the same three ice blocks have previously been analysed for PO^{14}C in an independent validation study with conventional ^{14}C dating and thus represent ideal reference samples for method validation. Within the sample-to-sample variability and the uncertainties, we found very good agreement for both DOC and POC ^{14}C content of the samples that were analysed with our new setup compared to the samples that were analysed with the well-established PO^{14}C method. In combination with the low procedural blank, this result suggests that radiocarbon microanalysis with DOC from glacier ice is both technically feasible and physically meaningful. The carbon concentrations of the different OC fractions have to be interpreted cautious at this special site. However, there is an indication for systematically lower POC concentrations when comparing the standard PO^{14}C method with the POC extraction with the new setup. Further investigation concerning potential filtration problems is needed.

In contrast to the hypothesis of in-situ production of DO^{14}C in glacier ice, we did not find any indication for such a biasing process. Within the uncertainties and in scope of the limited amount of samples we cannot support this hypothesis and claim that the DOC fraction can be used for radiocarbon dating of glacier ice.

With these achievements and the well defined operation protocol, the method is applicable by now. However, some limitations still exist.

With only two samples per day, the sample throughput is strongly limited. Although if only selected ice samples are analysed for DO^{14}C, the measurement of background values and processing efficiencies for quality control is laborious. However, to monitor the system hardware (UV lamps, quartz glass photo-reactor) and to further confine the procedural blank, frequent background measurements are needed. The extraction time per sample could be reduced in future by an increased UV photon flux for the oxidation steps and a higher gas flow-rate for the degassing steps. As the proof of concept has been achieved by now, also a sample processing in batch mode could be an option for a revised setup.

The elaborate operation is owed to the challenges of microgram level DOC extraction. Resulting sample loss due to processing errors can only be minimised by thorough training of the operator. In a future setup, an automation of the CO_2 sample processing in the vacuum line would simplify the operation and make it more efficient and reliable. This could be realised with the use of pneumatic valves that are controlled via a LabVIEW interface.

Another beneficial upgrade for the extraction setup would be to use a NDIR detector in flow-through mode. This would allow to monitor the CO_2 concentration in the carrier gas stream during the oxidation step in an online, non-destructive manner. However, restrictions considering contamination control would ask for a very high quality NDIR detector that can guarantee a completely leak-tight operation without outgassing or memory effects.

The filtration of POC showed occasional problems leading to disrupted filters, therefore we suggest a revision of the filtration unit.

Currently the DOC concentration of ice samples is limited to more than 33 μg C/kg ice. This is sufficient for the analysis of typical alpine ice samples, however for the analysis of polar ice samples the method needs further improvement, such as a reduced procedural blank mass. Apart from that, also the use of a revised photo-reactor with larger volume would reduce the required DOC sample concentration thanks to an increased possible sample mass.

Additional and comprehensive characterisation of the extraction setup and its capability could be gained in future by the measurement of further standard substances such as a HULIS standard and also the investigation of its applicability to firn samples and to temperate ice samples. Also the detailed analysis of the effect and need of the POC filtration step would complement the overall understanding of DOC extraction. To consolidate

the existing characterisation and to establish a reliable long-term blank, we recommend to continue with measurements of standards and blanks.

Further method validation and insight to the DOC fraction can be gained by the measurement of ice samples from well-dated alpine ice cores. In this work, ice samples in the age range of approximately 8300 to 6300 cal BP have been analysed. Thus, for a complete validation, both young and very old well-dated ice samples still need to be analysed. Well suited for such studies are samples from the Fiescherhorn ice core (3900 m a.s.l., Alps) that covers the transition from the preindustrial to the industrial era and from Illimani or Colle Gnifetti, which both contain ice from the entire Holocene epoch.

Ice samples from Colle Gnifetti are furthermore of particular interest considering the hypothesis of in-situ DO^{14}C production in glacier ice, which was proposed based on DO^{14}C measurements from this site. Although our results do not support this hypothesis, more measurements are needed to exclude it. Samples from Antarctic blue ice zones that should in principle be depleted in DO^{14}C, but that have been exposed for long times to intense cosmic ray neutrons, could be interesting for further tests, provided DOC concentrations are large enough for analysis.

Another validation approach is the analysis of aerosol filters. Commonly, the ^{14}C content of TOC and WISOC is determined directly from an aerosol filter that has been untreated or water extracted respectively, while the ^{14}C content of WSOC is calculated from those two quantities. A direct measurement of the solution from the water extraction with our setup could be used for a mutual validation study.

The main goal for the future should be the routine measurement of samples with low DOC concentrations, where the standard PO^{14}C method breaks down. This is of particular interest for ice samples from Greenland and Antarctica and will widen the range of radiocarbon dating of glacier ice. Eventually, this will reveal new fascinating secrets of the cryosphere.

Appendices

Appendix A

List of Suppliers

As described in Sec. 2, all components of the extraction setup were carefully chosen and are adapted to the specific needs of radiocarbon microanalysis of DOC in glacier ice. Apart from standard components that we obtained from PSI's goods counter or known retailers, the following table lists the specific model and its supplier for all compounds with dedicated use.

component	model	supplier
glass compounds (except photo-reactor and sampling tubes)	custom made from Boro 3.3	GlasKeller Basel AG `www.glaskeller.ch`
quartz glass photo-reactor	custom made from ilmasil PS	QSIL GmbH Quarzschmelze Ilmenau `www.qsil.com`
tubing, fittings, adapters, manometers silver-plated front ferrules bellow valve (dosing) bellow valve (on/off)	standard Swagelok components SS-6M3-1BL SS-6H-MM-SC11 and SS-6BMRG-MM-SC11 SS-BNTS6MM	Arbor Ventil + Fitting AG (Swagelok) `www.swagelok.com`
steel–glass adapter	custom made for 6 mm OD steel tubes and 4, 6, 8 and 10 mm OD glass tubes	workshop of the Department for Chemistry and Biochemistry, University of Bern
O-ring for melting vessel O-rings for steel–glass adapter spring for filtration unit	EDPM, (75.79 × 3.53) mm Viton, ((4, 6, 8, 10) × 2) mm stainless steel, (d 1.25 × Dm 12.5 × Lo 90.5) mm	Kubo Tech AG `www.kubo.ch`
sampling tubes syringes	glass tubes OD 4 mm full glass, 5 ml, LUER-LOCK	goods counter of the Department for Chemistry and Biochemistry, University of Bern

component	model	supplier
needles	injection cannula 2R2 with LUER-LOCK, OD 1 mm, length 200 mm	Huberlab AG www.huberlab.ch
oxalic acid standards	IAEA-C7, NIST 4990C, fossil (BE 1373)	from stock of LARA, University of Bern
phosphoric acid quartz fibre filters	orthophosphoric acid 85 %, EMSURE, analytical grade Pallflex Tissuquartz Filters 2500 QAT-UP, Pall Laboratory	VWR www.vwr.com
UPW system	Milli-Q Direct with UV lamp	Merck Millipore www.merckmillipore.com
sample container	Verpackungsdose PETG 1000 ml	Semadeni AG www.semadeni.com
turbo pump	HiCube 80 Eco with Pirani transmitter PKR 251	Pfeiffer Vacuum (Schweiz) AG www.pfeiffer-vacuum.de
UV lamps	Modul MH Lamp 250 W XL mit Hg-Strahler Ballast Vorschaltgerät OMB 250 A604K Ignitor Zündgerät ZRM 12-ES/CT	Wissenschaftliche Apparaturen und Industrieanlagen AG www.wisag.ch
NDIR	LI-820A	DMP AG (Licor) www.dmp.ch

component	model	supplier
pressure transmitter	PBMN-25B11AA14402201000	Baumer Electric AG `www.baumer.com`
PID temperature controller	3216/CC/VH/LLXX/R/2XL/S/ENG	Eurotherm Produkte (Schweiz) AG `www.eurotherm.ch`
MFC	C100L with filter FL214SW	Flowmeth AG (Sierra Instruments) `www.flowmeth.ch`
ventilator	TT 200 A	Staumann AG (Extravent) `www.extravent.ch`

Appendix B

Supply electronics box

The supply electronics box hosts several individual electronic components. The user can operate all components in a centralized manner at the electronics box by the individual switches and plugs. All parts are fed by a central, switchable power line that is connected to the mains power. In reference to the numbers assigned in Fig. B.1, the individual components are:

1. The power switch and supply for the protection box ventilator (model 'air inline TT 100 A' by Extravent) that cools the photo-reactor and ventilates ozone produced by the UV lamps, see Sec. 2.5.

2. The e-box ventilator is a conventional case fan to cool the electronics box. It is activated by a power switch and should be used in parallel with the UV lamp power supplies that produce waste heat.

3. The power switch, ignitor (model 'ZRM 12-ES/CT' by Tridonic) and ballast (model 'OBM 250' by Tridonic) for the supply of UV lamp 1 (model 'MH-Module 250W Hg XL' by Heraeus), see Sec. 2.3.2.

4. The power switch, ignitor (model 'ZRM 12-ES/CT' by Tridonic) and ballast (model 'OBM 250' by Tridonic) for the supply of UV lamp 2 (model 'MH-Module 250W Hg XL' by Heraeus), see Sec. 2.3.2.

5. The cold gas system with the PID controller (model '3216' by Eurotherm) user interface, power switch, plug for the thermocouple and connections to the nitrogen line, see Sec. 2.3.3.

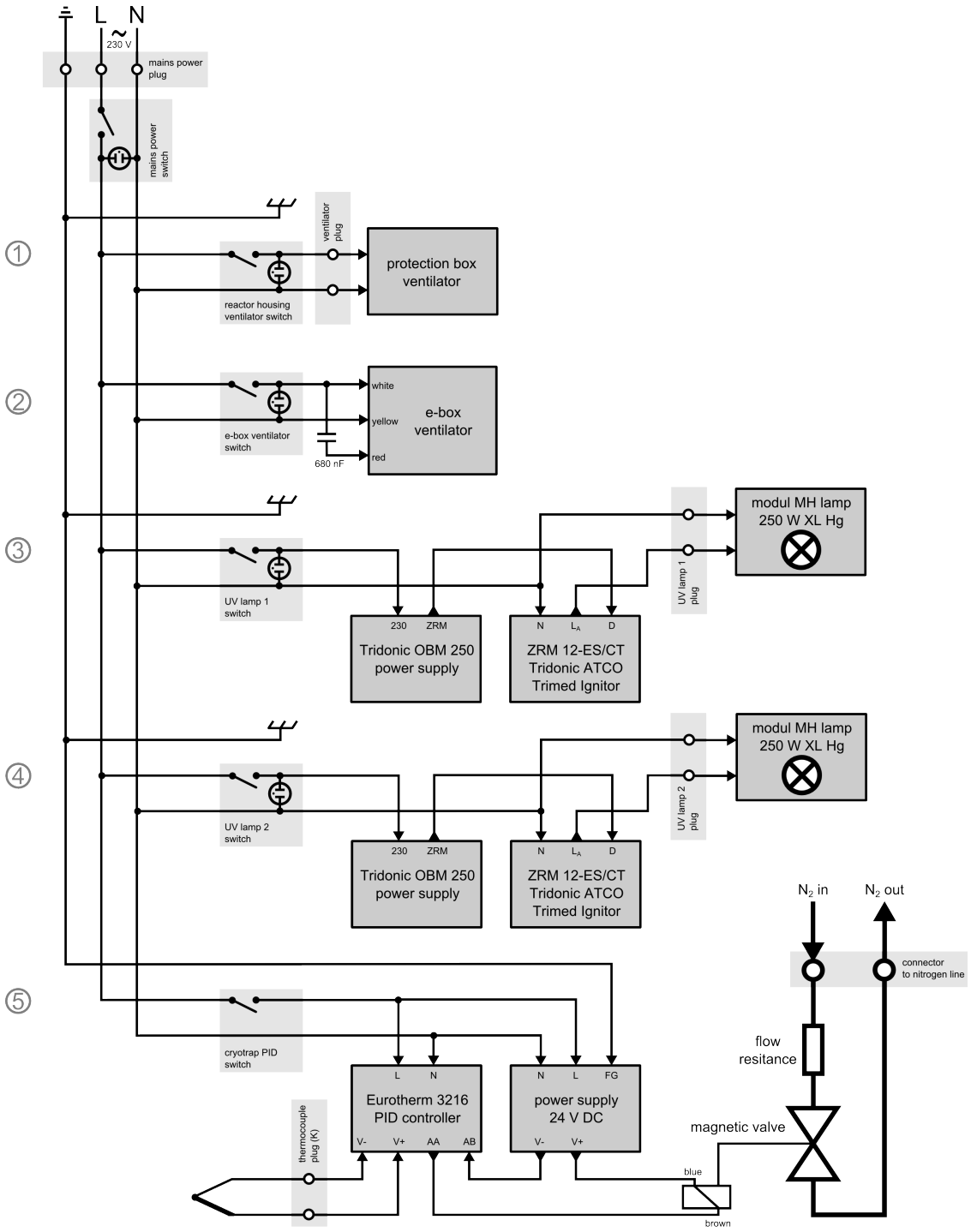

Figure B.1: Circuit diagram of the supply electronics box. Light grey shaded areas indicate switches and plugs that are mounted to the box for user manipulation. Dark grey boxes represent individual components with the respective pin assignment. Thin black lines illustrate electrical connections; thick black lines illustrate gas plumbing. Circled numbers in grey serve as reference for the description in the text.

Appendix C

Calibrations

C.1 Sample mass measurement

To determine the mass of the liquid sample, we measure the fill level of the photo-reactor. By a calibration of the fill level to the corresponding sample volume, the mass of the liquid sample can be derived from the fill level.

Technically, the fill level is measured with the help of a ruler with an adjustable pointer, as shown in Fig. C.1 a). The pointer is set to the bottom of the concave meniscus of the liquid sample in the photo-reactor. The axis of the pointer helps to avoid parallax errors since the eye can align horizontally to it. With this setup, the fill level can be determined to the nearest 0.5 mm with an uncertainty of $\pm$ 0.25 mm.

For the calibration itself, the ruler was zeroed to the bottom of the photo-reactor (outside). The volume of the glass coated stir bar was determined volumetrically to $\mathrm{V_{stirrer}} = 1.8 \pm 0.1\,\mathrm{ml}$ and is subtracted from the sample volume. The empty, assembled photo-reactor was filled with water in 5 ml increments with a pipette for small volumes V and in 25 ml steps with a measuring cylinder for larger volumes, while the corresponding fill level z was recorded. As shown in Fig. C.1 b), the results can be interpolated with a two-part linear fit:

$$V(z) = \begin{cases} \frac{z}{0.04}\frac{\mathrm{ml}}{\mathrm{cm}} - 8.3\,\mathrm{ml} - \mathrm{V_{stirrer}}, & \text{for } z \leq 2\,\mathrm{cm} \\ \frac{z}{0.05}\frac{\mathrm{ml}}{\mathrm{cm}} - 1.9\,\mathrm{ml} - \mathrm{V_{stirrer}}, & \text{for } 2\,\mathrm{cm} \leq z \leq 16\,\mathrm{cm} \end{cases}$$

The sample volume is converted to sample mass with the respective density of water. Temperature effects will influence the calibration only insignificantly, as the laboratory is kept at constant temperature and the water used for calibration has a similar temperature as the liquid sample in the

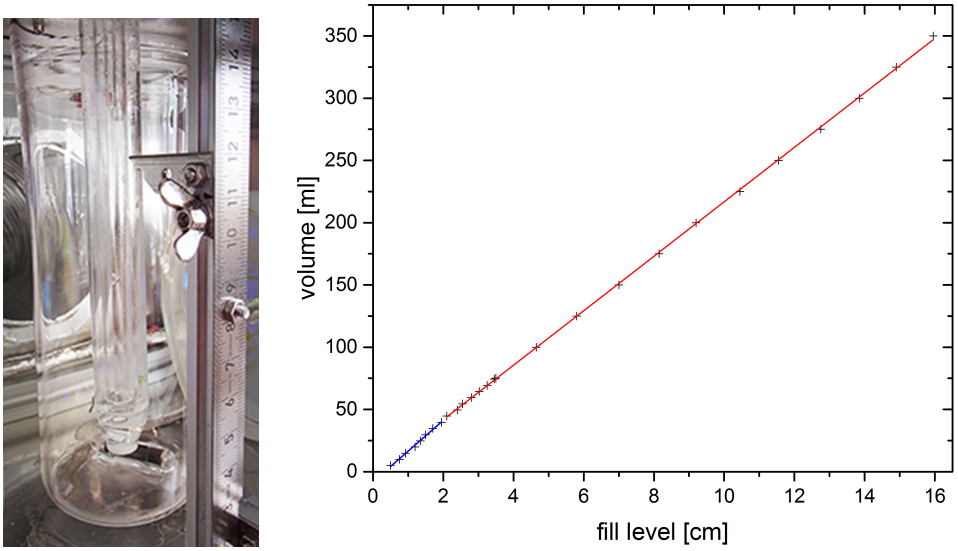

(a) (b)

Figure C.1: (a) Photo of the setup with ruler and adjustable pointer to measure the fill level of the photo-reactor. (b) Calibration of the fill level to the sample volume. Black crosses show the individual measurements, no uncertainty is indicated as it would be below the resolution of the diagram. The blue and red line correspond to the respective linear fits for the different fill level ranges 0 – 2 cm and 2 – 16 cm.

photo-reactor prior to UV irradiation. The reading uncertainty of 0.25 mm translates to an uncertainty in sample mass of 0.6 g.

C.2 Manometry

The manometry cell is used to determine the carbon mass by measuring the pressure of the CO_2 sample in a known volume. The more accurate the volume and pressure are determined, the more accurate the carbon mass can be measured.

C.2.1 External calibration of the pressure transmitter

The piezo-resistive pressure transmitter 'PBMN flush' from Baumer Electric AG measures absolute pressure from 0 to 400 mbar. An external display unit (model 'ZED 601' from Baumer Electric AG) reads the pressure signal and displays it. In order to match the range of the display (0 to 100), the displayed pressure is compressed by a factor of 4. Thus, the display's maximum value of 100 corresponds to 400 mbar and its smallest increment

of 0.01 corresponds to 0.04 mbar. The latter is also the typical uncertainty of a pressure measurement.

Although the pressure transmitter measures absolute pressure and does not rely on a reference value, precision measurements of very low pressures revealed a pressure offset. Therefore, the pressure transmitter was calibrated externally with another, a factor of 50 more precise manometer that works based on capacitive absolute pressure measurement. For the calibration, a 'Baratron' manometer from MKS Instruments was connected to the vacuum line. By the measurement of the same amount of CO_2 in the vacuum line with both manometers over a wide range of masses, a calibration curve was established. The relationship is highly linear and shows only a minute offset. Accounting also for the scaling at the display, the pressure transmitter was calibrated to:

$$p = \frac{4 \cdot d.u. + 0.298}{1.002}\,\text{mbar}$$

where $d.u.$ corresponds to the reading at the display unit.

C.2.2 Calibration of the manometry cell volume

The volume of the manometry cell was calibrated with the help of an external, calibrated volume. In a first step, a homebuilt 'calibration tube' was calibrated gravimetrically by the measurement of its mass when filled with water. Its volume V_{cal} was derived by comparison with the tare weight and the respective density of water at the temperature of the measurement to $V_{cal} = (44.3 \pm 0.7)\,\text{ml}$ (average and standard deviation of eight replicate measurements).

Next, the calibration tube ('CAL') was connected to the vacuum line as shown in Fig. C.2. After evacuation, the manometry cell was loaded with a certain amount of CO_2 and the corresponding pressure p_{MAN} is measured. Stepwise, the CO_2 sample was expanded isothermal to the central manifold and the calibration tube, while the respective pressures $p_{MAN+LIN}$ and $p_{MAN+LIN+CAL}$ were recorded. Since the amount of CO_2 and the temperature are constant for each set of measurement, the ideal gas law can be applied as $p_1 V_1 = p_2 V_2$. Thus, it can be derived:

$$V_{MAN} = V_{CAL}\,\frac{p_{MAN+LIN+CAL}\,p_{MAN+LIN}}{p_{MAN}\,(p_{MAN+LIN} - p_{MAN+LIN+CAL})}.$$

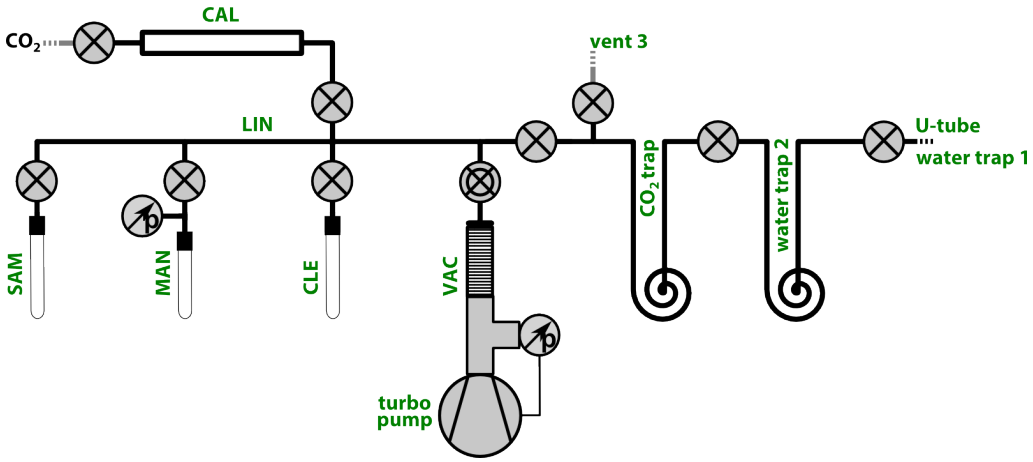

Figure C.2: Setup of the vacuum line for the volume calibration. A legend is shown in Fig. 2.1

We performed 13 pressure measurements over a range from 20 – 100 % full-scale of the pressure transmitter and estimated the volume of the manometry cell to:

$$V_{MAN} = (3.57 \pm 0.08)\,\text{ml}.$$

The uncertainty derives from the error propagation of the individual uncertainties of the pressure measurement and the calibrated volume.

C.2.3 Calibration of the vacuum line parts volumes

In the same way as we calibrated the volume of the manometry cell, also the other individual volumes of the vacuum line sections were calibrated. Tab. C.1 summarizes the results. Except for V_{MAN} and V_{CAL}, where the uncertainty was derived by error propagation, the uncertainty is given as the standard deviation of replicate measurements.

section	volume (ml)
manometry cell (MAN)	3.57 ± 0.08
cleaning tube (CLE)	4.74 ± 0.05
central manifold (LIN)	23.77 ± 0.08
CO_2 trap	60.2 ± 0.1
U-tube	9.54 ± 0.01
calibration tube (CAL)	44.3 ± 0.7

Table C.1: List of volumes of the individual sections of the vacuum line.

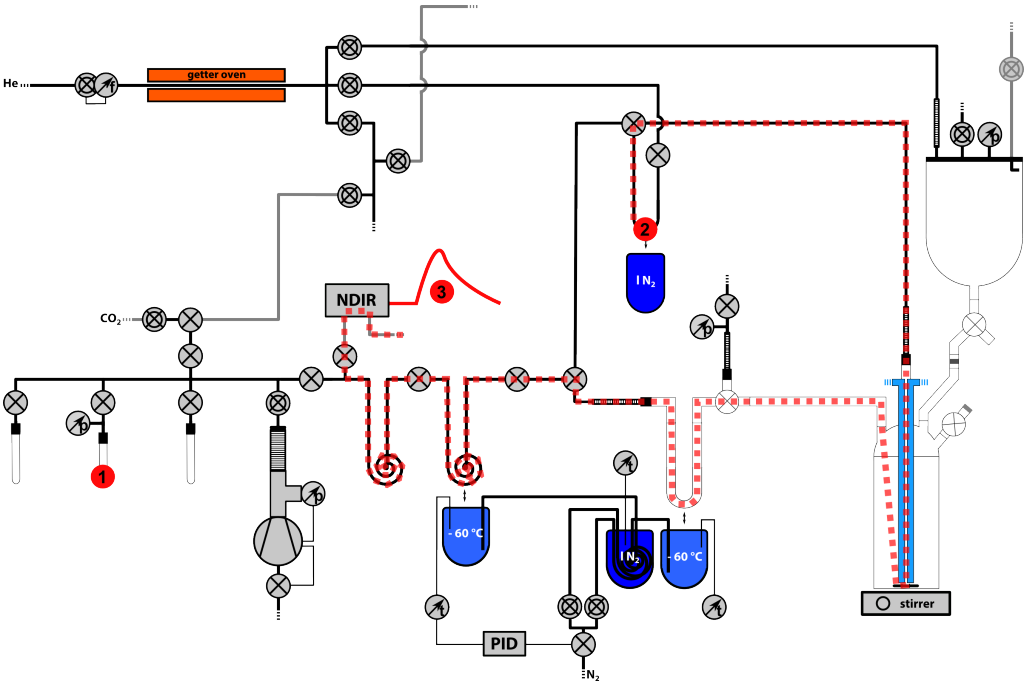

Figure C.3: Experimental setup for the calibration of the NDIR CO_2 detector. '1': a CO_2 sample is quantified in the manometry cell, '2': the U-tube is loaded with the CO_2 sample, '3': the helium carrier gas stream transports the CO_2 sample through the setup and the NDIR CO_2 detector (red, dashed line), where the corresponding signal is recorded. The detailed and complete setup including a legend is shown in Fig. 2.1.

C.3 Non-dispersive infrared CO_2 detector

The NDIR CO_2 detector that is connected in between the CO_2 trap and vent 3 (see Fig. 2.1) is used to measure the CO_2 concentration in the carrier gas stream in flow-through mode. Apart from the confirmation of a CO_2-free gas stream when the CO_2 trap is active, we also use it to monitor the cleaning and degassing steps. The NDIR CO_2 detector can also be used to measure the carbon mass by the integration of a recorded CO_2 concentration signal over time. Although, in the current setup (flow-through), this is a destructive measurement, it offers a fast measurement of the carbon mass since the sample does not need to be trapped and transferred to the manometry cell. This is of particular use for measurements that characterize the setup in terms of carbon mass, such as the determination of the carbon yield of the oxidation (see Sec. 3.2).

However, to detect not only relative changes in CO_2, but to perform reliable measurements of the absolute carbon mass, the NDIR CO_2 needs to be calibrated. For the calibration, we used the experimental setup as shown

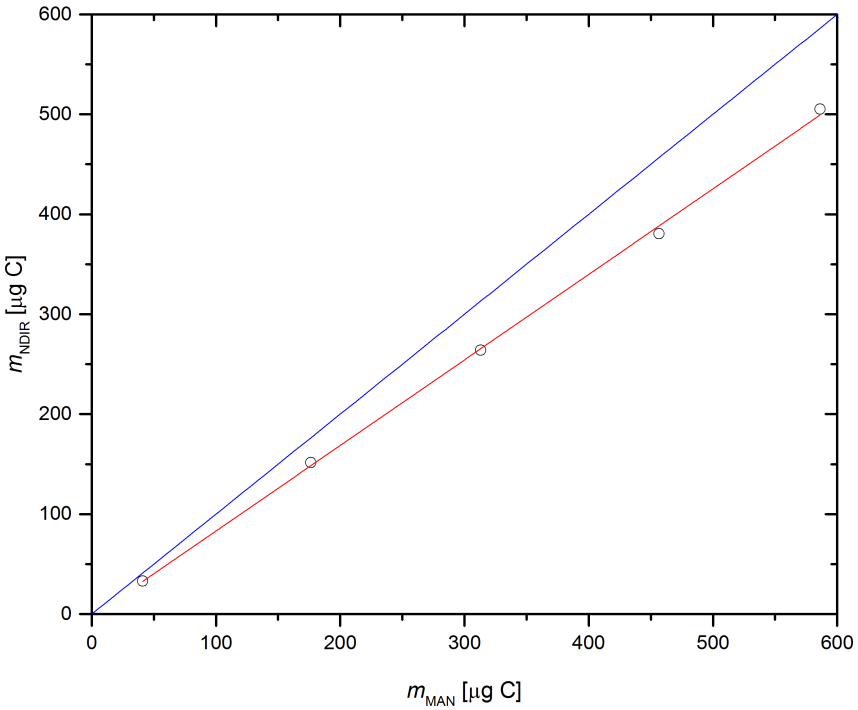

Figure C.4: Carbon mass of a CO_2 sample as measured with the manometry cell (m_{MAN}) versus as derived from NDIR CO_2 measurements (m_{NDIR}). The blue line would correspond to a perfect fit, the red line is a linear fit to the measurements (no uncertainty included).

in Fig. C.3. The setup was completely assembled for normal operation, the photo-reactor was filled with 300 ml UPW, acidified to pH 1.5, degassed and cleaned with UV irradiation. In a first step, the manometry cell was loaded with a CO_2 sample that was supplied from a CO_2 cylinder and the corresponding mass m_{MAN} was determined. Next, the CO_2 sample was transferred and frozen to the U-tube by cryogenic pumping. A helium carrier gas stream of 100 nccm was established through the getter oven, the U-tube with frozen CO_2 sample, the photo-reactor with UPW sample, the active water traps and the NDIR CO_2 detector. Then, the cryogenic bath was removed from the U-tube and the CO_2 sample was released and transported with the carrier gas stream as shown by the red, dashed line in Fig. C.3. The corresponding CO_2 concentration signal was recorded in the NDIR CO_2 detector. Since the flow-rate Q of the carrier gas was known, we could calculate the corresponding volume of CO_2 at standard temperature and pressure by the integration of the CO_2 concentration over time:

$$V(\mathrm{CO_2}) = Q \int C(\mathrm{CO_2})dt.$$

Finally, we derived the carbon mass m_{NDIR} from $V(\mathrm{CO_2})$ by the ideal gas law.

The measurements revealed that m_{MAN} does not equal m_{NDIR}, what would correspond to the blue line in Fig. C.4. Instead, a loss of $(15 \pm 2)\%$ of m_{MAN} was observed for m_{NDIR}. We assume that this loss is due to the nature of the flow-through measurement in the NDIR CO_2 detector. Moreover, since the CO_2 signal recorded by the NDIR CO_2 detector is related non-linearly to the carrier gas flow-rate, these results are only valid for a carrier gas flow-rate of 100 nccm.

However, the results showed good linearity and could be used for a calibration of the NDIR CO_2 detector. From a linear fit (red line in Fig. C.4) we derived the calibration for m_{NDIR}:

$$m_{\mathrm{MAN}} = 1.17 \cdot m_{\mathrm{NDIR}} + 3.3\,\mu\mathrm{g} \quad \text{for } Q = 100\,\mathrm{nccm}.$$

The mass m_{MAN} can be considered as the 'real' carbon mass of the measured CO_2 sample. No uncertainties are given for m_{NDIR}. For more accurate and non-destructive measurements, the manometry cell is used. However, for quick mass measurements with limited absolute accuracy, the NDIR CO_2 detector can be used.

Appendix D

Operation Manual

The operation manual for the extraction setup gives step-by-step instructions on every single action needed for successful and reproducible DOC extraction from ice samples. In addition to the general description of the setup (Sec. 2) and the conceptual explanation of the measurement procedure (Sec. 2.6), this manual is meant to be self-explanatory for the use of the extraction setup in the laboratory. Calibrations for the different components can be found in Sec. 3 and in App. C.

ice2C14 operation manual

extraction setup

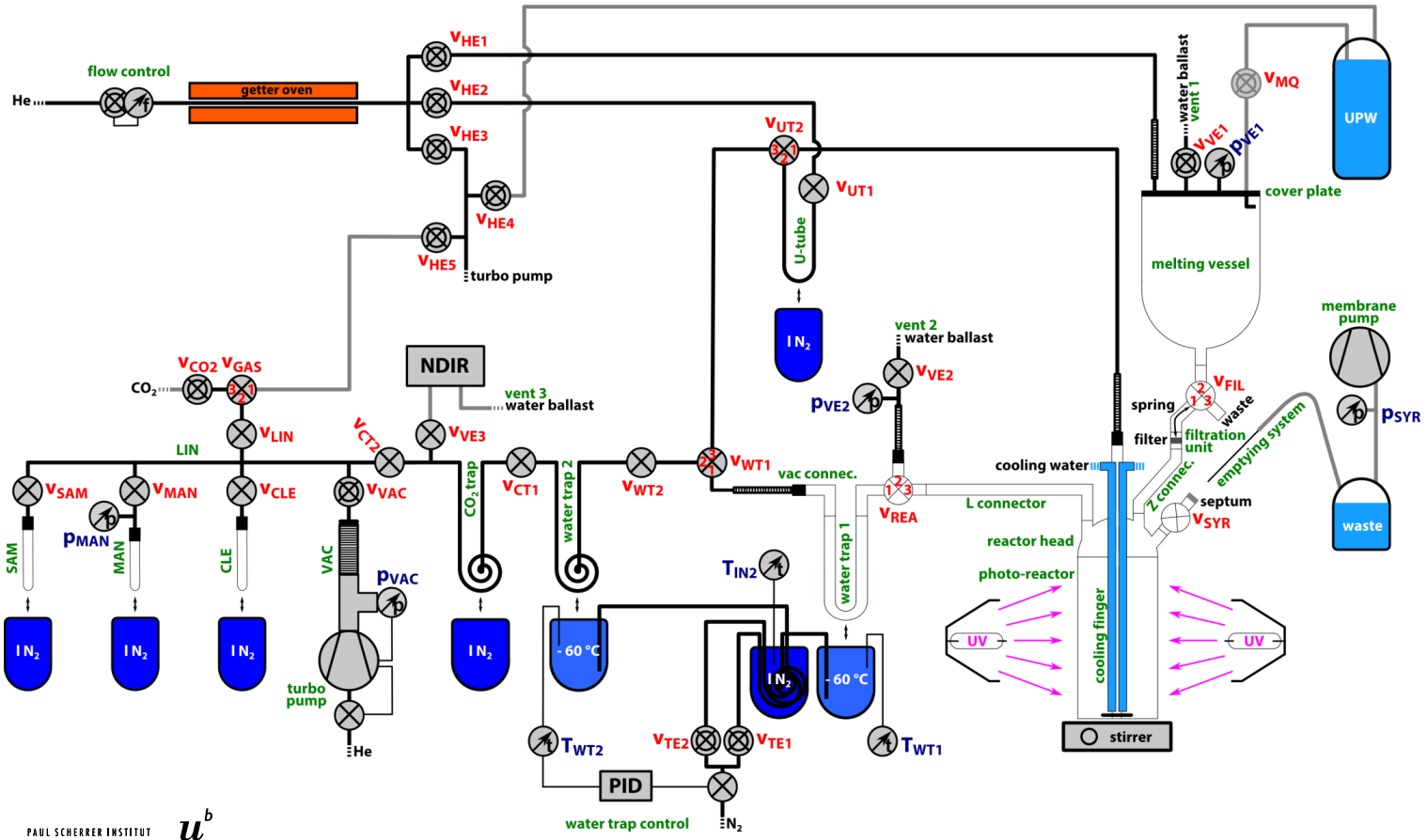

legend

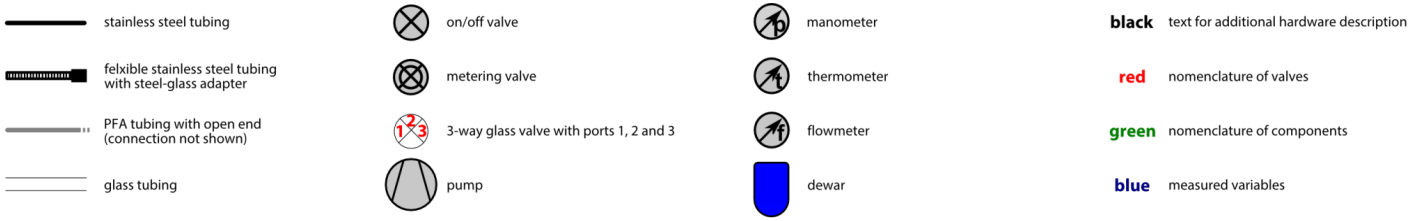

- process section 'x', working step 1, multiple single tasks are combined as […]
- process section 'x', working step 2 with link (↔ **x.1**) to other working step
- *italic type* refers to parts shown in the setup overview scheme in green and black text
- p_{XY} refers to the pressure displayed at manometer XY, T_{XY} refers to the temperature measured at thermometer XY
- 2-way valve settings: v_{XY} … valve XY is closed, v_{XY} … valve XY is open
- 3-way valve settings: v_{XY} … valve XY is closed to all ports, v_{XY}^{ij} … valve XY is open to ports i and j, v_{XY} … valve XY is open to all ports

ice sampling (#ice)

- cut ice sample in cold lab with bandsaw
- use Semadeni PETG sample container [cleaned by rinsing 3 times with UPW] for intermediate storage and sample transport to extraction setup
- temper in laminar flow box in container for 15 min, rinse with UPW from wash bottle, insert into *melting vessel* ↔ **m.1**

preparation (#p)

p.0

- prepare supply of UPW (wash bottles, UPW reservoir), pre-baked quartz fibre filters, liquid nitrogen, clean glass syringes with needles and sample containers / blank ice boxes

p.1

- fill lN_2 reservoir and install cryogenic baths for *water traps 1 and 2* and start *water trap control* at *PID* [nitrogen supply = ON, $p(N_2)$ = 2 bar]

p.2

- flush helium supply line [helium supply = ON, p(He) = 0.5 bar, *flow control* = ON + PURGE, *getter oven* = ON, v_{HE3} v_{HE5}, loosen connection to v_{GAS} and fix again after 1 min, v_{HE3} v_{HE5}]

p.3

- install ventilation to fume hood [fume hood = ON, flow box = ON]

p.4

- continuously monitor lN_2 reservoir fill level (T_{IN2} < -180°C?) and *water trap* temperatures T_{WT1} T_{WT2} (if needed, correct by dosing nitrogen flow with v_{TE1} v_{TE2})

p.5

- continuously monitor *water trap 1* gas flow (via p_{VE2}) and exchange *water trap 1* if needed

installation (#i)

i.1

- mount *melting vessel* with *cover plate* (with PFA O-ring), V_{FIL}, *filter holder* with quartz fibre *filter* and *spring*, *photo-reactor* with *stirrer*, *reactor head* (orientation: connection with drip nose for liquid sample at vessel holder fixation), *cooling finger*, *Z connector* at drip nose connection (connect reactor part and filtration part gently with the lifting platform and fix the platform), V_{SYR} at back connection (with *septum* at glass socket), *L connector*, V_{REA}^{23}, *water trap 1* (downstream leg filled with glass capillaries), *vac connector*

i.2

- connect vacuum line with *vac connector*, *vent 2* with V_{REA}^{23}, *cooling finger* with *cooling water* and V_{UT2}, insert *emptying system* through *septum* and V_{SYR} (syringe is connected to *waste* vessel and *membrane pump*)

cleaning (#c)

c.1

- fill the vacuum line with helium [v_{UT1} v_{HE5} v_{GAS}^{12} v_{LIN} v_{CT2} v_{CT1} v_{WT2} (all stepwise, avoiding negative pressure by monitoring helium flow-rate)], flush via *NDIR* [v_{VE3}, monitor *NDIR* signal drop to $C(CO_2)$ = 0 ppm (@ 100 nccm He flow) [*NDIR* = ON, connected to PC], v_{VE3}], flush for 2 min via *vent 2* [v_{WT1}^{12} v_{REA}]

c.2

- flush the glass setup with helium via the *cooling finger*: first for 5 min via *vent 2* [v_{WT1} v_{GAS} v_{CT2} v_{LIN} v_{VAC} , v_{HE2} v_{UT1} v_{UT2}^{12} v_{REA} v_{VE2}, *flow control* = PURGE] then for 5 min via *vent 1* [v_{FIL} v_{VE1} v_{VE2}]

c.3

- prepare rinsing [v_{UT1} v_{FIL} v_{VE2} v_{VE1}], fill *melting vessel* with UPW to 12 cm level below vessel holder (≈ 300 ml) [v_{HE3} v_{HE4} v_{MQ}] and rinse to *photo-reactor* [v_{MQ} v_{VE2} v_{HE1} v_{FIL}^{12}] by dosing p_{VE1} with v_{VE1} for a little overpressure at *melting vessel*, [v_{FIL} v_{HE1}] and measure fill level of cleaning sample in *photo-reactor*

c.4

- flush *photo-reactor* with helium via *vent 2* [v_{HE3} v_{UT1}, *flow control* = 100 nccm] and add 5 ml H_3PO_4 (85%) (pH < 1.5) with glass syringe through *septum* and v_{SYR} , remove glass syringe afterwards, magnetic *stirrer* = ON

c.5

- oxidise *photo-reactor* content [*cooling water* = ON, ventilation = ON, close reactor casing, attach shielding cloth, *UV lamps* = ON]

c.6

- check operation of *water traps* (T = -60°C), direct helium flow via *vent 3* [v_{VE2} v_{WT1}^{12} v_{VE3}] and monitor *NDIR* signal drop to $C(CO_2)$ < 1 ppm (@ 100nccm), **↔ m.5**

melting (#m)

m.1

- disassemble *melting vessel* [remove *cover plate* and loosen connection to v_{FIL}], insert ice sample (↔ **ice.3**) and assemble again

m.2

- flush *melting vessel* with helium [v_{HE1} v_{VE1}, *flow control* = PURGE], dose with v_{HE1} and v_{HE2} for a simultaneous helium flow through *vent 3* (oxidation monitoring via *NDIR* ↔ **c.6**) and *vent 1*

m.3

- flood *melting vessel* with UPW [v_{HE3} v_{MQ}] until sample floats [v_{MQ}], and dispose washing water to *waste* [v_{FIL}^{23}]

m.4

- melt cleaned ice sample [v_{FIL}, *IR lamp* = ON, hot air gun = ON] ↔ **f.1**

m.5

- ↔ **c.6** when cleaning oxidation finished (*NDIR* signal drop to $C(CO_2) < 1$ ppm (@ 100 nccm)), empty *photo-reactor* with *abstraction system* except for 50 ml (2.5 cm fill level, resulting pH < 2) (or more if sample small) [*membrane pump* = ON, when fill level reached: *membrane pump* = OFF and vent waste vessel to avoid negative pressure in *photo-reactor*], remove *emptying system*, v_{SYR}

m.6

- end cleaning oxidation ↔ **c.6** [*UV lamps* = OFF, open reactor casing, open shielding cloth], direct helium flow via *vent 2* [v_{WT1} v_{VE3} v_{REA}^{23} v_{VE2}] empty waste vessel, measure fill level of acidifier in *photo-reactor*

filtration and degassing (#f)

f.1

- after sample melting (↔ **m.4**) finished [hot air gun = OFF, IR lamp = OFF], check estimated sample volume* and transfer sample via *filter* to *photo-reactor* [v_{FIL}^{12}] by dosing p_{VE1} with v_{VE1} for a little overpressure at *melting vessel* (p_{VE1} ≈ 0.1 bar), measure fill level of sample in *photo-reactor*

f.2

- check operation of *water traps* (T_{WT1} , T_{WT2} = -60°C) and degas liquid sample in *photo-reactor* via *vent 3* [v_{FIL} v_{HE1} v_{VE1}, *flow control* = 100 nccm, v_{VE2} v_{REA} v_{WT1}^{12} v_{VE3}], monitor *NDIR* signal drop to C(CO_2) < 1 ppm (@ 100 nccm)

* check estimated sample volume vs. reactor volume by measuring fill level of *melting vessel* from below vessel holder, 350 ml in total = max. reactor volume)

melting vessel fill level	sample volume
12.6 cm	250 ml
12.0 cm	300 ml
11.4 cm	350 ml
10.8 cm	400 ml

oxidation (#o)

o.1

- close reactor casing and shielding cloth, install dewar with lN_2 at *CO_2 trap* [v_{VE3}, increase lN_2 level at trap with lifting platform, v_{VE3} when p_{VE2} > atmospheric pressure]

o.2

- check C(CO_2) drop to 0 ppm at *NDIR*, *UV lamps* = ON for 45 min, ensure stable lN_2 level at *CO_2 trap*

o.3

- oxidation finished [*UV lamps* = OFF], wait 2 min and direct helium flow via *vent 2* [v_{VE3} v_{CT1} v_{WT2} v_{WT1} v_{REA} ^{23} v_{VE2}, *magnetic stirrer* = OFF]

sampling (#s)

s.1

- evacuate *CO_2 trap* [v_{CT2}, open v_{VAC} carefully (*turbo pump* load)] until p_{VAC} < E-6 mbar [v_{CT2} v_{CLE} v_{MAN}]

s.2

- remove lN_2 bath from *CO_2 trap* and thaw *CO_2 trap* with water bath

s.3

- transfer sample to *CLE* [v_{VAC}, install lN_2 bath at *CLE*, v_{CT2}, wait for 5 min starting from p_{MAN} = LO and increase lN_2 level in the last minute, v_{CLE} v_{CT2}]

s.4

- clean sample from volatile compounds [v_{VAC} v_{VAC} v_{VAC} v_{VAC} iteratively until p_{VAC} < E-6 mbar]

s.5

- clean sample from water [v_{CLE}, remove lN_2 bath from *CLE*, thaw *CLE* with water bath, install EtOH slush bath (T = -70°C) at *CLE*, v_{MAN}, install lN_2 bath at *MAN*, wait for 2 min] and transfer sample to *MAN* [v_{VAC} v_{CLE} v_{MAN}, wait for 2 min and increase lN_2 level at the end, v_{CLE} v_{MAN}]

s.6

- remove lN_2 bath from *MAN*, thaw *MAN* with water bath, remove EtOH slush bath, measure p_{MAN}

s.7

- prepare *SAM* [v_{VAC} v_{SAM} v_{VAC}, mark 65 mm tube length at *SAM* glass tube, install lN_2 bath at *SAM*] and transfer sample to *SAM* [v_{MAN}, wait 2 min and increase lN_2 level at the end], seal glass tube at the marking with gas burner, do a leak test [remove lN_2 bath from *SAM*, thaw *SAM* with water bath, check if p_{MAN} = LO], seal off glass tube with gas burner and label it for GIS MICADAS measurement

next sample (#n)

n.1

- remove used *water trap 1* [V_{WT1} V_{REA}^{23}] and install fresh *water trap 1* with glass capillary filling, defrost *water trap 2* and evacuate *water trap 2* and the vacuum line [V_{CLE} V_{CT2} V_{CT1} V_{WT2} V_{VAC}], close vacuum line before step c.1 [V_{SAM} V_{MAN} V_{CLE} V_{CT2} V_{CT1} V_{WT2} V_{VAC}]

n.2

- insert *emptying system* via *septum* [V_{SYR}] and empty *photo-reactor* [V_{REA}^{23} V_{VE2} V_{FIL}, *membrane pump* = ON, when empty: *membrane pump* = OFF and vent *waste vessel* to avoid negative pressure in *photo-reactor*, V_{UT1}]

n.3

- dismantle *filter holder*, rinse *Z connector* to *photo-reactor* with UPW (wash bottle) and close it temporarily with glass stopper, remove *filter*, rinse *spring* and *filter holder* with UPW (wash bottle), briefly dry *filter holder* in oven (50°C, for dry joints), remove *cover plate* from *melting vessel* and rinse *melting vessel* [first V_{FIL}^{12} then V_{FIL}^{23}] with UPW (wash bottle) to waste container, mount *cover plate* again, mount *filter holder* with *spring* and fresh quartz *filter*

n.4

- empty *photo-reactor* [V_{REA}^{23} V_{VE2} V_{FIL} V_{UT1}, *membrane pump* = ON, when empty: *membrane pump* = OFF and vent *waste vessel* to avoid negative pressure in *photo-reactor*]

c.1

- continue with ↔ **c.1**

end (#e)

- turn OFF gas supplies: helium, nitrogen, propane, oxygen
- turn OFF *getter oven*, *flow control* = CLOSED
- stop *cooling water*, turn OFF ventilation and remove ventilation from hood, open reactor casing, remove shielding cloth
- turn OFF power supply for (p_{MAN}, *flow control*, *getter oven* control) and for (ventilation, *UV lamps*, *water trap control*)
- stop *NDIR* logging and turn OFF *NDIR,* turn OFF all three multimeter
- remove cryogenic baths of *water traps*
- close supply valves [V_{HE1} V_{HE2} V_{HE3} V_{HE4} V_{HE5} V_{UT1} V_{UT2} V_{VE1} V_{VE2} V_{WT1}] and open vacuum line valves [V_{SAM} V_{MAN} V_{CLE} V_{CT2} V_{CT1} V_{WT2}, open V_{VAC} carefully (*turbo pump* load)]
- if setup is not reused: disconnect [*cooling water*, V_{UT2}, *cover plate*, *emptying system*, V_{VE2}, V_{WT1}] and disassemble glass setup [*vac connector, water trap 1,* V_{REA}, *L connector, cooling finger,* V_{SYR}, *Z connector, filter holder* with *spring, reactor head, photo-reactor* with *stirrer,* V_{FIL}, *melting vessel*], store *cooling finger* and syringe of *emptying system* in UPW bath, clean all other parts [Deconex bath overnight, thorough rinsing with UPW, drying in oven at 50°C]

Appendix E

MICADAS Measurement Data

This section summarizes the results of all successful ^{14}C measurements with the MICADAS at the LARA, Bern. The following table is a compilation of:

- The individual **name** of each ^{14}C sample. All samples contain the prefix 'ice2C14_'.
- Information on the origin of the ^{14}C **sample**.
- The **Bern number** is the internal number of LARA given to each sample measured with the MICADAS.
- **Type** specifies the state of the ^{14}C sample for the measurement. 'G' denotes graphitised CO_2 samples. 'A' denotes gaseous CO_2 samples that were sealed in an ampoule. 'F' denotes samples on a quartz fibre filter that were combusted in a Sunset OC/EC Analyser to deliver CO_2. Furthermore, for filter samples, the used temperature protocol that corresponds to the analysed carbon fraction is indicated as 'TC' (total carbon) or 'OC' (organic carbon).
- The carbon **mass** given in μg C with its respective error. For graphite samples (G) no mass was determined. For ampoule samples (A) the mass was measured beforehand in the manometry cell. For filter samples (F) the mass was measured in the Sunset OC/ EC Analyser.
- The fraction modern $\boldsymbol{F^{14}C}$ with its respective absolute error. $F^{14}C$ is the direct result of the MICADAS ^{14}C measurement and has automatically been corrected for the ^{14}C analysis itself with the help of internal standards and blanks. For filter samples (F), the given $F^{14}C$ value has furthermore been corrected for the combustion step in the

Sunset OC/EC Analyser [Agrios et al., 2015]. However, the $F^{14}C$ values are not yet blank corrected for effects from the extraction method ('POC blank', 'DOC blank').

- The **use** for each set of measurements is given with the respective reference in this work.

name 'ice2C14_'	**sample**	**Bern number**	**type**	**mass (μg C)**	**$\pm$ (μg C)**	**F^{14}C**	**$\pm$ (abs)**	**use**
cal03	CO_2	3304.1.1	G	-	-	0.0026	0.0001	calibration gas (see Sec. 3.3.1)
		3304.1.2	G	-	-	0.0022	0.0001	
cal04	CO_2 (664 μg)	3300.1.1	A	43.6	1.1	0.0043	0.0014	CO_2 sample processing blank (see Sec. 3.3.1)
cal05	CO_2 (1452 μg)	3301.1.1	A	95.6	2.3	0.0021	0.0014	
cal06	CO_2 (433 μg)	3302.1.1	A	29.8	0.7	0.0016	0.0013	
cal07	CO_2 (441 μg)	3303.1.1	A	29.9	0.7	0.0022	0.0013	
cal08	H_2O (300 ml)	4287.1.1	A	27.1	0.7	0.2852	0.0059	oxidation blank (see Sec. 3.3.2)
cal09	OXA fossil (0.525 g)	4288.1.1	A	22.5	0.5	0.0923	0.0036	
cal10	OXA fossil (0.508 g)	4289.1.1	A	19.9	0.5	0.0500	0.0027	
cal11	OXA fossil (0.250 g)	4290.1.1	A	10.0	0.3	0.1189	0.0041	
cal12	OXA modern (0.499 g)	4291.1.1	A	16.9	0.4	1.2796	0.0153	
cal13	UPW (325 ml)	4292.1.1	A	8.0	0.2	0.6345	0.0105	
cal14	OXA modern (0.729 g)	4293.1.1	A	27.6	0.7	1.2031	0.0166	
cal15	OXA modern (0.572 g)	4294.1.1	A	20.1	0.5	1.2779	0.0152	
cal16	OXA modern (0.527 g)	4295.1.1	A	17.9	0.4	1.2459	0.0150	
cal17	OXA fossil (0.555 g)	4296.1.1	A	22.8	0.6	0.0699	0.0030	
cal18	OXA half-modern (0.610 g)	4297.1.1	A	26.5	0.6	0.5068	0.0083	
cal19	OXA half-modern (0.489 g)	4298.1.1	A	20.5	0.5	0.4946	0.0113	
cal20	pre-oxidised UPW (307 ml)	4652.1.1	A	3.1	0.1	0.6570	0.0359	
cal21	OXA fossil (1.085 g)	4747.1.1	A	43.7	1.1	0.0449	0.0033	oxidation blank (see Sec. 3.3.2)
cal22A	OXA fossil (4.471 g)	4748.1.1	A	103.4	2.5	0.0147	0.0020	
cal22B		4749.1.1	A	50.8	1.2	0.0122	0.0025	
cal24	OXA fossil (3.237 g)	4751.1.1	A	105.4	2.5	0.0177	0.0025	
cal25	OXA fossil (0.200 g)	4752.1.1	A	9.3	0.2	0.1388	0.0088	

name 'ice2C14_'	**sample**	**Bern number**	**type**	**mass (μg C)**	**$\pm$ (μg C)**	**F^{14}C**	**$\pm$ (abs)**	**use**
cal27	UPW (329 ml, 'TOT_1-liq')	5026.1.1	A	9.8	0.2	0.9215	0.0144	overall DOC blank (see Sec. 3.3.3)
cal30	H_2O (280 ml, 'TOT_4-liq')	5029.1.1	A	19.3	0.5	0.7312	0.0156	
cal32	UPI (340 ml, 'TOT_2-ice')	5031.1.1	A	7.5	0.2	0.8539	0.0134	
cal33	UPI (305 ml, 'TOT_3-ice')	5032.1.1	A	4.3	0.1	0.6366	0.0174	
cal34	ice (276 ml, 'TOT_4-ice')	5033.1.1	A	1.6	0.1	0.6909	0.0463	
cal35	UPI (240 ml, 'mQice-1')	5475.1.1	A	4.3	0.1	0.6150	0.0180	overall DOC blank (see Sec. 3.3.3)
cal36	UPI (186 ml, 'mQice-8')	5476.1.1	A	3.0	0.1	0.7171	0.0279	
cal39	UPI (309 ml, 'mQice-7')	5477.1.1	A	3.2	0.1	0.6621	0.0306	
cal40	UPI (267 ml, 'mQice-6')	5478.1.1	A	3.5	0.1	0.6340	0.0560	
juv1.4	Juvfonne block 1 (158 ml)	5481.1.1	A	20.0	0.5	0.5629	0.0063	Juvfonne ice tunnel DOC (see Sec. 4.3)
juv3.3	Juvfonne block 3 (147 ml)	5484.1.1	A	18.8	0.5	0.4900	0.0057	
juv3.4	Juvfonne block 3 (139 ml)	5483.1.1	A	45.1	1.1	0.4665	0.0055	
juv5.3	Juvfonne block 5 (164 ml)	5482.1.1	A	41.7	1.0	0.5311	0.0098	
cal35-POC	3 filters ('mQice-(1,2,3)')	5268.1.1	F, TC	2.8	0.2	0.6296	0.0771	POC* blank (see Sec. 3.3.4)
cal36-POC	2 filters ('mQice-(4,8)')	5269.1.1	F, TC	3.5	0.2	0.6404	0.0583	
cal40-POC	2 filters ('mQice-(5,6)')	5468.1.1	F, TC	2.5	0.3	0.7232	0.0849	
juv1.3	Juvfonne block 1 (226 ml)	5469.1.1	F, OC	7.7	0.6	0.4865	0.0234	Juvfonne ice tunnel POC* (see Sec. 4.2)
juv1.4	Juvfonne block 1 (158 ml)	5470.1.1	F, OC	23.4	1.4	0.4829	0.0091	
juv3.3	Juvfonne block 3 (147 ml)	5471.1.1	F, OC	16.4	1.0	0.4514	0.0107	
juv3.4	Juvfonne block 3 (139 ml)	5472.1.1	F, OC	92.2	4.8	0.4120	0.0062	
juv5.3	Juvfonne block 5 (164 ml)	5473.1.1	F, OC	21.0	1.3	0.4695	0.0089	
juv5.4	Juvfonne block 5 (194 ml)	5474.1.1	F, OC	135.3	7.0	0.4263	0.0074	

Bibliography

Agrios, K., Salazar, G., Zhang, Y.-L., Uglietti, C., Battaglia, M., Luginbühl, M., Ciobanu, V. G., Vonwiller, M., and Szidat, S. (2015). Online coupling of pure O_2 thermo-optical methods - ^{14}C AMS for source apportionment of carbonaceous aerosols. *Nuclear Instruments and Methods in Physics Research Section B*, 361:288–293.

Armstrong, F. J., Williams, P. M., and Strickland, J. D. H. (1966). Photo-oxidation of Organic Matter in Sea Water by Ultra-violet Radiation, Analytical and Other Applications. *Nature*, 211:481–483.

Barbante, C., Schwikowski, M., Döring, T., Gäggeler, H. W., Schotterer, U., Tobler, L., Van de Velde, K., Ferrari, C., Cozzi, G., Turetta, A., Rosman, K., Bolshov, M., Capodaglio, G., Cescon, P., and Boutron, C. (2004). Historical Record of European Emissions of Heavy Metals to the Atmosphere Since the 1650s from Alpine Snow/Ice Cores Drilled near Monte Rosa. *Environmental Science and Technology*, 38(15):4085–4090.

Bauer, J. E., Druffel, E. R. M., Williams, P. M., Wolgast, D. M., and Griffin, S. (1998). Temporal variability in dissolved organic carbon and radiocarbon in the eastern North Pacific Ocean. *Journal of Geophysical Research*, 103(C2):2867–2881.

Beaupré, S. R. and Druffel, E. R. M. (2012). Photochemical reactivity of ancient marine dissolved organic carbon. *Geophysical Research Letters*, 39(18):L18602.

Beaupré, S. R., Druffel, E. R. M., and Griffin, S. (2007). A low-blank photochemical extraction system for concentration and isotopic analyses of marine dissolved organic carbon. *Limnology and Oceanography: Methods*, 5:174–184.

Bennett, C. L., Beuckens, R. P., Clover, M. R., Gove, H. E., Liebert, R. B., Litherland, A. E., Purser, K. H., and Sondheim, W. E. (1977). Radiocar-

bon Dating Using Electrostatic Accelerators: Negative Ions Provide the Key. *Science*, 198(4316):508–510.

Bond, T. C., Doherty, S. J., Fahey, D. W., Forster, P. M., Berntsen, T., DeAngelo, B. J., Flanner, M. G., Ghan, S., Kärcher, B., Koch, D., Kinne, S., Kondo, Y., Quinn, P. K., Sarofim, M. C., Schultz, M. G., Schulz, M., Venkataraman, C., Zhang, H., Zhang, S., Bellouin, N., Guttikunda, S. K., Hopke, P. K., Jacobson, M. Z., Kaiser, J. W., Klimont, Z., Lohmann, U., Schwarz, J. P., Shindell, D., Storelvmo, T., Warren, S. G., and Zender, C. S. (2013). Bounding the role of black carbon in the climate system: A scientific assessment. *Journal of Geophysical Research: Atmospheres*, 118:5380–5552.

Bronk Ramsey, C. and Lee, S. (2013). Recent and Planned Developments of the Program OxCal. *Radiocarbon*, 55(23).

Cao, F., Zhang, Y.-L., Szidat, S., Zapf, A., Wacker, L., and Schwikowski, M. (2013). Microgram-Level Radiocarbon Determination of Carbonaceous Particles in Firn and Ice Samples: Pretreatment and OC/EC Separation. *Radiocarbon*, 55(34).

Cogley, J., Hock, R., Rasmussen, L. A., Arendt, A. A., Bauder, A., Braithwaite, R. J., Jansson, P., Kaser, G., Möller, M., Nicholson, L., and Zemp, M. (2011). Glossary of Glacier Mass Balance and Related Terms. Internal Report IHP-VII Technical Documents in Hydrology No. 86, IACS Contribution No. 2, UNESCO-IHP, Paris.

Crozaz, G. and Langway, C. C. (1966). Dating Greenland firn-ice cores with Pb-210. *Earth and Planetary Science Letters*, 1(4):194–196.

Demtröder, W., editor (2009). *Experimentalphysik 4: Kern-, Teilchen- und Astrophysik*. Springer-Verlag GmbH, Berlin, 3th edition.

Demtröder, W., editor (2012). *Experimentalphysik 1 - Mechanik und Wärme*. Springer-Verlag GmbH, Berlin, 6th edition.

Druffel, E. R. M., Griffin, S., Walker, B. D., Coppola, A. I., and Glynn, D. S. (2013). Total Uncertainty of Radiocarbon Measurements of Marine Dissolved Organic Carbon and Methodological Recommendations. *Radiocarbon*, 55(34).

Duursma, E. K. (1961). Dissolved organic carbon, nitrogen and phosphorus in the sea. *Netherlands Journal of Sea Research*, 1(1):1–141.

Eichler, A., Gramlich, G., Kellerhals, T., Tobler, L., and Schwikowski, M. (2015). Pb pollution from leaded gasoline in South America in the context of a 2000-year metallurgical history. *Science Advances*, 1(2):e1400196.

Eichler, A., Schwikowski, M., and Gäggeler, H. W. (2001). Meltwater-induced relocation of chemical species in Alpine firn. *Tellus B*, 53(2):192–203.

Eichler, A., Schwikowski, M., Gäggeler, H. W., Furrer, V., Synal, H.-A., Beer, J., Saurer, M., and Funk, M. (2000). Glaciochemical dating of an ice core from upper Grenzgletscher (4200 m a.s.l.). *Journal of Glaciology*, 46(154):507–515.

EMD Millipore Corp. (2013). *Milli-Q Direct Water Purification System*. Merck KGaA, Darmstadt, Germany.

Espe, W., Knoll, M., and P., W. M. (1950). Getter Materials. *Electronics*, 1(1):80–86.

Federer, U., Kaufmann, P. R., Hutterli, M. A., Schüpbach, S., and Stocker, T. F. (2008). Continuous Flow Analysis of Total Organic Carbon in Polar Ice Cores. *Environmental Science and Technology*, 42(21):8039–8043.

Fischer, H., Severinghaus, J., Brook, E., Wolff, E., Albert, M., Alemany, O., Arthern, R., Bentley, C., Blankenship, D., Chappellaz, J., Creyts, T., Dahl-Jensen, D., Dinn, M., Frezzotti, M., Fujita, S., Gallee, H., Hindmarsh, R., Hudspeth, D., Jugie, G., Kawamura, K., Lipenkov, V., Miller, H., Mulvaney, R., Parrenin, F., Pattyn, F., Ritz, C., Schwander, J., Steinhage, D., van Ommen, T., and Wilhelms, F. (2013). Where to find 1.5 million yr old ice for the IPICS "Oldest-Ice" ice core. *Climate of the Past*, 9(6):2489–2505.

Fry, B., Peltzer, E. T., Hopkinson, C. S., Nolin, A., and Redmond, L. (1996). Analysis of marine DOC using a dry combustion method. *Marine Chemistry*, 54(34):191–201.

Gäggeler, H., von Gunten, H. R., Rössler, E., Oeschger, H., and Schotterer, U. (1983). ^{210}Pb-Dating of Cold Alpine Firn/Ice Cores From Colle Gnifetti, Switzerland. *Journal of Glaciology*, 29(101):165–177.

Gelencsér, A., May, B., Simpson, D., Sánchez-Ochoa, A., Kasper-Giebl, A., Puxbaum, H., Caseiro, A., Pio, C., and Legrand, M. (2007). Source apportionment of PM2.5 organic aerosol over Europe: Primary/secondary,

natural/anthropogenic, and fossil/biogenic origin. *Journal of Geophysical Research: Atmospheres*, 112.

Ginot, P., Stampfli, F., Stampfli, D., Schwikowski, M., and Gäggeler, H. W. (2002). FELICS, a new ice core drilling system for high-altitude glaciers. *Memoirs of National Institute of Polar Research. Special issue*, 56:38–48.

Golimowski, J. and Golimowska, K. (1996). UV-photooxidation as pretreatment step in inorganic analysis of environmental samples. *Analytica Chimica Acta*, 325(3):111–133.

Grannas, A. M., Jones, A. E., Dibb, J., Ammann, M., Anastasio, C., Beine, H. J., Bergin, M., Bottenheim, J., Boxe, C. S., Carver, G., Chen, G., Crawford, J. H., Dominé, F., Frey, M. M., Guzmán, M. I., Heard, D. E., Helmig, D., Hoffmann, M. R., Honrath, R. E., Huey, L. G., Hutterli, M., Jacobi, H. W., Klán, P., Lefer, B., McConnell, J., Plane, J., Sander, R., Savarino, J., Shepson, P. B., Simpson, W. R., Sodeau, J. R., von Glasow, R., Weller, R., Wolff, E. W., and Zhu, T. (2007). An overview of snow photochemistry: evidence, mechanisms and impacts. *Atmospheric Chemistry and Physics*, 7(16):4329–4373.

Hagler, G. S. W., Bergin, M. H., Smith, E. A., Dibb, J. E., Anderson, C., and Steig, E. J. (2007). Particulate and water-soluble carbon measured in recent snow at Summit, Greenland. *Geophysical Research Letters*, 34(L16505).

Heraeus Noblelight GmbH (2012). *Technical Data MH-Module 250W XL*. Heraeusstrasse 12 - 14, D-63450 Hanau, Germany.

Hoffmann, H. M. (2016). *Micro radiocarbon dating of the particulate organic carbon fraction in Alpine glacier ice: method refinement, critical evaluation and dating applications*. PhD thesis, University of Heidelberg.

Hood, E., Battin, T. J., Fellman, J., O'Neel, S., and Spencer, R. G. M. (2015). Storage and release of organic carbon from glaciers and ice sheets. *Nature Geoscience*, 8(2):91–96.

Ionplus AG (2015). Mini Carbon Dating System - MICADAS. Technical report.

Jenk, T. M., Szidat, S., Bolius, D., Sigl, M., Gäggeler, H. W., Wacker, L., Ruff, M., Barbante, C., Boutron, C. F., and Schwikowski, M. (2009). A novel radiocarbon dating technique applied to an ice core from the

Alps indicating late Pleistocene ages. *Journal of Geophysical Research*, 114(D14305).

Jenk, T. M., Szidat, S., Schwikowski, M., Gäggeler, H. W., Brütsch, S., Wacker, L., Synal, H.-A., and Saurer, M. (2006). Radiocarbon analysis in an Alpine ice core: record of anthropogenic and biogenic contributions to carbonaceous aerosols in the past ($1650 - 1940$). *Atmospheric Chemistry and Physics*, 6(12):5381–5390.

Jenk, T. M., Szidat, S., Schwikowski, M., Gäggeler, H. W., Wacker, L., Synal, H.-A., and Saurer, M. (2007). Microgram level radiocarbon (^{14}C) determination on carbonaceous particles in ice. *Nuclear Instruments and Methods in Physics Research Section B*, 259(1):518–525.

Jouzel, J. (2013). A brief history of ice core science over the last 50 yr. *Climate of the Past*, 9(6):2525–2547.

Knüsel, S., Ginot, P., Schotterer, U., Schwikowski, M., Gäggeler, H. W., Francou, B., Petit, J. R., Simões, J. C., and Taupin, J. D. (2003). Dating of two nearby ice cores from the Illimani, Bolivia. *Journal of Geophysical Research: Atmospheres*, 108:4181.

Lal, D. and Jull, A. J. T. (1990). On determining ice accumulation rates in the past 40,000 years using in situ cosmogenic ^{14}C. *Geophysical Research Letters*, 17(9):1303–1306.

Lal, D., Nishiizumi, K., and Arnold, R. (1987). In Situ Cosmogenic ^{3}H, ^{14}C, and ^{10}Be for Determining the Net Accumulation and Ablation Rates of Ice Sheets. *Journal of Geophysical Research*, 92(B6):4947–4952.

Lambert, F., Delmonte, B., Petit, J. R., Bigler, M., Kaufmann, P. R., Hutterli, M. A., Stocker, T. F., Ruth, U., Steffensen, J. P., and Maggi, V. (2008). Dust-climate couplings over the past 800,000 years from the EPICA Dome C ice core. *Nature*, 452(7187):616–619.

Lang, S., Bernasconi, S., and Früh-Green, G. (2012). Stable Isotope Analysis of Organic Carbon in Small (μg C) Samples and Dissolved Organic Matter Using a GasBench Preparation Device. *Rapid Communications in Mass Spectrometry*, 26:9–16.

Lang, S. Q., Lilley, M. D., and Hedges, J. I. (2007). A method to measure the isotopic (^{13}C) composition of dissolved organic carbon using a high temperature combustion instrument. *Marine Chemistry*, 103(34):318–326.

Lavanchy, V. M. H., Gäggeler, H. W., Schotterer, U., Schwikowski, M., and Baltensperger, U. (1999). Historical record of carbonaceous particle concentrations from a European high-alpine glacier (Colle Gnifetti, Switzerland). *Journal of Geophysical Research*, 104(D17):21,227–21,236.

le Clercq, M., van der Plicht, J., and Meijer, H. A. J. (1998). A supercritical oxidation system for the determination of carbon isotope ratios in marine dissolved organic carbon. *Analytica Chimica Acta*, 370(1):19–27.

Legrand, M., McConnell, J., Fischer, H., Wolff, E. W., Preunkert, S., Arienzo, M., Chellman, N., Leuenberger, D., Maselli, O., Place, P., Sigl, M., Schüpbach, S., and Flannigan, M. (2016). Boreal fire records in Northern Hemisphere ice cores: a review. *Climate of the Past*, 12(10):2033–2059.

Legrand, M., Preunkert, S., Jourdain, B., Guilhermet, J., Faïn, X., Alekhina, I., and Petit, J. R. (2013a). Water-soluble organic carbon in snow and ice deposited at Alpine, Greenland, and Antarctic sites: a critical review of available data and their atmospheric relevance. *Climate of the Past*, 9(5):2195–2211.

Legrand, M., Preunkert, S., May, B., Guilhermet, J., Hoffman, H., and Wagenbach, D. (2013b). Major 20th century changes of the content and chemical speciation of organic carbon archived in Alpine ice cores: Implications for the long-term change of organic aerosol over Europe. *Journal of Geophysical Research: Atmospheres*, 118:3879–3890.

Legrand, M., Preunkert, S., Schock, M., Cerqueira, M., Kasper-Giebl, A., Afonso, J., Pio, C., Gelencsér, A., and Dombrowski-Etchevers, I. (2007). Major 20th century changes of carbonaceous aerosol components (EC, WinOC, DOC, HULIS, carboxylic acids, and cellulose) derived from Alpine ice cores. *Journal of Geophysical Research*, 112(D23S11).

Libby, W. F., Anderson, E. C., and Arnold, J. R. (1949). Age Determination by Radiocarbon Content: World-Wide Assay of Natural Radiocarbon. *Science*, 109(2827):227–228.

Loh, A. N., Bauer, J. E., and Druffel, E. R. M. (2004). Variable ageing and storage of dissolved organic components in the open ocean. *Nature*, 430(7002):877–881.

Lüthi, M. P. and Funk, M. (2001). Modelling heat flow in a cold, high-altitude glacier: interpretation of measurements from Colle Gnifetti, Swiss Alps. *Journal of Glaciology*, 47(157):314–324.

Masarik, J. and Beer, J. (1999). Simulation of particle fluxes and cosmogenic nuclide production in the Earth's atmosphere. *Journal of Geophysical Research: Atmospheres*, 104:12,099–12,111.

Maupetit, F. and Delmas, R. J. (1994). Carboxylic acids in high-elevation Alpine glacier snow. *Journal of Geophysical Research: Atmospheres*, 99:16491–16500.

May, B. (2009). *Radiocarbon microanalysis on ice impurities for dating of Alpine glaciers*. Dissertation, University of Heidelberg.

May, B., Wagenbach, D., Hoffmann, H., Legrand, M., Preunkert, S., and Steier, P. (2013). Constraints on the major sources of dissolved organic carbon in alpine ice cores from radiocarbon analysis over the bomb-peak period. *Journal of Geophysical Research: Atmospheres*, 118:1–9.

Menzel, D. W. and Vaccaro, R. F. (1964). The Measurement of Dissolved Organic and Particulate Carbon in Seawater. *Limnology and Oceanography*, 9(1):138–142.

Müller, J. (1984). Atmospheric residence time of carbonaceous particles and particulate pah-compounds. *Science of The Total Environment*, 36:339–346.

Müller-Tautges, C., Eichler, A., Schwikowski, M., Pezzatti, G. B., Conedera, M., and Hoffmann, T. (2016). Historic records of organic aerosols from a high Alpine glacier: implications of biomass burning, anthropogenic emissions, and dust transport. *Atmospheric Chemistry and Physics*, 16:1029–1043.

Nelson, D. E., Korteling, R. G., and Stott, W. R. (1977). Carbon-14: Direct Detection at Natural Concentrations. *Science*, 198(4316):507–508.

Nesje, A., Pilø, L. H., Finstad, E., Solli, B., Wangen, V., Ødegård, R. S., Isaksen, K., Støren, E. N., Bakke, D. I., and Andreassen, L. M. (2012). The climatic significance of artefacts related to prehistoric reindeer hunting exposed at melting ice patches in southern Norway. *The Holocene*, 22(4):485–496.

Ødegård, R. S., Nesje, A., Isaksen, K., Andreassen, L. M., Eiken, T., Schwikowski, M., and Uglietti, C. (2017). Climate change threatens archeologically significant ice patches: insights into their age, internal structure, mass balance and climate sensitivity. *The Cryosphere*, 11:17–32.

Oppenländer, T. (2007). *Photochemical Purification of Water and Air*. Wiley-VCH Verlag GmbH & Co. KGaA.

Pavlova, P. A., Jenk, T. M., Schmid, P., Bogdal, C., Steinlin, C., and Schwikowski, M. (2015). Polychlorinated Biphenyls in a Temperate Alpine Glacier: 1. Effect of Percolating Meltwater on their Distribution in Glacier Ice. *Environmental Science and Technology*, 49(24):14085–14091.

Petrenko, V. V., Severinghaus, J. P., Smith, A. M., Riedel, K., Baggenstos, D., Harth, C., Orsi, A., Hua, Q., Franz, P., Takeshita, Y., Brailsford, G. W., Weiss, R. F., Buizert, C., Dickson, A., and Schaefer, H. (2013). High-precision ^{14}C measurements demonstrate production of in situ cosmogenic $^{14}CH_4$ and rapid loss of in situ cosmogenic ^{14}CO in shallow Greenland firn. *Earth and Planetary Science Letters*, 365:190–197.

Petrenko, V. V., Smith, A. M., Brook, E. J., Lowe, D., Riedel, K., Brailsford, G., Hua, Q., Schaefer, H., Reeh, N., Weiss, R. F., Etheridge, D., and Severinghaus, J. P. (2009). $^{14}CH_4$ Measurements in Greenland Ice: Investigating Last Glacial Termination CH_4 Sources. *Science*, 324(5926):506–508.

Petrucci, R. H., Herring, F. G., Madura, J. D., and Bissonnette, C., editors (2016). *General Chemistry: Principles and Modern Applications*. Pearson, 11th edition.

Preunkert, M., Legrand, M., Stricker, P., Bulat, S., Alekhina, I., Petit, J. R., Hoffmann, H., May, B., and Jourdain, B. (2011). Quantification of Dissolved Organic Carbon at Very Low Levels in Natural Ice Samples by a UV-Induced Oxidation Method. *Environmental Science and Technology*, 45(2):673–678.

Qsil GmbH (2012). *Lamp Materials*. Gewerbering 8, D-98704 Langwiesen, Germany.

Raymond, P. A. and Bauer, J. E. (2001). Riverine export of aged terrestrial organic matter to the North Atlantic Ocean. *Nature*, 409:497–500.

Reimer, P. J., Bard, E., Bayliss, A., Beck, J. W., Blackwell, P. G., Ramsey, C. B., Buck, C. E., Cheng, H., Edwards, R. L., Friedrich, M., Grootes, P. M., Guilderson, T. P., Haflidason, H., Hajdas, I., Hatté, C., Heaton, T. J., Hoffmann, D. L., Hogg, A. G., Hughen, K. A., Kaiser, K. F., Kromer, B., Manning, S. W., Niu, M., Reimer, R. W., Richards, D. A., Scott, E. M., Southon, J. R., Staff, R. A., Turney, C. S. M., and van der Plicht, J. (2013). IntCal13 and Marine13 Radiocarbon Age Calibration Curves 0 - 50,000 Years cal BP. *Radiocarbon*, 55(4):1869–1887.

Ruff, M., Wacker, L., Gäggeler, H. W., Ter, M., Synal, H.-A., and Szidat, S. (2007). A Gas Ion Source for Radiocarbon Measurements at 200 kV. *Radiocarbon*, 49(2):307–314.

Schalk, S., Adam, V., Arnold, E., Brieden, K., Voronov, A., and Witzke, H.-D. (2006). UV-Lamps for Disinfection and Advanced Oxidation - Lamp Types, Technologies and Applications. *IUVA News*, 8(1):33–37.

Schwikowski, M. and Eichler, A. (2010). Alpine Waters. In Bundi, U., editor, *The Handbook of Environmental Chemistry*, volume 6, pages 141–150. Springer-Verlag GmbH, Berlin.

Schwikowski, M., Jenk, T. M., Stampfli, D., and Stampfli, F. (2014). A new thermal drilling system for high-altitude or temperate glaciers. *Annals of Glaciology*, 55(68):131–136.

Schwikowski, M., Seibert, P., Baltensperger, U., and Gäggeler, H. G. (1995). A study of an outstanding Saharan dust event at the high-alpine site Jungfraujoch, Switzerland. *Atmospheric Environment*, 29(15):1829–1842.

Sharp, J. H. (2002). Analytical Methods for Total DOM Pools. In Hansell, D. A. and Carlson, C. A., editors, *Biogeochemistry of Marine Dissolved Organic Matter*, pages 35–58. Academic Press, 1 edition.

Sigl, M., Jenk, T. M., Kellerhals, T., Szidat, S., Gäggeler, H. W., Wacker, L., Synal, H.-A., Boutron, C., Barbante, C., Gabrieli, J., and Schwikowski, M. (2009). Towards radiocarbon dating of ice cores. *Journal of Glaciology*, 55(194):985–996.

Singer, G. A., Fasching, C., Wilhelm, L., Niggemann, J., Steier, P., Dittmar, T., and Battin, T. J. (2012). Biogeochemically diverse organic matter in Alpine glaciers and its downstream fate. *Nature Geoscience*, 5:710–714.

St-Jean, G. (2003). Automated quantitative and isotopic (^{13}C) analysis of dissolved inorganic carbon and dissolved organic carbon in continuous-flow using a total organic carbon analyser. *Rapid Communications in Mass Spectrometry*, 17(5):419–428.

Steier, P., Fasching, C., Mair, K., Liebl, J., Battin, T., Priller, A., and Golser, R. (2013). A New UV Oxidation Setup for Small Radiocarbon Samples in Solution. *Radiocarbon*, 55(34):373–382.

Steier, P., Shah, S. R., Drosg, R., Pearson, A., Fedi, M., Kutschera, W., Schock, M., Wagenbach, D., and Wild, E. M. (2008). Radiocarbon Determination of Particulate Organic Carbon in Non-Temperate, Alpine Glacier Ice. *Radiocarbon*, 48(1):69–82.

Stenström, K., Skog, G., Georgiadou, E., Genberg, J., and Johansson, A. (2011). A guide to radiocarbon units and calculations. Internal report, Lund University.

Stubbins, A., Hood, E., Raymond, P. A., Aiken, G. R., Sleighter, R. L., Hernes, P. J., Butman, D., Hatcher, P. G., Striegl, R. G., Schuster, P., Abdulla, H. A. N., Vermilyea, A. W., Scott, D. T., and Spencer, R. G. M. (2012). Anthropogenic aerosols as a source of ancient dissolved organic matter in glaciers. *Nature Geoscience*, 5:198–201.

Sugimura, Y. and Suzuki, Y. (1988). A high-temperature catalytic oxidation method for the determination of non-volatile dissolved organic carbon in seawater by direct injection of a liquid sample. *Marine Chemistry*, 24(2):105–131.

Synal, H.-A., Schulze-König, T., Seiler, M., Suter, M., and Wacker, L. (2013). Mass spectrometric detection of radiocarbon for dating applications. *Nuclear Instruments and Methods in Physics Research Section B*, 294:349–352.

Synal, H.-A., Stocker, M., and Suter, M. (2007). MICADAS: A new compact radiocarbon AMS system. *Nuclear Instruments and Methods in Physics Research Section B*, 259(1):7–13.

Szidat, S., Jenk, T. M., Gäggeler, H. W., Synal, H.-A., Hajdas, I., Bonani, G., and Saurer, M. (2004). THEODORE, a two-step heating system for the EC/OC determination of radiocarbon (^{14}C) in the environment. *Nuclear Instruments and Methods in Physics Research B*, 223-224:829–836.

Szidat, S., Salazar, G. A., Vogel, E., Battaglia, M., Wacker, L., Synal, H.-A., and Türler, A. (2014). ^{14}C Analysis and Sample Preparation at the new Bern Laboratory for the Analysis of Radiocarbon with AMS (LARA). *Radiocarbon*, 56(2):561–566.

Takeuchi, N., Uetake, J., Fujita, K., Aizen, V. B., and Nikitin, S. D. (2006). A snow algal community on Akkem glacier in the Russian Altai mountains. *Annals of Glaciology*, 43(1):378–384.

Thompson, L. G., Davis, M. E., Mosley-Thompson, E., Sowers, T. A., Henderson, K. A., Zagorodnov, V. S., Lin, P.-N., Mikhalenko, V. N., Campen, R. K., Bolzan, J. F., Cole-Dai, J., and Francou, B. (1998). A 25,000-Year Tropical Climate History from Bolivian Ice Cores. *Science*, 282(5395):1858–1864.

Thompson, L. G., Mosley-Thompson, E., Davis, M. E., Mashiotta, T. A., Henderson, K. A., Lin, P.-N., and Tandong, Y. (2006). Ice core evidence for asynchronous glaciation on the Tibetan Plateau. *Quaternary International*, 154155:3–10.

Uglietti, C., Zapf, A., Jenk, T. M., Szidat, S., Salazar, G., and Schwikowski, M. (2016). Radiocarbon dating of glacier ice. *The Cryosphere*, 10:3091–3105.

Van De Wal, R. S. W., Van Roijen, J. J., Raynaud, D., Van Der Borg, K., De Jong, A. F. M., Oerlemans, J., Lipenkov, V., and Huybrechts, P. (1994). From 14C/12C measurements towards radiocarbon dating of ice. *Tellus B*, 46(2).

van Roijen, J., van der Borg, K., de Jong, A., and Oerlemans, J. (1995). A Correction for In-Situ ^{14}C in Antarctic Ice with ^{14}CO. *Radiocarbon*, 37(2):165–169.

Wacker, L., Christl, M., and Synal, H.-A. (2010). Bats: A new tool for AMS data reduction. *Nuclear Instruments and Methods in Physics Research B*, 268:976–979.

Weast, R. C. and Astle, M. J., editors (1981–1982). *CRC Handbook of Chemistry and Physics*. CRC Press, Inc., Boca Raton, Florida, 62 edition.

Williams, P. M. and Druffel, E. R. M. (1987). Radiocarbon in dissolved organic matter in the central North Pacific Ocean. *Nature*, 330:246–248.

Williams, P. M., Oeschger, H., and Kinney, P. (1969). Natural Radiocarbon Activity of the Dissolved Organic Carbon in the North-east Pacific Ocean. *Nature*, 224:256–258.

Yoshimura, Y., Kohshima, S., Takeuchi, N., Seko, K., and Fujita, K. (2000). Himalayan ice-core dating with snow algae. *Journal of Glaciology*, 46(153):335–340.

Zapf, A., Nesje, A., Szidat, S., Wacker, L., and Schwikowski, M. (2013). ^{14}C Measurements of Ice Samples from the Juvfonne Ice Tunnel, Jotunheimen, Southern Norway Validation of a ^{14}C Dating Technique for Glacier Ice. *Radiocarbon*, 55(23):571–578.

Zhang, Y. L., Perron, N., Ciobanu, V. G., Zotter, P., Minguillón, M. C., Wacker, L., Prévôt, A. S. H., Baltensperger, U., and Szidat, S. (2012). On the isolation of OC and EC and the optimal strategy of radiocarbon-based source apportionment of carbonaceous aerosols. *Atmospheric Chemistry and Physics*, 12(22):10841–10856.

List of Symbols and Abbreviations

Abbreviation	Description
ACE	acetic acid
AMS	accelerator mass spectroscopy
BC	black carbon
BP	before present
C	carbon
^{14}C	radiocarbon
CO_2	carbon dioxide
DOC	dissolved organic carbon
EC	elemental carbon
$F^{14}C$	fraction modern
FOR	formic acid
GIS	gas inlet system
Hg	mercury
H_2O	water
H_3PO_4	phosphoric acid
IC	inorganic carbon
IR	infrared
LARA	Laboratory for the Analysis of Radiocarbon with AMS
lN_2	liquid nitrogen
MFC	mass flow controller
MICADAS	MIni radioCArbon DAting System
NDIR	non-dispersive infrared
OC	organic carbon
OD	outer diameter
OXA	oxalic acid
PETG	polyethylene terephthalate glycol-modified

Abbreviation	Description
PFA	perfluoroalkoxy
PHP	potassium hydrogen phthalate
PID	proportional-integral-derivative
POC	particulate organic carbon
PSI	Paul Scherrer Institute
PTFE	polytetrafluoroethylene
SJ	spherical joint
TC	total carbon
TOC	total organic carbon
UHP	ultra-high purity
UPI	ultra-pure ice
UPW	ultra-pure water
UV	ultraviolet
WIOC	water-insoluble organic carbon
WSOC	water-soluble organic carbon

Acknowledgements

The success of this work is based on the help, input and effort of many colleagues and friends. I want to express my sincere gratitude to all of you for realising this exciting endeavour!

First, I deeply thank Margit Schwikowski for all her support, expertise, trust and confidence. Her door was always open and she opened many doors for me – thanks. It was great to work with her and as part of her team, both at PSI and on field trips.

I thank the whole Analytical Chemistry team for the good working atmosphere. In particular Theo Jenk was of big help at times when I lost confidence in the lab. Anja Eichler's positive attitude and input on chemistry were very supportive. I thank Chiara Uglietti for performing AMS measurements and sampling Juvfonne ice patch. Also Sabina Brütsch helped with chemistry lab services and Michael Sigl added a lot of fun to working at PSI. My first contact to the team was Alexander Zapf who sadly passed away in the midst of his life. I will keep him in my best memory.

Situated in Bern and operating the MICADAS, the LARA was my second workplace. I owe my best thanks to Sönke Szidat for his support with expertise, infrastructure and many stimulating discussions. Furthermore, I thank the whole team and in particular Gary Salazar for running MICADAS.

The former Laboratory for Radio- and Environmental Chemistry offered a profound base for this project. Both Dave Piguet and Mario Birrer, the genial workshop wizards were great consultants for the actual setup. Robert Eichler helped with critical views and hardware components. The secretaries Angela Blattmann and Doris Bühler always were straightforward and supportive.

Being part of the Oeschger Centre for Climate Change Research and its PhD programme, network and events was a big plus for me.

Steven Beaupré, formerly at University of California, generously shared his experience and know-how with me. Together with Andreas Stubbe and co-workers from Glas Keller AG, the glass setup was created after many revisions as a piece of glass-blowing art. I enjoyed to meet Dieter and Felix Stampfli on several field trips and to use their great ice drilling technology.

Finally, I want to thank my family. My parents Lisa and Wolfgang always gave me great freedom, trust and love and offered me best conditions. My wonderful wife Christiane was the best company along this way and also gave a lot of her time for me to finalise this work – thank you.

Declaration

Under Art. 28 Para. 2 RSL 05

Last, first name:	Schindler, Johannes
Matriculation number:	11-130-416
Programme:	Climate Sciences
	Bachelor ☐ Master ☐ Dissertation ☒
Thesis title:	An Extraction System for Radiocarbon Microanalysis of Dissolved Organic Carbon in Glacier Ice
Thesis supervisor:	Prof. Dr. Margit Schwikowski

I hereby declare that this submission is my own work and that, to the best of my knowledge and belief, it contains no material previously published or written by another person, except where due acknowledgement has been made in the text. In accordance with academic rules and ethical conduct, I have fully cited and referenced all material and results that are not original to this work. I am well aware of the fact that, on the basis of Article 36 Paragraph 1 Letter o of the University Law of 5 September 1996, the Senate is entitled to deny the title awarded on the basis of this work if proven otherwise.

Bern,

Signature